Development and Application of Augmented Smartphone-enabled Imaging in Mobile Health

Qinghua He

A dissertation

Submitted in partial fulfillment of the

Requirements for the degree of

Doctor of Philosophy

University of Washington

2022

Reading Committee

Ruikang K. Wang

Ivan M. Pelivanov

Jonathan T. C. Liu

Program Authorized to Offer Degree

Bioengineering

University of Washington

Abstract

Development and Application of Augmented Smartphone-enabled Imaging in Mobile Health

Qinghua He

Chair of the Supervisory Committee:

Professor Ruikang K. Wang

Bioengineering

Mobile health techniques aim to deliver healthcare remotely and wirelessly using surging computing power and mobile connectivity. The commercial smartphone is naturally becoming a popular partner device due to its computing/communication capacity and built-in sensors, such as the camera, microphone and touch screen modules. Among these sensing units, the camera is experiencing extensive technical iterations and nowadays capable of delivering medical-grade imaging, which fashioned a foundation for an important branch of mobile health techniques: the smartphone-enabled imaging from afar. The main goal of this thesis is to develop augmented smartphone-enabled imaging techniques and apply them in health evaluation. To achieve the augmentation, intrinsic medical information will be mined from the regular vision data stream, including smartphone photographs and videos. Firstly, smartphone-enabled multispectral imaging will be developed based on the snapshot RGB-mode photography. Corresponding system

and method will be applied and tested in detecting chromophores in human tissue. Then, this technique will be expanded to realize smartphone-enabled multispectral fluorescence imaging to detect porphyrins to estimate the bacterial contamination within skin tissue and oral cavity. Further, smartphone-enabled multispectral remote photoplethysmography will be developed to spatially monitor the skin oxygenations and hemodynamics. Lastly, a multifunctional platform will be developed to integrate these augmented smartphone imaging functions into a mobile app and clinically validated in predicting the blood bilirubin level of patients with liver diseases.

CONTENTS

LIST OF FIGURES

LIST OF TABLES

ACKNOWLEDGEMENTS

First and foremost, I am extremely grateful to my supervisors, Prof. Ruikang Wang for his invaluable advice, continuous support, and patience during my PhD study. His immense knowledge and plentiful experience have encouraged me in all the time of my academic research and daily life. Thank you for trusting my potentials and being supportive on my research exploration. Thank you for supervising me on how to initiate, organize, justify and present the research. Your dedication and wisdom have inspired me to keep going ahead in this way.

I would also like to thank my committee members, Prof. Jonathan Liu, Prof. Ivan Pelivanov and Prof. Dan Fu for spending their valuable time on reviewing my work and giving me suggestions. Without their kind help and support, it would be impossible for me to complete my study.

I would like to thank my colleagues in the Biophotonics and Imaging Laboratory (BAIL). Special thanks to Dr. Yuandong(Jenny) Li, Dr. Peijun Tang, Dr. Yiming Lu, Dr. Qinqin Zhang, Yuxuan Cheng, Dr. Hao (Diana) Zhou and Dr. Nhan Le who gave me a lot of technical supports. Great thanks to Teng Liu, Yaping Shi, Xiao (Gabriella) Zhou and Yi Zhang for helping me with my research work. Thanks to all members in BAIL for providing me with friendship and encouragement.

Special thanks to our external collaborators, Prof. Zhiyuan Sun and his team from CIOMP, Dr. Philip Rosenfeld, Dr. Giovanni Gregori and Dr. Mengxi Shen from BPEI, Prof. Nina Lu from UW Medicine. I was also lucky to learn from Prof. Steven Jacques and Prof. Kirk Beach from UW.

I am eternally grateful for my parents, Ms. Anrong Pan and Mr. Shaoping He, for their unconditional love and support. They teach me how to face the difficulties in life and encourage me to pursue my career and dream.

Lastly, from the bottom of my heart I would like to say big thank you to my girlfriend and best friend ever, Miss. Xiaoling Zhuang. Without her, I cannot imagine how to survive the darkest hours in the past tough years.

Chapter 1. INTRODUCTION

1.1 SIGNIFICANCE AND RESEARCH MOTIVATION

Mobile health (mHealth) is an emerging term in medical practice and public healthcare that uses mobile communication devices for medical data acquirements, diagnostic support, information communication, and remote monitoring[1]. The first goal of the mHealth-motivated technique revolution is to promote current heavy-laden and unbalanced healthcare system[2]. The population in many countries, especially low-income countries, always face varying shortages of medical resources. For example, the WHO notes a global deficit of 2.4 million healthcare workforce[3]. Even worse, the existed medical resources are far from evenly distributed. For example, the density of doctors, nurses and midwives in the US is four times higher than the number in Africa[4]. Even in the region with less resource constraints, the prospects can hardly be optimistic due to other factors like population aging. By 2050, one in four people, which is 1.3 billion in total, in Asia and the pacific will be over 60 years' old[5]. The massive population aging will lead to a rapid growth of medical service demand and reduced healthcare workforce. To address, or at least alleviate, these problems, the mHealth concept has been proposed and developed to improve various perspectives of medical service, including the affordability, accessibility and shareability.

Smart devices like Apple Watch and Fitbit firstly arouses the interests of public to mHealth devices. However, the developing of mHealth devices has experienced a long journey and now is in a grooming age due to the progressively miniaturized and powerful mobile computing and communication capacities (Figure 1.1). In general, current mHealth

techniques can be divided into three main categories: wearable sensors, lab on chip and imaging from afar[6]. Wearable sensors work in varying forms, such as watches[7], bracelets[8], earphones[9] and rings[10]. The unobtrusive existence of sensors in these devices eases the passive and continuous measurements of biometric signals, which is appropriate to be used in vital signs monitoring and chronic disease managements. Lab-on-chip techniques were derived from the combination of microfluidics and microelectronics, which mainly focus on developing sensors to detect molecules in body liquid samples, such as sweat, blood, saliva, urine and tears[11]. The ubiquitous point of care tests realized by these techniques are possible to predict or screen potential diseases by sensing the biomarkers. While above two categories focus on global signals and features, imaging from afar provides new possibilities for diagnosing specific lesions within organs and tissues[12]. For example, digital dermoscope[13], otoscope[14], ophthalmoscope[15] and endoscope[16] can deliver diagnosis to skin, ear, fundus and digestive system. According to the study on the global mobile phone penetration rate, there are over 7 billion mobile phone subscribers all over the world. The increased availability and performance of smartphone is accelerating the implementation of imaging techniques in mHealth.

This thesis will proceed from the regular smartphone-enabled imaging to explore its augmented functions. Several techniques, including smartphone-enabled multispectral imaging, fluorescence imaging and remote photoplethysmography, will be specifically developed. Multiple subjects like blood perfusion, blood pulsation, pigmentation and bacterial contamination will be investigated using these techniques. In the following sections, I will briefly introduce these imaging techniques and their applications in healthcare.

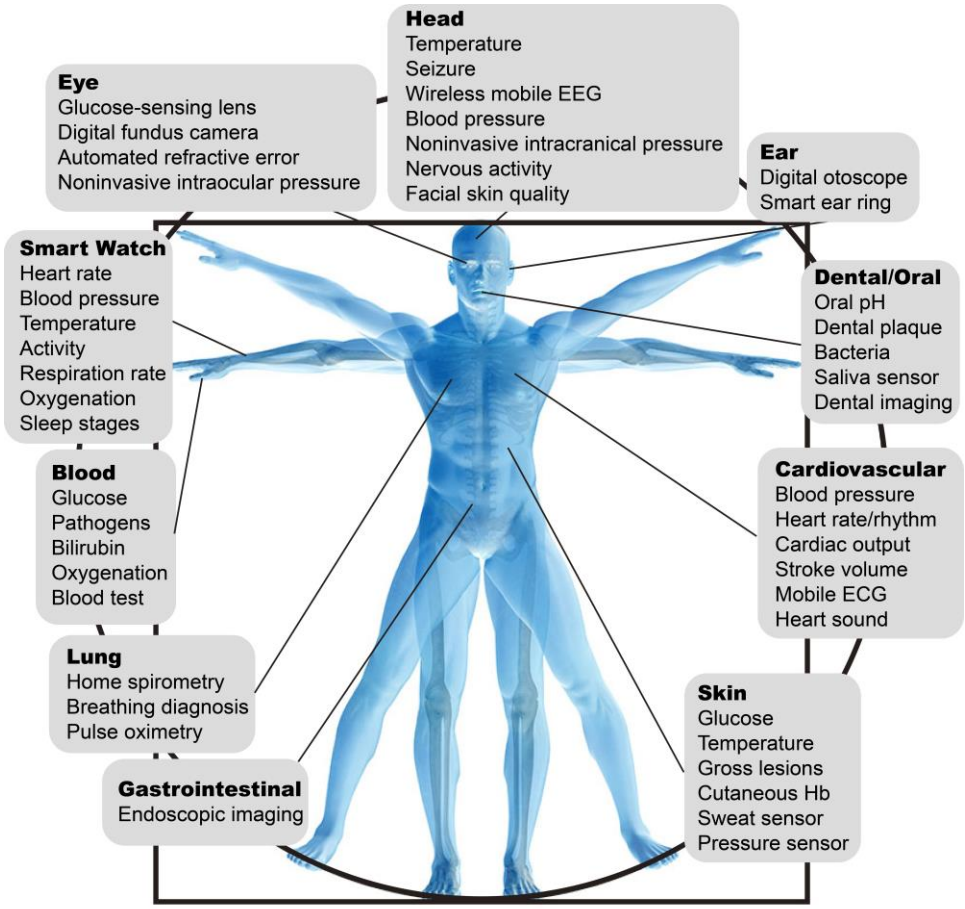

Figure 1. 1. Applications in mHealth

1.2 TECHNICAL BACKGROUND

1.2.1 SMARTPHONE-ENABLED IMAGING IN MHEALTH

Smartphones are the most commonly used tools in the mHealth-motivated imaging from afar techniques due to the low cost and high penetration rate in population[17](Figure 1.2). Smartphone-enabled imaging is capable of acquiring users' medical images not only in laboratories and clinics, but also in their daily lives to facilitate diagnosis and aid clinical management. The most straightforward and prolific usage of smartphone-enabled imaging is in digital dermoscope. For example, in a study to assess the benign and malignant pigmented and unpigmented skin lesions, the smartphone dermoscope delivered diagnosis

with a strong correlation with conventional clinical examination[18]. Moreover, in another study of wound management, researchers demonstrated the smartphone-enabled wound imaging can largely shorten the response time when there is a wound deterioration[19]. Fundus photography usually requires specialized cameras. However, being used with an ophthalmic lens, the smartphone can be easily transformed into a smartphone fundus camera, which can improve the accessibility of fundus examination in low-resource settings[20]. Except for above usages, other typical applications of smartphone-enabled imaging include cardiology, dental/oral healthcare and endoscopy. In these applications, the smartphone benefits the public healthcare mostly in the connectivity and usability. More discrete subjects, such as the patients in rural areas, can be linked to the central repositories like clinics or available clinicians. Some current existed connections can be strengthened. For example, the inspection frequency can be increased by replacing onsite follow-up visiting with continuous and real-time imaging. The low cost, high subscriber quantity and packaged apps significantly lower the threshold for smartphone users to access their own medical services.

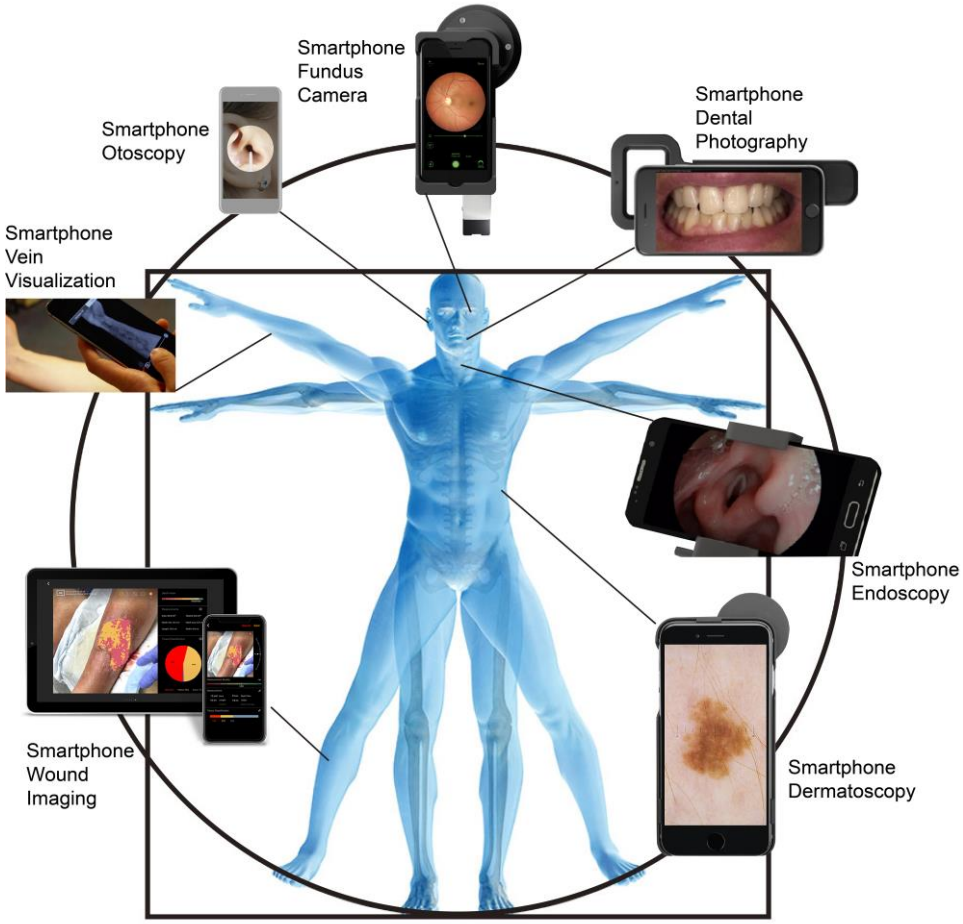

Figure 1. 2. Applications of smartphone-enabled imaging in mHealth

1.2.2 IMAGING AUGMENTATION

Although showing significant benefits and potential, current smartphone-enabled imaging mainly works in a somewhat simple mode to deliver ‘vision field’ and ‘vision-based diagnosis’. Most data streams were acquired and transmitted in RGB-mode to maximally simulate human naked-eye vision. In this case, the features that can be provided for diagnosis would be mainly limited to colors, shapes and textures. To augment the smartphone-enabled imaging and promote the diagnosis, one solution is to adopt diverse imaging modalities to expose the information of subjects in more dimensions. In this thesis, three different imaging modalities, including multispectral imaging, fluorescence imaging

and remote photoplethysmography, will be adopted in smartphone-enabled imaging and discussed.

1.2.2.1 MULTISPECTRAL IMAGING

Multispectral imaging technique is developed to capture image data of subjects at specific wavelengths across the electromagnetic spectrum[21]. The target can be differentiated from the multispectral data cube when it performs unique spectral properties, like absorbance, reflectance and scattering. Multispectral imaging has been used in a broad range of applications since chromophores widely exist in the universe and environment we lived. For example, in aerospace photogrammetry, the light collected by the detector will be separated into different wavebands to identify the feature type of the cosmic emission[22]. In remote sensing imaging, the multispectral channels are capable of recognizing plants, mines and buildings without silhouette details[23].

Due to the spectral characteristics of various chromophores within human tissue, such as hemoglobin, melanin and bilirubin, the imaging at different wavelengths can be combined to contrast them from the surrounding tissue[24]. Conventional systems in these applications rely on the wavelength-selection units to physically separate the collected light, which can be roughly classified into time and space-varied methods. In time-varied methods, the wavelength selection is realized by sequentially switching spectral filters or light sources. For example, Diebele et al used solid-state liquid crystal to realize spectral imaging in the clinical evaluation of melanomas and common nevi[25]. Spigulis et al applied color LED to provide illuminations for smartphone-based skin assessment[26]. In space-varied method, the multiple optical paths working at different wavelengths are coexisted so the multispectral data cube can be captured with a snapshot. Diverse spatial

configurations and structures can be designed under this concept, such as multi-aperture filtered camera[27], coded aperture snapshot imager[28] and image mapping spectrometry[29]. For example, multi-aperture filtered camera utilizes the combination of lens array and filter array to realize multispectral imaging on a single sensor. The IMEC in Belgium optimized this strategy and developed snapshot multispectral imager based on the on-chip Fabry-Perot filter array. This system shares similar optic path with regular imaging system but the pixel matrix on the CMOS sensor was covered by a multispectral filter array so the snapshot image includes multispectral data cube arranged in a specific matrix structure.

1.2.2.2 FLUORESCENCE IMAGING

Fluorescence imaging is a molecular imaging technique which detects the emission from molecules after absorbing electromagnetic radiation[30]. From the image data, the spatial distribution, abundance, and activity of the target molecules, also termed fluorophores, can be investigated. Fluorescence imaging has a wide application in molecular biology. Fluorescent dye is usually used as the label of DNA and protein probes in PCR, Blotting and DNA sequencing[31]. The most common in vivo applications of fluorescence imaging including calcium imaging. and fluorescein angiography. The calcium ion in the neural activity can bound to injected calcium indicators and change their fluorescence signals, so this mechanism can be used to estimate the condition of nervous system[32]. Fluorescein angiography is a technique used in the evaluation of retinal disease by injecting fluorescein dye and capturing its emission with fundus camera[33].

Except above ex vivo or agent-based methods, in vivo autofluorescence imaging is another technique which has not been fully explored but shows great potentials as well[34].

Human tissue contains bunch of fluorophores, such as NADPH, flavin, collagen, elastin and porphyrin, which can be imaged without agent injections[35]. From the autofluorescence signal of these components, different conditions can be estimated, such as bacterial contamination, tissue generation and aging. For example, some research has introduced autofluorescence imaging to detect advanced glycation end product to evaluate aging and degenerative diseases[36]. Further, some devices have been already designed and commercialized to estimate the autofluorescence within human tissue. One typical example is Moleculight i:X, which was developed and fabricated to monitor the bacterial contamination by imaging porphyrin fluorescence in wound managements[37].

1.2.2.3 REMOTE PHOTOPLETHYSMOGRAPHY

Photoplethysmography (PPG) is becoming one of the most popular techniques to access the hemodynamic information inside the human body[38]. Nowadays, it has been widely used for in-hospital monitoring and even in wearable devices nowadays. Due to the strong absorption of blood to the light, PPG works by recording time-elapsed optical reflectance modulated by the effective blood volume within light interrogated tissue volume to indicate the dynamic pulsatile behavior of the blood flow (volume) caused by cardiac heartbeat[39]. Remote photoplethysmography (rPPG) works in a similar mechanism with PPG but it is typically implemented by a camera-based system[40]. The video of tissue would be acquired to record the temporal variation of tissue reflection. Using dedicated signal processing algorithms, subtle momentary changes in the tissue reflection in the video can be extracted. With this dynamic and pulsatile blood flow behavior directly obtained from the human tissue, rPPG can be used to monitor the heart rate[41], respiration[42] and blood oxygenation[43]. Except for these global vital signs, some newly developed methods has been using the spatial resolution of rPPG to investigate localized features like blood

pulsations[44] and pulse wave transitions [45], which can be used as biomarkers for localized organ lesions and vascular abnormalities.

1.3 SCOPE OF THE THESIS

The objective of this thesis is to propose augmented smartphone-enabled imaging techniques and explore their applications in mobile health. To achieve so, firstly, a novel smartphone-enabled multispectral imaging method will be developed in Chapter 2 to provide a strategy for identifying chromophores in human tissue. In Chapter 3, a new smartphone-enabled multispectral fluorescence imaging system will be developed to estimate bacterial contamination following the strategy used in Chapter 2. Chapter 4 will combine the smartphone-enabled multispectral imaging technique and rPPG together to realize spatiotemporal monitoring of skin blood pulsation and oxygenation variation. Chapter 5 will adopt this strategy to develop a mobile app as the multifunctional augmented smartphone imaging platform and use it to predict patients' bilirubin levels in clinics. The last chapter of this thesis will summarize and conclude the research, and discuss the future plan of this topic.

Chapter 2. DEVELOPMENT OF SMARTPHONE-ENABLED MULTISPECTRAL IMAGING METHOD FOR ANALYZING TISSUE CHROMOPHORES

2.1 BACKGROUND AND MOTIVATION

The application of multispectral imaging in cosmetology and dermatology is becoming increasingly popular and appealing to academic researchers and industrial entrepreneurs[46]. Based on specific spectral characteristics of chromophores with skin tissue, for example hemoglobin and melanin, multispectral imaging can be used to separate and contrast the target chromophores from others, upon which to analyze and monitor skin features[47].

A number of multispectral imaging systems have been recently developed for the analysis of skin features. One of such uses monochromatic lasers or optical filters (either filter wheels or tunable filters) to provide specific spectral illumination and uses a single array detector to sequentially capture the tissue reflection images[48]. For example, Mo et al used LED to provide illumination in multispectral imaging[49]. Diebele et al tuned illumination wavelengths with liquid crystal filters for the clinical evaluation of melanomas and common nevi [25]. In these devices, wavelength-selection procedure requires at least tens of milliseconds to complete, leading to asynchronous data acquisitions for different wavelengths. Consequently, both tissue motion and device movements would inevitably cause motion artifacts, affecting our ability to interpret the final results. In addition, the need to select the wavelengths complicates the system setup, not a cost-effective solution for daily-use purposes.

Recent development of multispectral cameras surges new interests and new opportunities for multispectral imaging[29]. This type of camera is manufactured by

assembling optical-filter array on the sensor, so that the pixels on the sensor can be separated into various wavebands, enabling spectral images across a wide spectrum to be captured at once[50]. Such capability of snapshot-capturing multispectral images eliminates motion artifacts during data acquisition and improves device compactness[51]. However, due to complicated design and enabling fabrication, the cost is currently at least prohibitive for routine and cost-effective applications. And also, the number of pixels available in the spectral array is limited, which directly translates to the limited imaging resolution that can be achieved. As a result, a high demand remains for a multispectral system that is capable of high-resolution imaging, and at the same time, is immune to motion artifacts, compact and cost effective so that it can be deployed to a wider user community for daily assessment of the skin features.

In the past decade, the developments in smartphone have changed the daily life of human beings. Both the technical development and the consumer group have experienced explosive improvements. Nowadays, a typical camera in a smartphone has 8 to 12 million pixels and is capable of high-speed imaging, ideal as a low-cost and handy imaging device for skin assessments[52]. There have seen some developments of smartphone-based skin analysis[53], however, these developments simply take a straightforward approach to enhance the images captured by the camera.

In this paper, we propose a novel concept and method that utilizes an unmodified smartphone to enable multispectral imaging, where RGB images captured by the built-in camera is used to reconstruct “pseudo”-multispectral images through a transformation using Wiener estimation. The reconstruction process is calibrated with a snapshot multispectral camera with 16 spectral channels. After the reconstruction of multispectral

images from RGB images, we use a weighted subtraction strategy to demonstrate the extraction of the chromophore information, e.g. blood, melanin absorption, oxygenation etc. within the skin from the RGB images captured by the smartphone, which are then compared with the results directly obtained from snapshot multispectral camera. Finally, we show the usefulness of the proposed approach in the analysis of skin morphological features. Meanwhile, in the application of monitoring the hemodynamic activities, we successfully detect the heartbeat and map the vascular occlusion effect on the skin.

2.2 MATERIAL AND METHODS

2.2.1 RECONSTRUCTION PRINCIPLE FROM RGB IMAGES TO MULTISPECTRAL IMAGES

The accuracy of extracting information from the measurements related to a specific chromophore (e.g. hemoglobin) relies on how the measurements represent accurately its characteristic absorption features across the wavelengths. However, the sensor in the smartphone has only three sensitive channels (red, green and blue), and each channel detects the lights that are integrated over its spectral sensitive bandwidth (that typically ranges as wide as >50 nm, though its peak wavelength is at R, G or B). Such integration reduces the sensitivity of the measurement to chromophore features that makes the accurate extraction of the chromophore information difficult. Multispectral reconstruction to refine the measurement signal before processing could be a useful solution to mitigate this problem. To recover high-dimensional information from low-dimensional data, several reconstruction techniques have been investigated, such as finite-dimensional modeling[54], pseudo-inverse[55] and Wiener estimation[56]. Among these, Wiener estimation proves superior in terms of reconstruction accuracy and computational efficiency[57]. Therefore,

we elected the Wiener estimation algorithm to perform multispectral reconstruction from RGB images captured by a smartphone camera. In smartphone camera, the response of RGB channels can be depicted as:

$$V_C = \int l(\lambda)\gamma(\lambda) f_C(\lambda)s(\lambda)d\lambda = \int m_C(\lambda)\gamma(\lambda)d\lambda \quad (2.1)$$

where λ is the wavelength, V_c is the response of subchannel c in the smartphone camera (c=R,G,B), $l(\lambda)$ is the spectral power distribution of illumination, $f_c(\lambda)$ is the spectral transmittance of the filter in subchannel c, $s(\lambda)$ is the spectral sensitivity of camera sensor. $m_c(\lambda)$ is the product of $l(\lambda)$, $f_c(\lambda)$ and $s(\lambda)$, which is the spectral responsivity of each subchannel. $\gamma(\lambda)$ is the spectral reflection of the sample. The matrix form of equation (1) can be represented as:

$$\mathbf{V} = \mathbf{M}\boldsymbol{\gamma} \quad (2.2)$$

where **V** is the vector of smartphone camera response, **M** is the matrix of spectral responsivity in smartphone camera, $\boldsymbol{\gamma}$ is the vector of sample reflection.

In the Wiener estimation, the core step is to find a reconstruction matrix, which is used to transform RGB images to multispectral images. This step necessitates training multiple samples with known colors for calculation and error correction. In our study, we used 100 color blocks with different reflectance in visible wavelength bands as the training set samples. Traditionally, the spectral reflection from the color blocks can be calibrated with a well-characterized spectrometer. In doing so, the sampling areas in the smartphone camera imaging and spectral reflection measurements need to match with each other, which is termed the co-registration step. This would increase the workload and introduce

additional instabilities in the calibration. Furthermore, the reflection measurement and co-registration steps are supposed to be repeatedly conducted for 100 samples, which may cause even heavier workloads and more instabilities.

To mitigate the tedious procedures when using spectrometer for calibration, we instead used a snapshot multispectral camera (MQ022HG-IM-SM4X4-VIS, XIMEA, Germany) with 16 spectral channels to provide spectral reflection calibrations. With this multispectral camera, all training steps were replaced by taking one RGB image and one multispectral image of the color chart with100 color samples. The illumination light sources in the training should be the same to the light sources used in the later imaging process to the skin, which includes the smartphone flashlight and fluorescent lamp in our study. The measurements of these 100 samples and co-registration of each sampling area can be achieved by selecting and calculating the subchannel values of corresponding target area from color chart images. When the sample is captured by the snapshot multispectral camera, the response of each subchannels is depicted as:

$$V'_{C'} = \int l(\lambda)\gamma(\lambda)\, f_{C'}(\lambda)s'(\lambda)d\lambda = \int m'_{C'}(\lambda)\gamma(\lambda)d\lambda \tag{2.3}$$

where $V'_{c'}$ is the response of c'th subchannel (c=1,2,3, $\cdots$, 16), $f_{c'}(\lambda)$ is the spectral transmittance of the filter in c'th subchannel, $s'(\lambda)$ is the spectral sensitivity. $m'_{c'}(\lambda)$ is the product of $l(\lambda)$, $f_c(\lambda)$ and $s(\lambda)$, which is the spectral responsivity of each subchannel in the multispectral camera. The matrix form of equation (3) is then expressed as:

$$\boldsymbol{V' = M'\gamma} \tag{2.4}$$

where $\mathbf{V}'$ is the vector of multispectral camera response, $\mathbf{M}'$ is the matrix of spectral responsivity in multispectral camera. To reconstruct multispectral images from RGB images, we assume the reconstruction matrix is $\mathbf{W}$. The process is expressed as:

$$\widetilde{\boldsymbol{V}}' = \boldsymbol{WV} \tag{2.5}$$

where $\widetilde{\mathbf{V}}'$ is the reconstructed multispectral image. To ensure the accuracy of reconstruction, the minimum square error between the reconstructed multispectral image and the original multispectral image should be minimized. The minimum square error is calculated as:

$$\begin{aligned} e &= \left\langle (\boldsymbol{V}' - \widetilde{\boldsymbol{V}}')^{\boldsymbol{t}} (\boldsymbol{V}' - \widetilde{\boldsymbol{V}}') \right\rangle \\ &= \langle \boldsymbol{V}'^{\boldsymbol{t}} \boldsymbol{V}' \rangle - \boldsymbol{W} \langle \boldsymbol{V}'^{\boldsymbol{t}} \boldsymbol{V} \rangle - \boldsymbol{W}^{\boldsymbol{t}} \langle \boldsymbol{V}^{\boldsymbol{t}} \boldsymbol{V}' \rangle + \boldsymbol{W}^{\boldsymbol{t}} \boldsymbol{W} \langle \boldsymbol{V}'^{\boldsymbol{t}} \boldsymbol{V}' \rangle \end{aligned} \tag{2.6}$$

When the partial derivative of e with respect to $\mathbf{W}$ is zero, the minimum square error is minimized, expressed as:

$$\frac{\partial e}{\partial \boldsymbol{W}} = -\langle \boldsymbol{V}'^{\boldsymbol{t}} \boldsymbol{V} \rangle + \boldsymbol{W}^{\boldsymbol{t}} \langle \boldsymbol{V}^{\boldsymbol{t}} \boldsymbol{V} \rangle = 0 \tag{2.7}$$

The reconstruction matrix is derived as:

$$\boldsymbol{W} = \langle \boldsymbol{V}' \boldsymbol{V}^{\boldsymbol{t}} \rangle \langle \boldsymbol{V} \boldsymbol{V}^{\boldsymbol{t}} \rangle^{-1} \tag{2.8}$$

where $\langle \quad \rangle$ is an ensemble-averaging operator. $\langle \mathbf{V}' \mathbf{V}^t \rangle$ is the correlation matrix between the multispectral response and smartphone camera response. $\langle \mathbf{V} \mathbf{V}^t \rangle$ is the autocorrelation matrix of the smartphone camera response. The reconstruction matrix was

calculated from the calibration of a color chart which contains 100 color blocks. With this reconstruction matrix, skin images captured by a smartphone camera can be reconstructed into multispectral images.

2.2.2 WIENER ESTIMATION MATRIX CALCULATION

A schematic setup of the multispectral reconstruction calibration is shown in Figure 2.1(a). We used a color chart with 100 randomly selected known-color blocks. The color chart was illuminated by the flashlight from a smartphone (Mate SE, HUAWEI, China). Both the smartphone camera (Sensor model: Sony IMX371) and the snapshot multispectral camera were used to acquire images of the color chart. The smartphone camera has a sensor with 3264×2448 pixels and works in the RGB mode. The snapshot multispectral camera (MQ022HG-IM-SM4X4-VIS, XIMEA, Germany) houses a CMOS sensor with 2048×1088 pixels, where a filter array separates the sensor array into 512×272 super-pixels. Each super-pixel contains a 4×4 spectral sensitive pixel-matrix that are sensitive to 16 wavebands, termed as 16 subchannels. Figure 2.1(b) shows the spectral sensitivity curves of 16 subchannels in the snapshot multispectral camera. The specific values of spectral characterization of the snapshot multispectral camera is shown in Table 2. 1. The RGB mode image of the color chart from smartphone camera is shown in Figure 2.1(c). From the raw multispectral data, we extracted a representative image from the sub-channel of band 9 (615 nm) as an example, shown in Figure 2.1(d). The spectral power distribution of the smartphone flashlight is shown in Figure 2.1(e). Meanwhile, the multispectral data of light source was measured from the polymer white diffuser standard (SphereOptics GmbH, 95% Reflectance) under the smartphone flashlight illumination. Therefore, the reflectance of the color chart in 16 subchannels can be calculated. Based on equation (8), we calculated the correlation matrix between multispectral response and the smartphone camera response,

and the autocorrelation matrix of the smartphone camera to obtain the Wiener estimation matrix. To minimize the estimation error, we used the averaged values of pixel responses in the central area, which is one fourth of the total area, of every color block in the calibration.

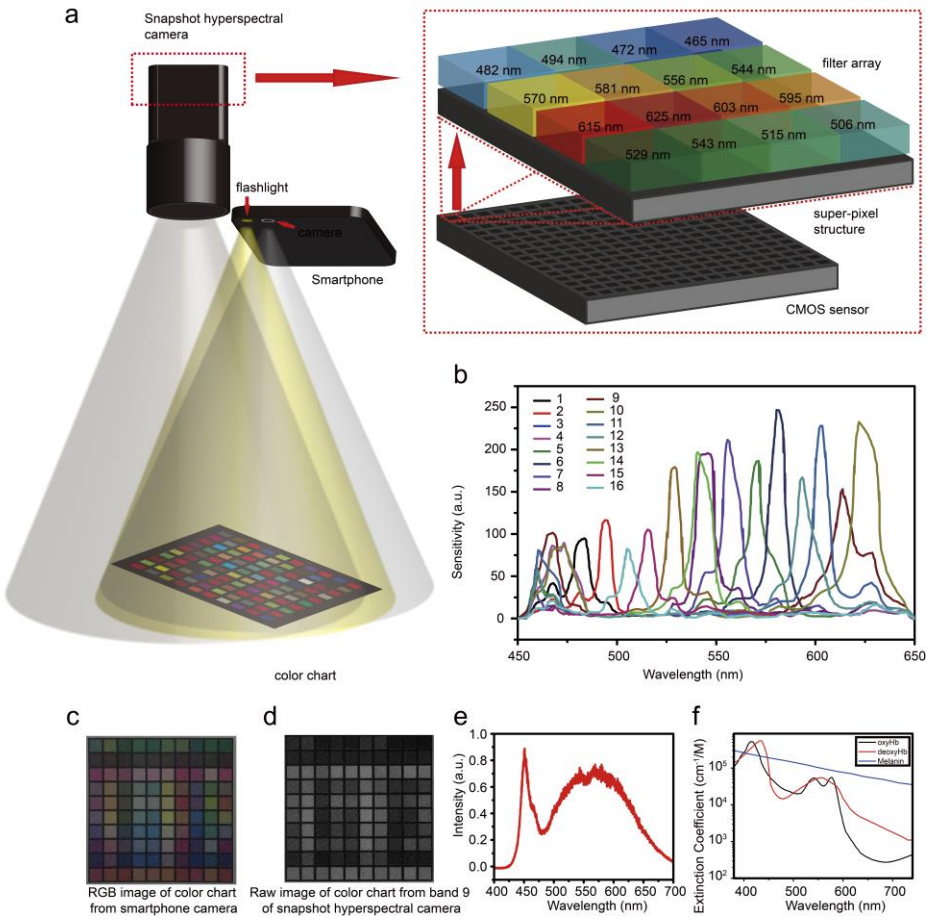

Figure 2. 1. Schematic of the smartphone-enabled multispectral reconstruction.
(a) The multispectral reconstruction calibration system that consists of a smartphone, color chart and 16-channel multispectral camera, with sensor structure and sensitive wavebands at each subchannel shown in the top left. (b) The manufacturer's data of wavelength-dependent sensitivity for 16 bands in the snapshot multispectral camera. (c) The RGB image of color chart from the smartphone camera. (d) The raw image of color chart directly exported from the band 9 in the snapshot multispectral camera. (e) Spectral power distribution of the smartphone flashlight that is used in this study. (f) Absorption spectra of oxyhemoglobin (oxyHb), deoxyhemoglobin (deoxyHb) and melanin.

Table 2. 1. The spectral characterization of snapshot multispectral camera.

Band number	1	2	3	4	5	6	7	8	9	10	11	12	13	14	15	16
Center wavelength (nm)	482	494	472	465	570	581	556	544	615	625	603	595	529	543	515	506
Spectral bandwidth (nm)	10	8	13	18	10	10	10	10	15	13	10	10	9	10	10	10

2.2.3 MULTISPECTRAL RECONSTRUCTION AND POST-PROCESSING

Chromophores, such as hemoglobin and melanin, are the key factors for the skin assessments. By extracting their absorption information from the skin, these chromophore features can be contrasted from surrounding tissues, realizing specific assessment. We recruited two volunteers and used the smartphone to capture RGB images from their faces, where there appears redness and moles (i.e., nevi) on the skin. This study adhered to the tenets of the Declaration of Helsinki and was performed in accordance with the Health Insurance Portability and Accountability Act. Ethical approval was obtained from the Institutional Review Board of the University of Washington. All enrolled participants provided written informed consent.

With our method, we extracted the hemoglobin-related redness and melanin-related moles from the facial skin and separated them from each other. The distribution of chromophores provides the basis for assessing morphological features. The time-resolved variation of hemoglobin absorption may be used as an index of hemodynamic monitoring, which may be useful to infer pathological information. With the calculated Wiener estimation matrix, we transformed RGB images of the skin acquired by the smartphone

camera into the multispectral images, simulating the images as if they were captured by the 16-spectral channel multispectral camera. From the reconstructed multispectral images, we extracted spatial absorption information of skin chromophores, e.g. melanin and hemoglobin, through a series of processing steps on images representing different wavebands. Figure 2.1(e) shows plots of absorption efficiencies of melanin and hemoglobin, respectively. For example, in this scheme in order to extract the absorption information caused by hemoglobin in blood, we selected several red light wavebands, including bands 8 (615 nm), 9 (625 nm), 10 (603 nm), 11 (595 nm), and subtracted one by one from green light wavebands, including bands 6 (556 nm), 7 (544 nm), 12 (529 nm), 13 (543 nm). From 'Green bands' to 'Red bands', the absorption of the chromophores of interest decreases, but the rate of decrease is slow for melanin, and rapid for hemoglobin. By subtracting the measurement at 'Red bands' from that at 'Green bands', the contribution of melanin absorption to the extraction of hemoglobin absorption can be suppressed. Thus, we used the weighted subtraction to emphasize the hemoglobin absorption measurement, indicating blood perfusions in skin samples. The weighted subtraction is expressed as:

$$C_r = C_1 - KC_2 = mx_1l_1 + ny_1l_1 - K(mx_2l_2 + ny_2l_2) = m(x_1l_1 - Kx_2l_2) + n(y_1l_1 - Ky_2l_2) \quad (2.9)$$

where C_r is the estimated reflection of skins that is assumed to be influenced by the absorption of melanin and hemoglobin. C_1 and C_2 are the detected reflections at two selected wavebands. K represents the ratio of weighted subtraction. m and n are the concentrations of the hemoglobin and melanin in the skin sample. l_1 and l_2 are the illumination intensities at two selected wavebands. x_1 and x_2 are the reflectance of hemoglobin at two selected wavebands. y_1 and y_2 are the reflectance of melanin at two

selected wavebands. By setting the value of K to be $y_1 l_1 / y_2 l_2$, the reflection of hemoglobin in the data can be extracted. By conducting similar weighted subtraction processing between blue light wavebands (band 0: 482nm, band 1: 494nm, band 2: 472nm, band 3: 465nm) and green light wavebands, the superficial melanin can be extracted.

In the real-time monitoring experiment, we extracted hemoglobin absorption information from multispectral images which were reconstructed from RGB-image sequences. From the results, we quantitatively analyzed the skin hemodynamics during heartbeat cycle and vascular occlusion. Furthermore, in the monitoring to vascular occlusion, besides the blood absorption, we also estimated oxygen saturation (SaO_2). In this case, oxyhemoglobin and deoxyhemoglobin are studied independently. The reflection is expressed as:

$$C_i = m_{oxy} x_i^{oxy} + m_{deo} x_i^{deo} + \alpha \tag{2.10}$$

where C_i is the detected reflection at the selected wavebands. m_{oxy} and m_{deo} are the concentrations of oxy and deoxyhemoglobin, respectively. x_i^{oxy} and x_i^{deo} are the corresponding reflectance coefficients of oxyhemoglobin and deoxyhemoglobin. α is a term that represents the light intensity losses caused by other chromophores, including melanin. We selected bands 4 (570nm), 5 (581nm) and 6 (556 nm) for the evaluation of SaO_2. Since the sensitive wavelengths in these bands are close to each other, we assumed that α is a constant in the processing. From equation (10), the SaO_2 can be evaluated as:

$$SaO_2 = m_{oxy} / (m_{oxy} + m_{deo}) \tag{2.11}$$

2.3 RESULTS

2.3.1 ANALYSIS OF SKIN MORPHOLOGICAL FEATURES AND REAL-TIME MONITORING USING SNAPSHOT MULTISPECTRAL CAMERA

A representative set of sub-channel images of skin captured by the multispectral camera under white light exposure is shown in Figure 2.2. All the bands were recorded simultaneously, which makes the data acquisition inherently immune to inter-spectral motion artifacts. Based on these subchannel images, weighted subtractions can be directly applied to extract the blood and melanin concentration information for morphological analysis. Furthermore, based on extracted blood absorption information, we conducted real-time monitoring of the variations in skin under various conditions, including heartrate cycle, the exercise recovery and the vascular occlusion.

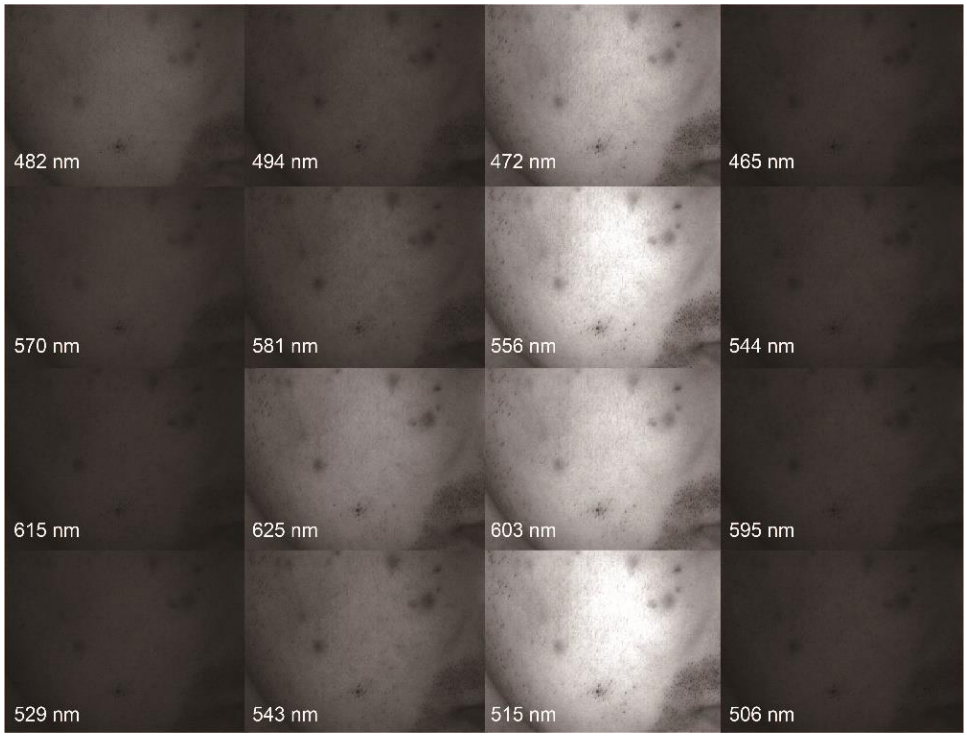

Figure 2. 2. Sixteen subchannel images captured by the multispectral camera from a volunteer skin under white light illumination.

There are several common types of skin features that can be analyzed from the multispectral images, including melanocytic nevus, pimples, nonmalignant red spots, etc. Some of them show abnormally high absorptions due to melanin, while others can be characterized by strong hemoglobin absorption. Therefore, in spatial morphological analysis, we conducted absorption mapping for these two chromophores to recognize skin features.

As a dominant chromophore in the blood, hemoglobin is associated with blood located in dermis and hypodermis, causing the redness appearance of the skin depending on its concentration. Since we need to capture the reflection images from the skin tissue beyond epidermis, green and red lights with deeper penetration are suitable for the hemoglobin analysis. To extract and enhance the contrast of hemoglobin information, the absorption caused by other chromophores, mainly melanin, should be minimized or eliminated. From green-wavelength band around 550 nm to red wavelength band over 600 nm, the absorption efficiencies of melanin and hemoglobin vary in different trends (Figure 2.1d). Therefore, with a suitable ratio, the weighted subtractions between green and red subchannels are applied to extract the hemoglobin absorption information from the melanin absorption. The subtraction ratios in experiments were calculated with equation (1) and calibrated according to the different band sensitivities of the camera. The blood absorption extraction results are shown in Figure 2.3. Three cases of initial images (band 10 extracted from the multispectral raw images) under white light illumination are shown in Figure 2.3(a). In Figure 2.3(a)-1, both melanocytic nevi and pimples exist on the skin. In Figure 2.3(a)-2, there is a light red spot on the cheek and a nevus on the right corner of the mouth. There are only pimples on the skin in Figure 2.3(a)-3. The corresponding results of extracted

blood absorption information from weighted subtractions are shown in Figure 2.3(b). It can be observed that melanocytic nevi and some other features with large amounts of melanin, including hairs, eyebrows, eyelashes, and beards, are all eliminated in the extracted hemoglobin absorption information maps. The red spots represent the positions where there is high hemoglobin content and their locations match well with corresponding features in raw data, which can be verified in overlaid images in Figure 2.3(c). To fully utilize the multiple subchannels, we applied summation operation among the blood absorption information maps from three subchannels combinations to realize contrast enhancements. Three cases of weighted subtraction results from combination 2(band11(529 nm)/10(603 nm)) (Figure 2.3(d)) and combination 3(band 6 (556 nm)/8 (615 nm)) (Figure 2.3(e)) are added together with combination 1 (band 6(556 nm)/9(625 nm)) in Figure 2.3(b), the results are shown in Figure 2.3(f).

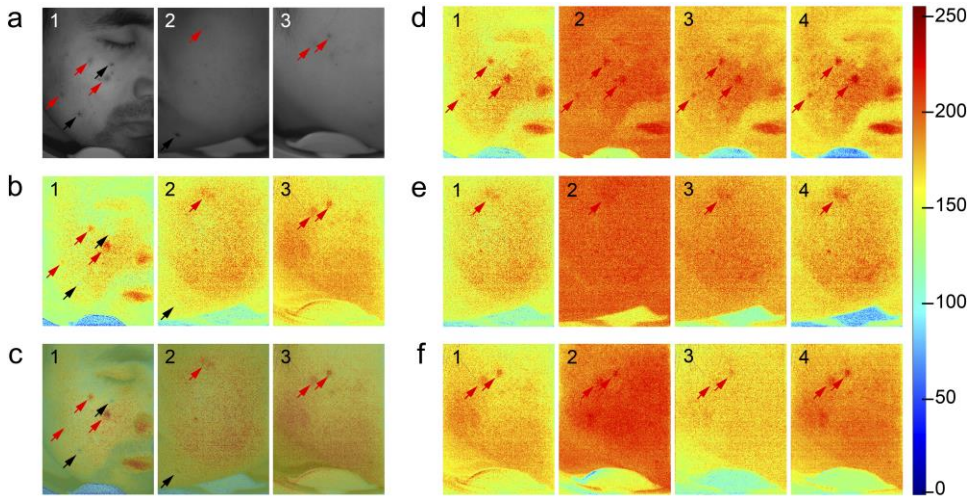

Figure 2. 3. Extraction of blood absorption information content from snapshot multispectral image.
(a) The raw images directly exported from the spectral band 10 in the camera, from three volunteers (marked as 1, 2, and 3, respectively). (b) Corresponding images showing blood absorption information content derived from the weighted subtraction between band 6 (556 nm) and 9 (625 nm), (c) Overlaid images of raw images and corresponding blood

absorption images. (d) Corresponding images derived from weighted subtractions between band11(529 nm) and 10(603 nm). (e) Corresponding images derived from weighted subtractions between band 6 (556 nm) and 8 (615 nm). (f) Contrast enhancements of the blood absorption information content by summing the images showing in (b), (d) and (e). 1,2,3 represent three different cases in the blood extraction. Red arrow: pimples or light red spots, black arrow: melanocytic nevi.

Skin melanin is produced by melanocytes and normally exists in the melanosomes that are distributed in the upper part of the keratinocytes. Therefore, the melanin absorption information can be extracted from superficial skin, which was realized by subtractions between blue and green channels. In our method, bands 6 (556nm),7 (544nm),12 (529nm) and 13 (543nm) were selected and alternately subtracted from bands 0 (482nm), 1 (494nm), 2 (472nm) and 3 (465nm) to show the melanin absorption. The subtraction ratios were manually adjusted based on the normalization of band sensitivities and absorption coefficients to exclude the interference of hemoglobin. As shown in Figure 2.4, we conducted melanin absorption information extraction on three cases and two of them are the left and right faces from the volunteer. In these cases, pimples, red spots and melanocytic nevi mixed together in the field of view (Figure 2.4(a)). Through the weighted subtraction between blue and green bands, the melanocytic nevi stand out from other features, which are represented in Figure 2.4(b). It is observed that pimples and light red spots are eliminated from the melanin absorption images. The locations of extracted spots and nevi are in accordance with raw data, which can be checked in the overlaid images in Figure 2.4(c). Meanwhile, we also conducted summations to melanin absorptions from different subchannel combinations to enhance the contrast and the results are shown in Figure 2.4(d-f).

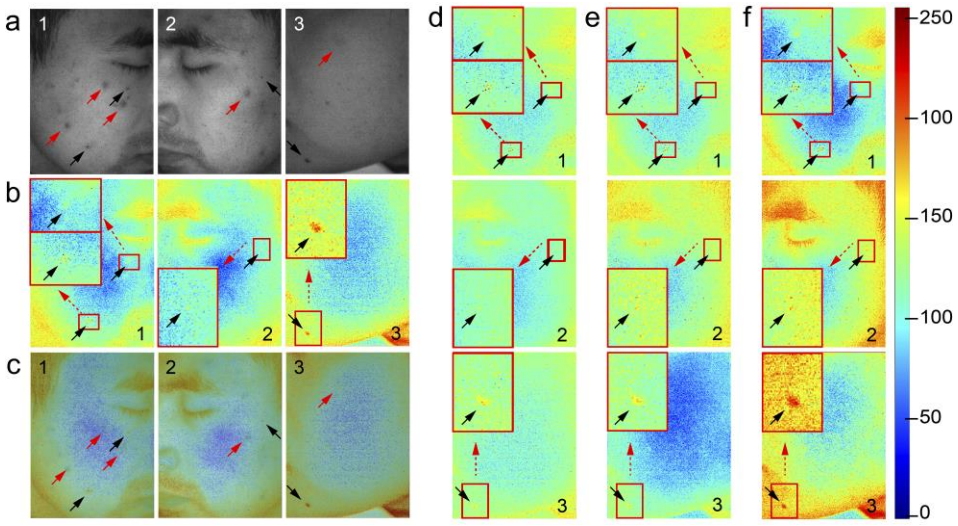

Figure 2. 4. Extraction of melanin absorption information content from snapshot multispectral image.

(a) The raw images directly exported from the spectral band 10 in the camera, from three volunteers (marked as 1, 2, and 3, respectively). (b) Corresponding images showing extracted melanin absorption information content derived from weighted subtraction between bands 0(482 nm) and 12(543 nm). (c) Overlaid images of raw images and corresponding melanin absorption images. (d) Corresponding images derived from weighted subtractions between bands 0(482 nm) and 11(529 nm). (e) Corresponding images derived from weighted subtractions between bands 0(482 nm) and 7(544 nm). (f) Contrast enhancements of the melanin absorption information content by summing the images showing in (b), (d) and (e). 1,2,3 represent three different cases in the melanin extraction. The insert in each panel is zoomed view of the regions as marked to show more details. Red arrow: pimples or light red spots, black arrow: melanocytic nevi.

Besides the capability of extracting spatial morphological features, the multispectral imaging system would be also amendable to monitor the skin activities in real time due to its snapshot nature of image capturing, thanks to the multispectral camera. Below we demonstrate, by examples, the temporal analysis in heartrate measurements, exercise recovery, and vascular occlusion. The derived information due to blood absorption was used as a metric in the visualization and assessment of temporal responses of skin tissue.

We operated the imaging system in video mode and collected a series of images during a time period for temporal analysis. The framerate was at 10 fps and the imaging duration lasted for 60s. Afterwards, the summation of the extracted information content due to blood absorption within the cheek region (square-box marked in Figure 2.5(a)) was calculated and used as the blood absorption index for every frame along the time axis. Then, we Fourier-transformed the temporal profile of the blood indices over 60 s duration to show the frequency variation within the profile. As shown in Figure 2.5(b), a frequency peak at around 1.19 Hz was reliably detected, which corresponded well to the heartrate. To verify the result, we carried out reference measurements with a pulse sensor and data-logger device (PowerLab 4/30, ADInstruments) during multispectral imaging and the result is shown in Figure 2.5(c). It is clear that the heartrate frequency, indicated by the first dominant frequency peak, matches very well with the result from our multispectral imaging system.

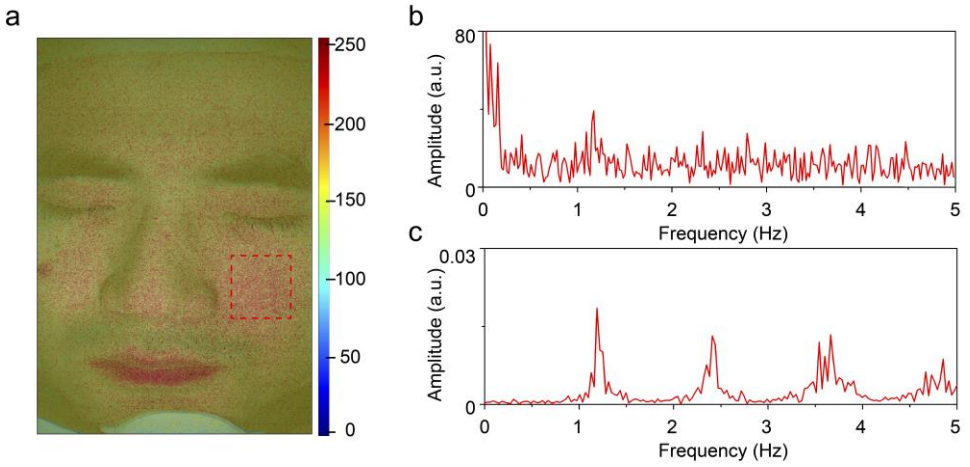

Figure 2. 5. Heartrate measurement with snapshot-multispectral-camera-based multispectral imaging system.
(a) The overlaid face skin image of raw image with the derived map of hemoglobin absorption information (coded according to the color bar shown in the right). The red dotted box area on the cheek is the target area for extracting heartrate from blood absorption information content derived

from the multispectral imaging. (b) The frequency spectrum of temporal profile of blood absorption information content summed within the red-box region in (a). (c) The heartrate reference from the PowerLab pulse sensor.

By lengthening the time period of imaging, real-time monitoring of the skin performance in some daily activities, like exercises and fitness, may be realized. Herein, the recovery process of volunteer's face-skin performance after he jumps up and down for ~100 times had been monitored and analyzed. We selected the left facial skin as the imaging site and conducted a video recording, which lasted for 6 minutes. The blood absorption information content was extracted for every frame. As shown in Figure 2.6(a), the blood absorption information maps and corresponding overlaid images with the raw photograph at 0,3,6 minutes during the exercise recovery process are presented, where it is observed that the information about blood absorption declines as the increase of recovery time. The real-time temporal profile of absorption information summed within the marked region of the cheek area is shown in Figure 2.6(b). Obviously, the signal strength shows a rapid decrease within the 6-minute period. Furthermore, from 2 minutes to 6 minutes, we separated the recovery temporal profile into 5 segments and each one lasted for 1 minute. Within each segment, Fourier transform was performed, upon which to extract the heartrates (Figure 2.6(c)). The heartrates are 1.56 Hz, 1.53 Hz, 1.51 Hz, 1.49 Hz and 1.46 Hz for 5 segments respectively. We can see that the heartrate slow-down from 2 minutes to 6 minutes, and then gradually into a resting state value, which is in accordance with our common sense.

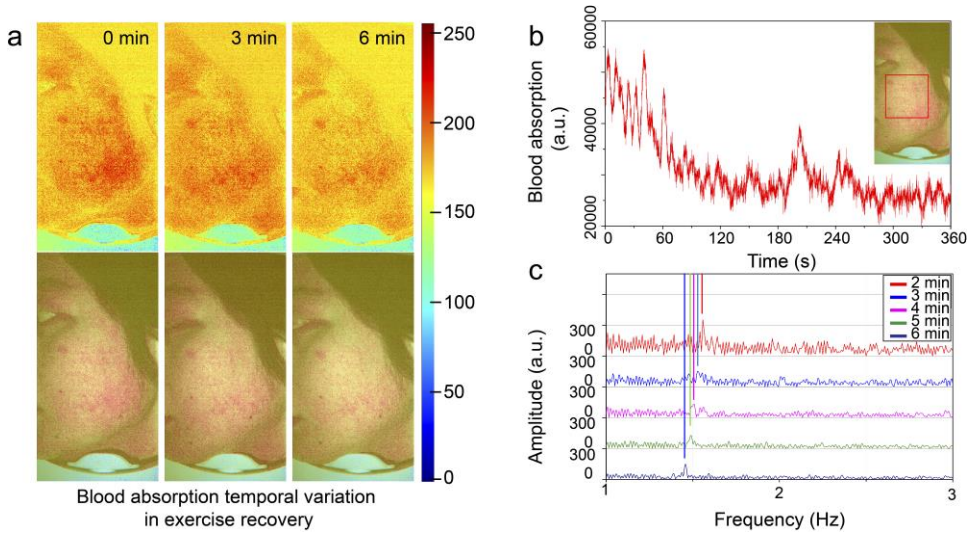

Figure 2. 6. Exercise recovery monitoring with the snapshot-multispectral-camera-based multispectral imaging system.
(a) The hemoglobin absorption information map (top row, color-coded according to color bar shown in the right) and overlaid images (bottom row) of the left facial skin at different time points of the recovery. (b) Real-time response curve of blood absorption information content during exercise recovery. The red dotted box area on the left is the targeted region for analysis. (c) The heartrate measurements of 5 recovery segments at 2, 3, 4, 5 and 6 minutes, respectively.

The vascular occlusion would lead to the blood perfusion variations that can be detected from the blood absorption information content extracted during multispectral imaging. Here, we demonstrate its feasibility by monitoring subcutaneous vascular occlusion with the skin tissue. We selected fingers as the test site for the vascular occlusion study because occlusion can be easily realized by applying outside pressures and different fingers can act as control groups to each other. In the experiments, we used the thin rubber ring to provide outside pressures to apply vascular occlusions on the skin. In Figure 2.7(a), the rubber ring worked on the mid-finger and forefinger respectively to provide effective pressure to occlude the skin perfusion. The rubber ring was banded on the mid-finger at 60s and removed at 150s. After recovering for around 120s, the banding was applied on the forefinger at 280s and relieved at 360s. From the blood absorption images at 120s and 300s,

it is observed that the pressure applied on the skin caused rapid reductions of blood perfusion. After the relief of the banding, the skin blood perfusion showed a short-time over-rebounding and then recovered to the similar levels with other control group fingers, as shown in the images at 160s, 240s, 390s, and 480s. To clearly present the quantitative variation during pressure-induced perfusion occlusion, we conducted quantitative measurements to the fingers. We selected five positions (marked as A, B, C, D, E, shown in top left image of Figure 2.7a) on the dorsal skin of the finger and summed the blood information content within the marked tissue region. The temporal variation curves are shown in Figure 2.7(b). Position B (mid-finger) and C (forefinger) represent the experiment groups and others are control groups. The blood absorption information content as derived from multispectral imaging is apparently declined at the mid-finger and the forefinger under the applied pressure. The recovery processes also match with the images in Figure 2.7(a). In contrast, they are generally stable during the time period.

The SaO_2 images (Figure 2.7(c)) and quantitative curves (Figure 2.7(d)) during the pressure-induced vascular occlusion show similar variation with the derived blood absorption information as shown in Figure 2.7(a) and Figure 2.7(b). The SaO_2 intensities showed sharp decrease after rubber ring banding at 60s on the mid-finger and 280s on the forefinger. Before removing the rubber ring, the SaO_2 intensities stayed in relatively low levels. After removing the rubber ring at 150s on the mid-finger and 360s on the forefinger, the SaO_2 intensities showed quick over-rebounding in a short time and then slowly regressed to normal levels.

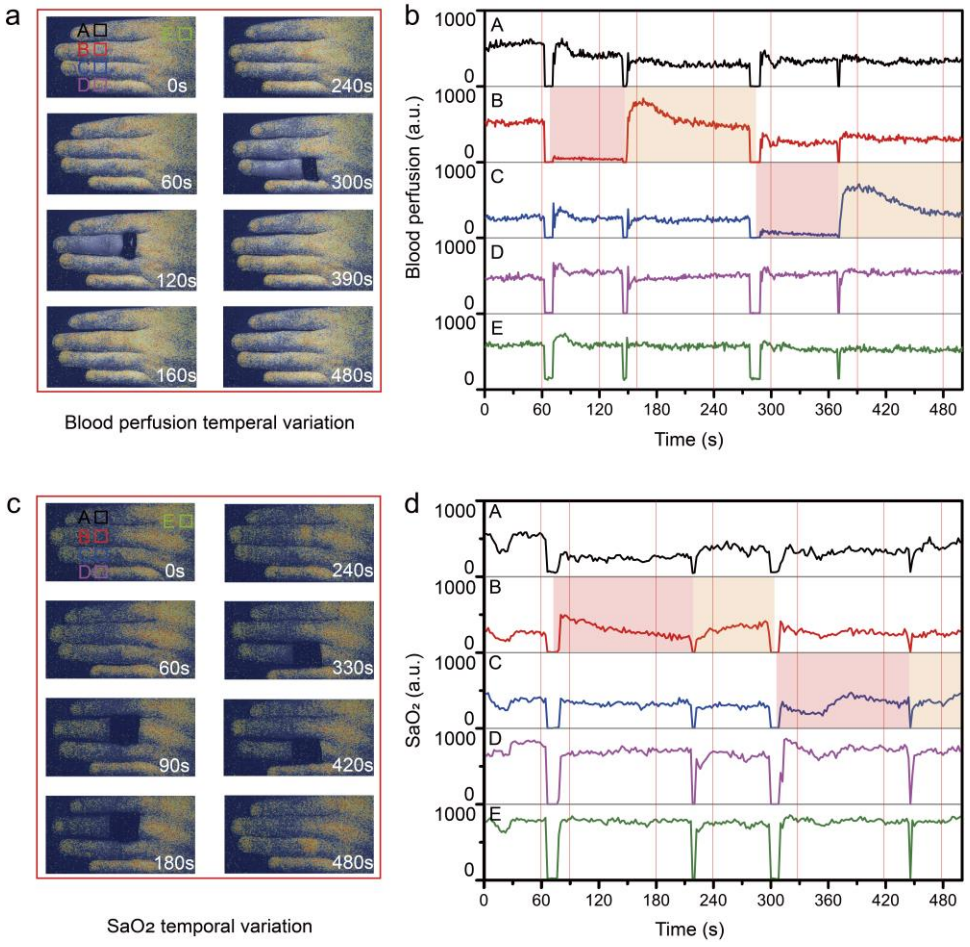

Figure 2. 7. Vascular occlusion monitoring with the snapshot-multispectral-camera-based multispectral imaging system.
(a) Finger dorsal skin blood absorption images at different time points of vascular occlusion under the outside pressure. (b) Real-time quantitative blood absorption response curves of fingers under the vascular occlusion and the contrast groups. (c) Finger dorsal $_{SaO_2}$ images at different time points of vascular occlusion under the outside pressure. (d) Real-time quantitative $_{SaO_2}$ response curves of fingers under the vascular occlusion and the contrast groups.

2.3.2 MULTISPECTRAL RECONSTRUCTION OF SMARTPHONE CAMERA

To investigate the reconstruction performance, we reconstructed RGB images of 100 color blocks from the color chart into multispectral images with Wiener estimation matrix. For each color block, we calculated the average value of relative errors of 16 subchannels between initial and reconstructed multispectral reflectance. The averaged relative errors of

100 color blocks are shown in Table 2. The maximum, minimum and average values are 10.950%, 0.424% and 4.933%, respectively. Relative errors of the reconstruction are higher in some color blocks, mainly in some blocks with dark cold tones. The underexposure in blue and green wavebands caused by the relative lower power intensity around 500nm of the light source can be the main factor. To show the reconstruction in more details, we selected 3 representative samples, including the one with maximum reconstruction error, the one with minimum reconstruction error and the one with reconstruction error close to the average value of 100 color blocks, and compared their initial and reconstructed reflectance in 16 wavebands, showing in Figure 2.8. Note that the reflectance in each waveband was averaged from data in the central area, which is one fourth of the total area of corresponding color block. The results indicate that reconstructed multispectral images from RGB images match well with initial multispectral images.

Table 2. 2. Relative errors between initial and reconstructed multispectral reflectance of 100 color blocks.

4.505%	6.659%	6.680%	7.090%	3.755%	5.159%	3.159%	3.248%	2.136%	2.592%
4.328%	5.567%	4.516%	4.620%	1.747%	2.604%	1.226%	0.871%	0.696%	0.596%
4.753%	8.695%	8.920%	8.533%	5.541%	7.577%	5.552%	6.514%	5.979%	6.256%
7.535%	10.950%	10.825%	10.201%	7.668%	9.491%	7.605%	8.637%	8.354%	8.731%
5.947%	9.164%	8.419%	7.298%	4.454%	5.913%	3.299%	4.183%	3.775%	4.230%
5.979%	8.886%	7.779%	6.439%	3.594%	4.946%	2.063%	2.928%	2.586%	3.135%
6.311%	8.728%	7.481%	5.977%	3.190%	4.543%	1.443%	2.371%	2.372%	2.989%
6.276%	8.588%	7.325%	5.792%	2.978%	4.274%	1.415%	2.051%	2.131%	2.741%
4.489%	7.148%	5.913%	4.400%	1.589%	2.468%	1.568%	1.060%	0.464%	0.424%
4.688%	7.509%	6.973%	5.930%	2.961%	4.075%	1.755%	1.885%	1.751%	2.150%

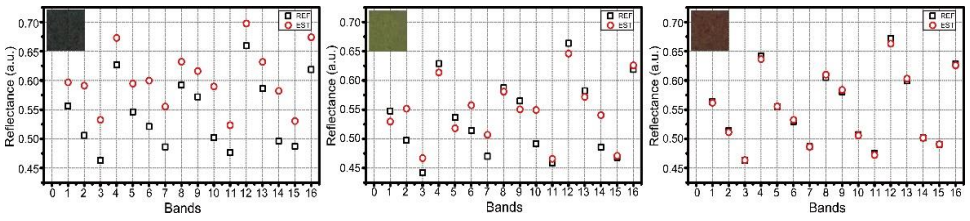

Figure 2. 8. Comparison of reflectance in 16 wavebands of reconstructed multispectral images from RGB images with initial multispectral images from snapshot multispectral camera.
Shown are 3-representative color blocks. The relative error between initial and reconstructed multispectral reflectance of the color blocks in the left, medium and right are 10.95% (the maximum reconstruction error), 4.946% (close to the mean error) and 0.424% (the minimum error) respectively. Black box symbol represents the reflectance from initial multispectral images; Red circle symbol corresponds to the reflectance of reconstructed multispectral images. The insert of each panel is the RGB image of selected color block.

2.3.3 ANALYSIS OF SKIN MORPHOLOGICAL FEATURES AND REAL-TIME MONITORING USING SNAPSHOT-ENABLED MULTISPECTRAL IMAGING

Under dark environment, we conducted skin imaging to a volunteer with a smartphone, showing in Figure 2.9(a). The illumination was provided by the built-in flashlight and the smartphone camera was used to acquire images. These settings were the same as the calibration steps when using the smartphone flashlight as the illumination source. By stabilizing the illumination condition, the accuracy of the multispectral reconstruction was ensured. The RGB-mode image of the facial skin was shown in Figure 2.9(b). There are redness and moles in the field of view. The RGB-mode image was reconstructed into multispectral images with Wiener estimation matrix as described above. The reconstructed data consisted of 16 wavebands, simulating the multispectral images as if they were captured by the snapshot multispectral camera. Blood vessels are localized within relatively deep skin tissue so that lights with longer penetration depth are suitable for detection. Therefore, we applied weighted subtractions between green- and red-light

wavebands to extract hemoglobin absorption information. The extracted blood absorption map is shown in Figure 2.9(c), where redness spots (red arrow) are significantly contrasted from other features. Afterwards, we extracted melanin absorption with weighted subtractions between blue and green bands because melanin exists in superficial layer of the skin. Figure 2.9(d) shows the absorption map of melanin. As expected, the hemoglobin-related features are significantly weakened while the nevi (black arrows) are enhanced in this map.

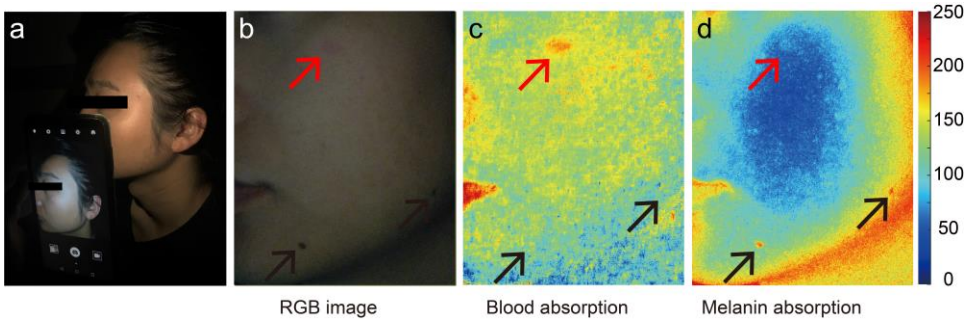

Figure 2. 9. The image acquisition and extraction of blood and melanin absorption information content from multispectral reconstruction with the RGB image from a smartphone camera with illumination from built-in flashlight.
(a) Photography during image acquisition with the smartphone camera and built-in flashlight. (b) Initial RGB-mode image of the facial skin captured by the smartphone camera. (c) Blood absorption information map. (d) Melanin absorption information map. Red arrow: skin redness; Black arrow: moles. Blood and melanin absorption maps are coded according to the color bar shown in the right.

To compare the skin analysis performance of the RGB-camera-based multispectral imaging system and snapshot multispectral camera, we imaged the same skin area with two cameras and conducted the same processing. Melanin absorption information was extracted and compared as an example (Figure 2.10). Figure 2.10(a) shows the raw image from the band 9 in the snapshot multispectral camera. The extracted melanin absorption map from the images captured by multispectral camera is shown in Figure 2.10(b), where

the details of two moles (marked by square boxes) are shown in the zoomed-in images (Figure 2.10(c) to 10(d)). Analyses of images captured by the smartphone resulted in melanin absorption map shown in Figure 2.10(f). Figs.2.10(g) and 10(h) are the zoomed-in view of the two moles, marked by square boxes in Figure 2.10(f). Since the smartphone camera has many more pixels than the snapshot camera, the melanin absorption map in Figure 2.10(f) performs much better in terms of image resolution. From the zoomed-in images, we can see that two moles absorption spots from smartphone-based system (Figure 2.10(g) to 10(h)) show clear edges and sizes. However, these characteristics are not clearly depicted by the snapshot multispectral camera largely due to its limited spatial resolution. It is worth noting that the unexpected high contrast in the skin area below the mandible (i.e. jaw) was caused by the curvature of skin surface that makes the reflectance measurement not uniform (typically low) at that area.

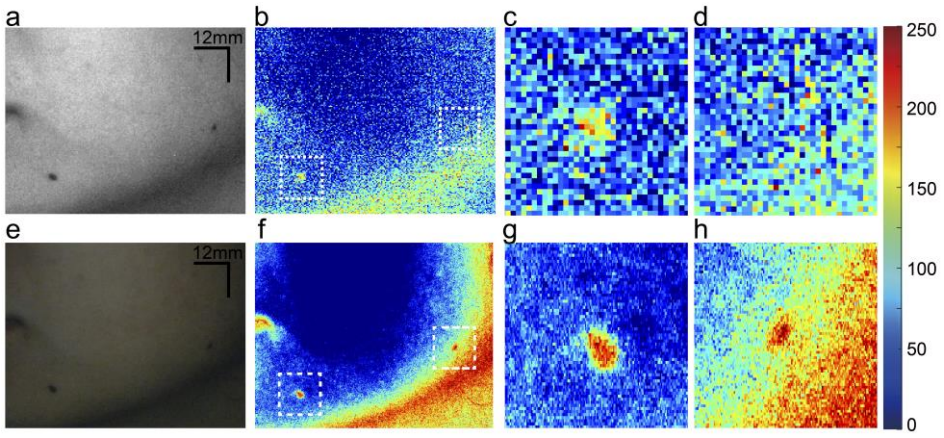

Figure 2. 10. Comparison of the imaging performance between snapshot multispectral camera and smartphone-based multispectral reconstruction. (a) Raw image of the facial skin with moles from band 9 of snapshot multispectral camera. (b) Extracted melanin absorption map from snapshot multispectral camera. (c) Zoomed-in view of the left white box area of (b). (d) Zoomed-in view of the right white box area of (b). (e) Raw RGB image of the same facial skin captured by the smartphone camera. (f) Extracted melanin absorption map from the smartphone camera. (g) Zoomed-in view of the left white box area of (f). (d) Zoomed-in view of the right white box

area of (f). Blood and melanin absorption maps are coded according to the color bar shown in the right.

In our smartphone-based multispectral imaging and analysis method, as long as the illumination is controlled to be generally stable, various types of light sources are applicable in this system. Besides the smartphone flashlight, one of other types of regular light sources, the fluorescent lamp, was tested in our study as well. Before imaging, we re-conducted the calibration steps under the fluorescent lamp illumination and calculated the new Wiener estimation matrix. Then, we used the same smartphone to image volunteer's facial skins and conducted similar reconstruction and processing for the captured RGB images. We selected and presented analysis results of two parts on the left facial skin in Figure 2.11. Figure 2.11(a) shows the initial RGB-mode image from the smartphone camera under the fluorescent lamp illumination, where there are pimples and moles in the field of view. The reconstruction and processing resulted in absorption information maps of hemoglobin and melanin, showing in Figure 2.11(b) to 5(c), respectively. To clearly show the analysis performance of different skin features, we zoomed in a small target area (the red-box area in Figure 2.11(a)), to provide the detailed visualization in Figure 2.11(d) to 5(f). Figure 2.11(e) to 5(f) clearly shows that the pimple (red arrow) is of higher blood content while the mole has higher melanin content. The lower part of the facial skin features one mole and many skin redness instead of pimples. With similar steps, the initial RGB image, the extracted absorption maps of hemoglobin and melanin and corresponding zoomed-in details of main features are shown in Figure 2.11(g) to 5(l), respectively. The results in Figure 2.11 verified that fluorescent lamp can also be used as illumination source in the smartphone-based multispectral imaging.

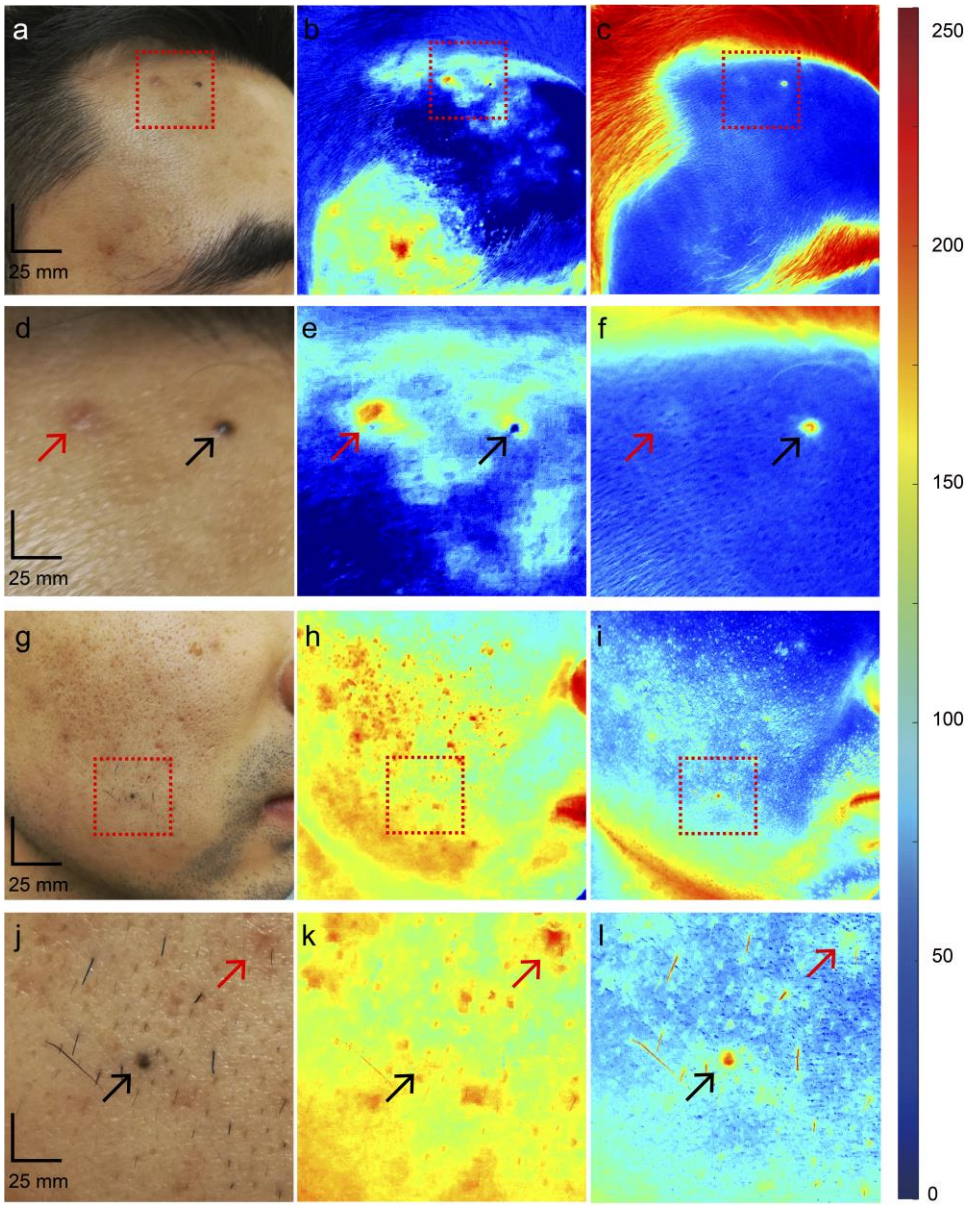

Figure 2. 11. Extraction of blood and melanin information content from multispectral reconstruction with the RGB images captured by a smartphone camera under the fluorescent lamp illumination.
(a) Initial RGB image of upper facial skin captured by the smartphone. (b) blood absorption map and (c) melanin absorption map of the facial skin, with pimples and moles. Figure 2.11(d)-5(f) Zoomed-in views of the target areas in red box of Figure 2.11(a)-5(c), respectively. (g) Initial RGB image of lower facial skin captured by the smartphone, (h) blood absorption map and (i) melanin absorption map of the facial skin, with pimples and moles. Figure 2.11(j)-5(l) Zoomed-in views of the target areas in red box of Figure 2.11(g)-5(i), respectively. Red arrow: skin redness or pimples; Black arrow:

moles. Blood and melanin absorption maps are coded according to the color bar shown in the right.

Following the cycle of heart contraction and expansion, the blood supply in the body appears pulsatile. Therefore, by monitoring the change of blood absorption intensity in skin tissue, the heartbeat may be detected[58]. In the experiment, we used a fixed support to keep the facial skin stable during the video recording process and provided illumination with the smartphone flashlight, showing in Figure 2.12(a). We extracted the blood absorption map from every frame in the video. From the blood absorption map in Figure 2.12(b), we can see higher blood absorption intensities at the areas of lips, eye socket and ear positions than other areas, matching with our common senses. To test whether it is possible to evaluate the heart rate from the time series of blood information maps, we summed the signals of blood absorption map on whole facial skins for each frame in the whole video. We then conducted Fourier transform of the time series of temporal variation data. This process resulted in a plot in the frequency domain (black curve in Figure 2.12(c)), where the main frequency peak around 1.05 Hz is identified, which we believe is the heart beat frequency. As a proof, we used a pulse sensor and data-logger device (PowerLab 4/30, AD Instruments) to provide reference heart rate measurements during imaging. The result is shown in red curve in Figure 2.12(c) where a heart-beat frequency at 1.05 Hz is identified, exactly matched with the measurement from smartphone camera. This demonstrates that our monitoring has successfully captured heart rates in the heart cycles.

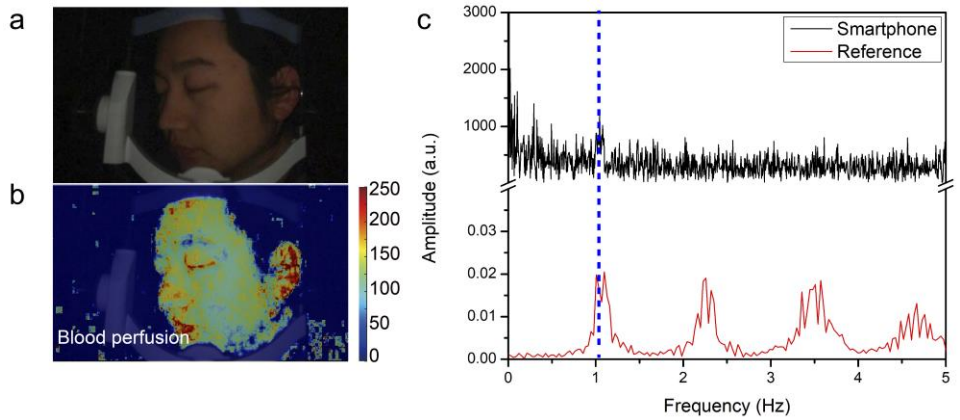

Figure 2. 12. Heart Rate measurement with the smartphone-based multispectral imaging system.
(a) One frame extracted from the RGB mode video in facial skin monitoring with the smartphone camera under flashlight illumination. (b) The derived map of blood absorption information (coded according to the color bar shown in the right) overlaid with the raw grey-scale RGB image in (a). (c) Black curve: The frequency spectrum of temporal profile of blood absorption information content. Red curve: The heart rate reference from the PowerLab pulse sensor.

Vascular occlusion monitoring is useful in the assessment of some clinical procedures, like skin grafting[59], and monitoring in rehabilitations, like the pressure sores monitoring[60]. In this study, we applied outside pressures with rubber ring on a volunteer's mid-finger to create a vascular occlusion. We kept the pressure for 60 seconds and then released it. The pressure-on and recovery processes were recorded by the smartphone camera. The illumination was provided by the smartphone flashlight. We extracted one RGB frame at 60s in the video (Figure 7(a)) and reconstructed it into the multispectral image. Figure 2.13(b) shows the blood absorption map extracted from the reconstructed multispectral image. The oxygen saturation map was extracted as well and shown in Figure 2.13(c). Compared with other fingers, the mid-finger under pressures shows lower blood absorption and oxygenation intensities. The correlation coefficient between the blood absorption map and the oxygen saturation map is calculated to be 0.9430,

which means these two indices are highly related. The oxygenation status in the healthy tissue is macroscopically stable, except for the periodical variation caused by the heart cycle. The different intensities in the oxygenation map may be due to the density and locations of the vascular components in the corresponding area, upon which to determine the blood absorption mapping in our study. The supply of blood to the occluded skin area was reduced, leading to the decrease of both blood volume and oxyhemoglobin. We selected the dorsal skin on the middle digits of five fingers as the ROI. The field of view was ~10x20 mm. During video recording, measures were taken to stabilize the hand and fingers to minimize the motion artifacts. For every frame in the video, we summed blood absorption and oxygen saturation intensities in the ROI (shown in the color box areas Figure 2.13(a)) on five fingers. The temporal blood absorption and oxygen saturation intensity variation curves were normalized and presented in Figure 2.13(d) and (e), respectively. In the mid-finger curves, both blood absorption and oxygen saturation intensities are relatively lower with pressures on. After releasing the rubber ring at around 60s, the intensities in both two curves show a rapid over-rebounding and then a slow regression to a stable level. However, in control groups, which consists of other four fingers, blood absorption and oxygen saturation intensities are more stable during the monitoring.

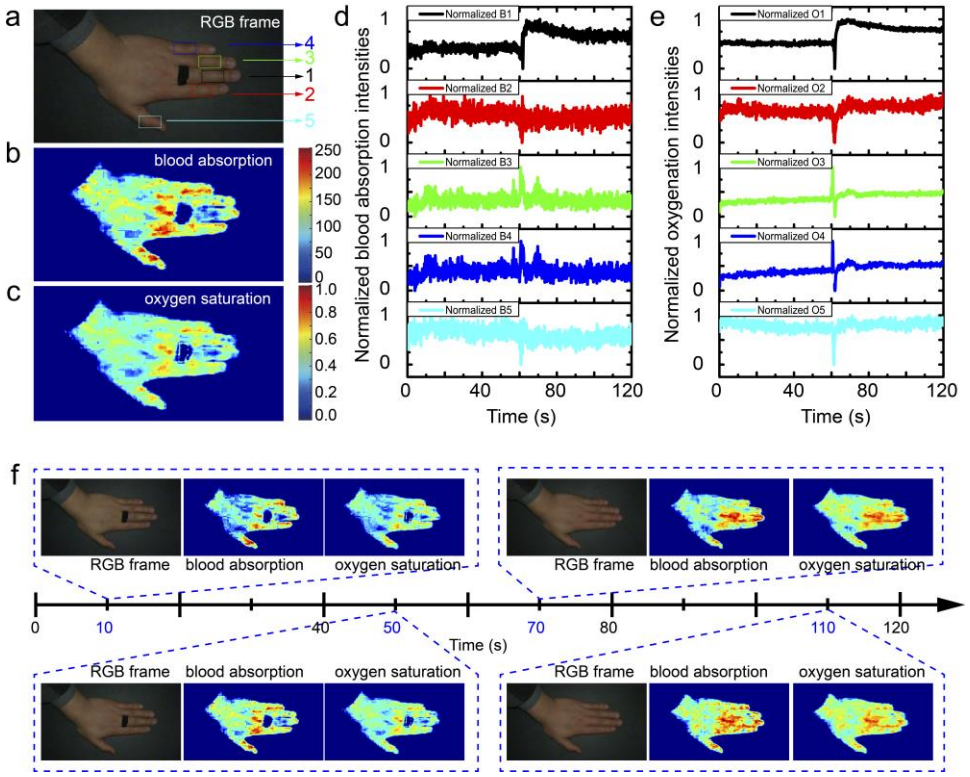

Figure 2. 13. Vascular occlusion monitoring with the smartphone-based multispectral imaging system.
(a) Representative RGB frame at 60s from the monitoring video during vascular occlusion on the middle finger. (b) Blood absorption map at 60s extracted from multispectral reconstruction based on the RGB frame in (a) (color-coded according to color bar shown in the right). (c) Oxygen saturation map at 60s extracted from multispectral reconstruction based on the RGB frame in (a) (color-coded according to color bar shown in the right). (d) Real-time response curves of blood absorption intensities on middle finger during vascular occlusion. The intensities were normalized summations of blood absorption intensities in corresponding color box areas in (a): Experiment group: black curve: box 1, mid-finger. Control group: red curve: box 2, forefinger; green curve: box 3, index finger; blue curve: box 4, little finger; teal curve: box 5, thumb. (e) Real-time response curves of oxygen saturation intensities on finger skins during vascular occlusion. The intensities were normalized summations of oxygen saturation intensities in corresponding color box areas in (a). Experiment group: black curve: box 1, mid-finger. Control group: red curve: box 2, forefinger; green curve: box 3, index finger; blue curve: box 4, little finger; teal curve: box 5, thumb). (f) Visualization of RGB frames, blood absorption maps and oxygen saturation maps at 10s, 50s, 70s and 110s from the monitoring video to vascular occlusion on middle finger. Blood absorption maps were color-coded according to color bar shown in (b).

Oxygen saturation maps were color-coded according to color bar shown in (c).

To provide visualized proofs to these variations, we intercepted four frames at around 10s, 50s, 70s and 110s in the video to extract the blood absorption and oxygenation maps. The initial RGB-mode frames, blood absorption and oxygen saturation maps are respectively listed in Figure 2.7(f). As expected, the blood perfusion and oxygenation on the mid-finger at 10 and 50s were relatively weaker than other fingers. At 70s, these two indices are relatively higher than other fingers. Finally, at 110s, the blood absorption and oxygenation intensities regressed to the similar level with other fingers. These results demonstrate that our smartphone-based multispectral imaging method could be applicable in hemodynamic monitoring of the skin vascular occlusion.

2.4 DISCUSSION AND CONCLUSION

Commercial smartphones have experienced a booming development in the past ten years. Up to 2019, there are 2.71 billion of smartphone users worldwide. Following the development of smartphone, smartphone camera is also being increasingly advanced, especially in its imaging quality, fidelity, resolution and speed. Some flagship smartphones equip cameras with 12 million pixels and can achieve video recording at 60 fps. Under some special setups, like slow motion modes, some smartphone cameras can even realize high-speed recording at 960 fps. All these advancements make the smartphone-based imaging method attractive in providing cost-effective skin assessments with high spatial and temporal resolution.

Chromophores, mainly hemoglobin and melanin, in the skin tissue are the dominant factors which have potential impacts on the skin assessments, both in clinical dermatology and cosmetics. Hemoglobin concentration is related to the features like skin redness,

inflammations and vascular abnormalities. Melanin variation often presents in skin pigmentations, nevus and some skin cancers[61]. Recently, multispectral imaging provides a strategy with both spectral analysis and snapshot visualization abilities, which has shown the attractive potential to be more widely used in the skin assessments.

Our study aims to provide a smartphone-based multispectral imaging system for the skin assessments. Since the RGB mode of smartphone cameras lacks enough wavebands and spectral resolutions to properly conduct multispectral analysis, we innovatively applied Wiener estimation to transform RGB images captured by the smartphone camera into the multispectral images. While there may be other more efficient and optimal methods, we selected Wiener estimation in our study. We showed that Wiener estimation has been promising in providing accurate and high-resolution multispectral reconstruction. We note that such reconstruction using Winer estimation relies on the training of a big set of samples, requiring independent measurements to the spectral reflection of each sample.

The spectral calibration would be ideally conducted by the use of high-resolution spectrometers. However, in doing so, the calibration process would suffer extremely high workload and perhaps instabilities because it has to be done at each wavelength one by one. To mitigate this prohibitive and tedious task, we used a state-of-the-art snapshot multispectral camera with 16 wavebands ranging from 470nm to 620nm to provide spectral reflection calibration. With this camera, the measurements of multiple wavelengths, multiple samples and the co-registration of sampling area in each sample can be easily achieved by selecting and calculating corresponding areas of the color chart in the RGB and multispectral images. Therefore, the calibration is realized by taking RGB and multispectral images of the color chart under the same illumination, dramatically reducing

the tedious workload in the process and increasing the stability of calibration. However, like traditional calibrations with spectrometers, the effectiveness of our calibration and training is also limited for practical applications because the same illumination condition is required. An alternation of ambient lights may require re-calibration.

The calibration process resulted in a Wiener estimation matrix that is used to transform the RGB images into multispectral images. Since it is done through pixel by pixel, the reconstructed multispectral images possess the same spatial pixel resolution as the original RGB images (typically around 800 million spatial pixels), and each pixel bearing spectral information with 16 wavebands in visible range. With weighted subtractions between different wavebands, the target chromophores were contrasted from surrounding tissues. Coupling with above multispectral reconstruction and post-processing steps, we showed the smartphone camera's abilities to visualize blood, melanin absorption maps and oxygen saturation in the facial skin. Besides, the extraction and separation of chromophores could provide an ability of smartphone-based system to quantitatively analyze and monitor the skin temporal activities (however, it should be understood that this is still an estimation). Compared with conventional multispectral imaging system, which mostly relies on lasers or tunable optical filters, the smartphone-based multispectral imaging system eliminates the internal time difference within frames, greatly improving the imaging speed and immunity to motion artifacts. Furthermore, compared with advanced and costly multispectral cameras, the smartphone based multispectral imaging is superior in terms of its spatial resolution. In addition, our method shows flexibility in terms of different illumination conditions. The smartphone flashlight and the daily-used fluorescence lamps are all applicable in this strategy. Most importantly, our strategy does not require any

modification or addition to the existing smartphones, which makes multispectral imaging and analysis of skin tissue possible in daily scenes out of labs. This may be particularly important and appealing for the inhabitant regions where the resource-settings are relatively low.

We have conducted the analyses of regular skin features, like pimples and nevus, to provide proof of concept for the feasibility and advantages of smartphone-based multispectral imaging system and methods. If properly developed, we believe that this method would be also applicable to facilitate the diagnosis and prognosis of some other dermatosis with chromophore abnormalities, like malignant melanoma[62]. In addition, the smartphone-based operation would hold the enormous promises in cosmetic applications, where the assessments of the UV spots and the skin hyperpigmentation[63] are often needed. In the future, related mobile applications of skin assessments may be developed as the APPs for the smartphones, and consumers may utilize them to conveniently conduct self-analyses of their own skin conditions.

There is often lack of scientific devices and instruments for multispectral imaging in the low-resource setting regions. However, due to the explosive growth of mobile communication techniques, smartphone becomes widely used, even in the developing countries and rural areas. Our study introduces the use of low-cost smartphone to realize multispectral analysis of the skin, providing an opportunity for users to achieve skin assessments. The popularity of smartphones makes the proposed multispectral imaging useful in daily cosmetic and dermatologic applications. In addition, the multispectral reconstruction may also be applicable to other imaging techniques, such as microscopy and fluorescent imaging, to extract more sensitive information of interest from the typical RGB

images. However, the calibration settings and steps as discussed in this paper still require further improvement and optimization so that it can be easily deployable to ordinary smartphones, including illumination during the calibration and imaging.

We have proposed a smartphone-based multispectral imaging system and corresponding post-processing methods for the skin analysis and monitoring. Using Wiener estimation strategy, RGB-mode skin images acquired by the smartphone camera were reconstructed/transformed into multispectral images with 16 wavebands, simulating as if they were captured by a 16-channel multispectral camera. After transformation, weighted subtractions were applied to extract blood and melanin absorption information from the reconstructed multispectral images of skins, realizing the spatial analysis of skin features. Meanwhile, we have demonstrated the advantages of smartphone-based multispectral system in terms of its inherent imaging resolution and the adaptability to various illumination sources. We have also presented that the proposed system can be used to monitor the skin hemodynamic activities in heart cycles and in a vascular occlusion. Compared with conventional multispectral imaging methods relied on lasers or tunable filters, our method improves dramatically the system compactness and immunity to motion artifacts. Compared with snapshot-multispectral-camera based systems, the smartphone-based system has higher imaging resolution, and is very cost-effective. Finally, differing from systems in labs and wards, our smartphone-based system is flexible enough to be used by users no matter when and where they are as long as there is a smartphone available. It should be reasonable to anticipate that our system and methods can be extremely useful in dermatology and cosmetology applications in future, especially in the inhabitant regions with low-resource settings.

Chapter 3. DEVELOPMENT OF SMARTPHONE-ENABLED MULTISPECTRAL AUTOFLUORESCENCE IMAGING METHOD FOR BACTERIA ASSESSMENTS IN SKIN AND ORAL CAVITY

3.1 BACKGROUND AND MOTIVATION

Many microbiomes like bacteria massively colonize on human tissue, sometimes even having larger population than human host cells[64]. Typical bacteria that reside in the skin, like cutibacterium acnes, are usually active in sebaceous glands[65]. The relevant metabolic activities of these bacteria trigger the risks of inflammation, leading to skin disorders, such as folliculitis and acne vulgaris[66]. Another common site of the bacteria reproduction is within the oral cavity, potentially causing dental plaque that may progress to tooth decay and further to periodontal diseases[67]. Therefore, bacteria assessments are clinically important for skin and oral health care.

In conventional bacterial assessments for skin and oral cavity, visual inspection is still being most widely used. Relying on the observation with naked eyes, this method is highly subjective. Even with experienced assessors, uncertainty often exists in the determination and evaluation of bacterial infection. To provide an objective and more accurate bacterial assessment, efforts have been paid to develop strategies to facilitate the visualization and diagnosis. For example, tape stripping and gram staining were used in the evaluation of bacterial infections within facial skin[68]. However, the entire procedure for sampling and staining is time-consuming, making such method difficult to provide real-time aids. As for the assessing the bacterial infection in the oral cavity, dental plaque is usually detected through the application of a disclosing gel or tablet. However, the use of external dye is

possible to cause harm to one's health[69]. Besides, the disclosing gel test is highly specialized for visualizing dental plaque, thus not applicable for detecting bacterial infections of all kinds and in other types of oral tissue. For these reasons, a new technology is in high demand that can provide real-time, non-invasive, and label-free assessment of bacteria in various human body parts.

Recent developments of fluorescence imaging have presented new interests and opportunities for assessing bacteria contents in the human tissue[70]. Porphyrins, for example, as a byproduct of bacterial reproduction and metabolism accumulating in sebaceous glands of skin and in dental plaque[71], fluoresce red light signals under black light stimulation, which can be contrasted from green autofluorescence background (originated from endogenous tissue components)[72]. By tracking porphyrins-induced red fluorescence signals, the bacteria-contaminated tissue can be effectively mapped. Accordingly, a numbers of fluorescence imaging devices have been developed for bacteria assessment in human tissue. For example, Seo et al have imaged bacteria within facial skin using a filtered Xe lamp as the light source and a spectrograph as the detector[73]. Veen et al have used a light-induced fluorescence imaging system to investigate the red fluorescence from dental biofilms[74]. A common limitation in these devices is the bulkiness of the setup as a result of the requirement of complicated wavelength filtering components, hindering their applications in routine and cost-effective examinations. In addition, due to the necessity to switch the wavelengths to realize the multispectral imaging, motion artifacts can often be introduced, which may contaminate the imaging quality. Some handheld devices have been recently developed to tackle this problem[75]. However, these developments can only provide RGB-mode snapshot photographs, lacking

advanced functions of spectral analysis that can enhance the detection accuracy from the complex autofluorescence tissue background. Furthermore, the color space of autofluorescence often varies due to the complicated makeup of the background tissue, which may introduce confounding factors in the assessment. These above-listed concerns in current autofluorescence imaging devices must be addressed before it can become practically useful for bacteria assessment in human tissues.

In this study, we propose a smartphone-enabled snapshot multispectral autofluorescence imaging system for mapping and analyzing bacterial infection in the facial skin and oral cavity. The system consists of an unmodified and intact commercial smartphone and a LED attachment, which provides the stimulation of fluorophores and acquires autofluorescence photographs in RGB mode. By using Wiener estimation method, the RGB autofluorescence photographs are converted into multispectral data cubes, providing an ability to spectrally analyze the fluorescence emissions due to bacteria-produced porphyrins and background tissue. In the reconstructed multispectral data cube, a weighted subtraction algorithm is proposed to extract bacteria-related fluorescence signals. Through the imaging and processing in facial skin and dental plaque, we show the usefulness of the proposed method in bacteria assessments within human body parts.

3.2 MATERIAL AND METHODS

3.2.1 SETUP AND CALIBRATION OF SMARTPHONE-ENABLED IMAGING SYSTEM

A schematic setup of smartphone-enabled autofluorescence multispectral imaging system is shown in Figure 1. The device consisted of a commercial smartphone and a home-made LED attachment (Figure 3.1(b, c)), where an iPhone 8 (Apple, USA) was used for

demonstration purpose though any type of smartphones can be used. The attachment was assembled with 10 black light LEDs (365 nm) on a 3D-printed annulus to provide light stimulation. The illumination uniformity in the field of view (FOV) was tested with a standard 95% reflection board. U1 (Minimum/Average lux) and U2 (Minimum /Maximum lux) were assessed as 0.92 and 0.78, respectively, meaning the illumination is relatively uniform. In the smartphone, we installed "Raw+" from the App Store and used it as a mobile application for photographing. When taking the photograph, the image resolution was set at 3024X4032 pixels. The shutter speed, ISO and white balance were set to be 1/60 seconds, 800 and 4000K, respectively.

The smartphone-based device was calibrated by a multispectral imaging system (Figure 3.1(a)). In this system, the target was stimulated by the same black light source. The stimulated fluorescence signals were relayed by a lens assembly to pass through a linear variable visible bandpass filter (400 nm to 700 nm, Edmund, USA). The filtered fluorescence signals were collected by a monochrome camera (A501K, Basler, Germany). By translating linear filter laterally as shown, the filtering wavelength of system can be adjusted. A spectrometer (CCS100, Thorlabs, USA) was used to label the working wavelengths at different translating positions. We selected 15 wavebands from 420 nm to 700 nm as our target for reconstruction (Figure 3.1(e)). To provide calibration training data set, we synthesized a fluorescence color chart by staining a resin base with black light fluorescent dyes which are used for body paint (Figure 3.1(d)). Through the mixing of various dyes, we obtained 40 color blocks with unique fluorescence appearance. During the calibration process, we illuminated this fluorescence color chart with the LED

attachment (Figure 3.1(b)). RGB-mode photographs and multispectral data cubes were acquired by the smartphone camera and linear-filter-based system, respectively.

To assess the performance of the proposed system and methods, we recruited two volunteers with combination and oily skin types, respectively. This study adhered to the tenets of the Declaration of Helsinki and was performed in accordance with the Health Insurance Portability and Accountability Act. Ethical approval was obtained from the Institutional Review Board of the University of Washington. All enrolled participants provided written informed consent. We conducted autofluorescence imaging to the facial skin and teeth of volunteers with the proposed smartphone-enabled device under black light illumination.

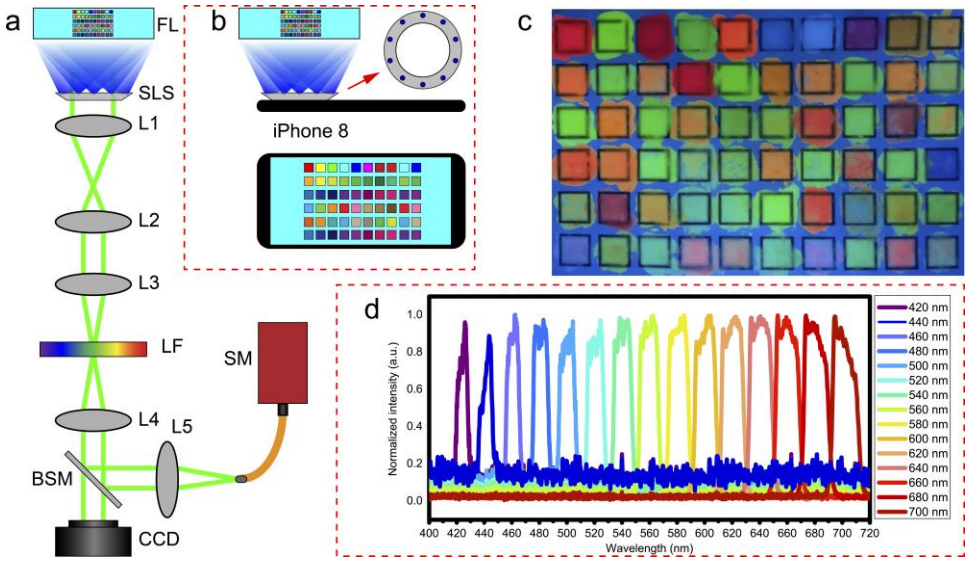

Figure 3. 1. Schematic for calibrating the smartphone-enabled multispectral fluorescence imaging system.
(a) Schematic of linear-filter-based multispectral imaging system for calibrating the smartphone-based device. FL: fluorescent color chart; SLS: short-wave light source, L1~4: lens; PH: pinhole; LF: linear variable visible bandpass filter. (b) Setup of smartphone-enabled autofluorescence imaging system. (c) Photographs of the front and back sides of real smartphone with attachment. (d) Home-made fluorescent color chart under black light

illumination. E. Wavelength-dependent sensitivity of selected 15 wavebands in multispectral imaging system.

3.2.3 SPECTRAL ANALYSIS AND EXTRACTION OF BACTERIA INFORMATION

On each RGB-mode autofluorescence photograph, we applied Wiener estimation reconstruction to transform it into multispectral data cube with 15 wavebands from 420 nm to 700 nm. From the data cube, we selected bacteria-contaminated tissue and endogenous tissue as the targets to compare their spectral appearance, thus realizing bacteria-targeted spectral analyses. According to their spectral performance of fluorescence, we applied weighted subtraction between different wavebands to extract and contrast porphyrins from the tissue beds.

3.3 RESULTS

3.3.1 CALIBRATION PROGRESS AND MULTISPECTRAL FLUORESCENCE RECONSTRUCTION ACCURACY

The estimated Winer estimation matrix affects whether multispectral information of autofluorescence can be accurately recovered from the RGB-mode autofluorescence photographs, thus directly determining the performance of subsequent spectral analysis and feature mapping. To investigate the reconstruction accuracy, we applied the estimated Wiener matrix back to the RGB-mode photograph of fluorescent color chart to reconstruct initial fluorescence spectra of 40 color blocks. Then, we calculated correlation coefficients and root mean square errors between initial and reconstructed fluorescence spectra of these color blocks. The results of which are given in Table 3. 1 and 3. 2. The maximum, minimum, mean values and standard deviation of correlation coefficients are 0.9970, 0.9125, 0.9663, and 0.0250, respectively. Lower correlation coefficients in some

fluorescent color blocks may be caused by relative weaker fluorescent signals. Due to the different quantum efficiencies, the sensors in smartphone cameras are more sensitive to green lights than others, which may cause higher reconstruction accuracy in corresponding wavebands. However, the different quantum efficiency between different smartphone cameras will not cause biased reconstruction results. For each color block, the root mean square error was averaged from the values of 15 wavebands. We selected three representative blocks, including the best, the worst and the one with the correlation coefficient close to the averaged value of all blocks, and showed their initial and reconstructed fluorescence spectra in Figure 3.2. These results demonstrate that our estimated Wiener matrix can faithfully recover multispectral information from the RGB-mode autofluorescence photographs with good accuracy.

Table 3. 1. Correlation coefficients between initial and reconstructed fluorescence spectra of 40 color blocks.

0.9265	0.9369	0.9400	0.9330	0.9690	0.9867	0.9792	0.9794	0.9380	0.9862
0.9696	0.9326	0.9827	0.9247	0.9761	0.9774	0.9549	0.9663	0.9666	0.9804
0.9125	0.9225	0.9706	0.9864	0.9417	0.9841	0.9518	0.9559	0.9788	0.9236
0.9316	0.9884	0.9318	0.9883	0.9494	0.9929	0.9970	0.9940	0.9940	0.9351

Table 3. 2. Root mean square errors between initial and reconstructed fluorescence spectra of 40 color blocks.

2.7041	1.7878	3.8703	2.2134	2.6815	1.4285	2.0663	2.9904	2.1563	0.6363
1.4417	2.5464	1.4353	1.7301	1.6579	0.7343	2.7354	1.6797	2.8988	2.1948
2.6527	1.6286	1.8531	0.6651	2.1558	1.3972	4.0032	3.4471	3.4509	2.2908
2.6320	1.2138	1.4000	0.9280	1.7134	1.6525	1.1765	1.3619	1.0376	1.1561

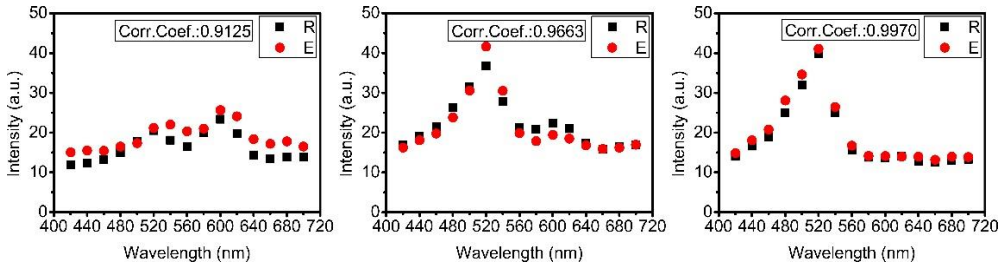

Figure 3. 2. Comparison of initial and reconstructed fluorescence spectra in 15 wavebands from 3-representative fluorescent color blocks.
The correlation coefficients in left, middle and right are 0.9125 (the worst), 0.9663 (close to the mean value) and 0.9970 (the best), respectively. R: initial fluorescent spectra; E: reconstructed fluorescence spectra.

3.3.2 AUTOFLUORESCENCE IMAGING OF SKIN AND ORAL CAVITY WITH SMARTPHONE-BASED DEVICE

In this part, we show the autofluorescence imaging results from volunteer 1. Figure 3.3(a) shows the RGB-mode autofluorescence photograph from the right-side skin of nose bridge, where it is evident that the skin tissue around the hair follicles fluoresce red signals. From the partial zoom-in image in Figure 3.3(b), the fluorescence at different spots is seen to vary in color and strength. Similar skin autofluorescence appearance can be observed in photographs of the nose alar (Figure 3.3(c)) and its zoom-in details (Figure 3.3(d)). The different autofluorescence performance around hair follicles are believed to be caused by multiple factors, including the amount of sebum secretion and bacteria activeness. In general, excessive sebum secretion in sebaceous glands and high bacterial contamination work together to produce strong red fluorescence signals [30]. Figure 3.3(e) shows the autofluorescence photograph of the teeth in the subject's oral cavity, where the significant red fluorescence signal at the root part of the lateral incisor is a strong indication of the existence of dental plaque, a mass of bacteria. From the zoomed-in detail of the lateral incisors (Figure 3.3(f)), the intensity of red fluorescence is seen not evenly distributed in

the dental plaque region. The boundary is fuzzy due to the presence of autofluorescence signals by the endogenous teeth tissue. While the fluorescence photographs clearly indicate the porphyrin-containing bacteria accumulation in the host tissue, the extraction and quantitative assessment of the bacteria content is difficult largely due to the strong background fluorescence signals emitted by the host tissue components, e.g. protein collagens, enamel, dentin etc. in this case.

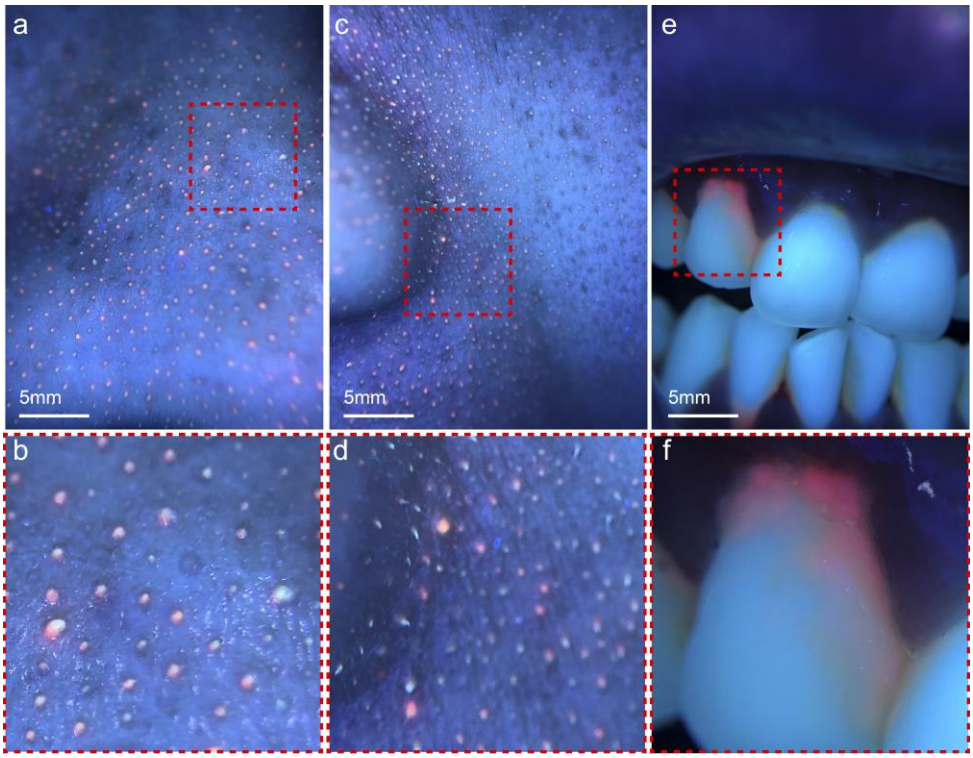

Figure 3. 3. RGB-mode autofluorescence photographs of facial skin and oral cavity acquired from volunteer 1 by smartphone-based device, indicating the bacteria accumulation on the host tissue.
(a) Photographs of right side of nose bridge. (b) Zoom-in view of the red box area of (a). (c) Photographs of lest side of nose alar. (d) Zoom-in view of the red box area of (c). (e) Photographs of teeth. (f) Zoom-in view of the red box area of (e).

3.3.3 MULTISPECTRAL RECONSTRUCTION OF AUTOFLUORESCENCE PHOTOGRAPHS OF SKIN AND ORAL CAVITY

As described above, the RGB-mode autofluorescence photographs of facial skin and teeth (Figure 3.3) were converted into multispectral data cubes (Figure 3.4) using the estimated Wiener matrix. As shown in Figure 3.4(a) and Figure 3.4(b), background skin tissue at the nose bridge and alar emits strong fluorescence in blue and green wavebands (from 440 nm to 520 nm), consistent with autofluorescence measurements reported by Croce and Bottiroli [31]. The fluorescence peaks in blue-green wavebands are believed to be contributed by multiple fluorophores including proteins, NADH, vitamins and fatty acids. The spot areas around hair follicles fluoresce red light, especially from 600 nm to 660 nm, matching well with prior fluorescence measurements of porphyrins [32]. Figure 3.4(c) shows reconstructed multispectral data cube of autofluorescence from the teeth (Figure 3.3(e)), where strong fluorescence exists from 420 nm to 600 nm. It appears that the fluorescence at this band peaks at around 500 nm and 520 nm, which are typical fluorescence peaks of dentin and enamel [33]. The dental plaque on the surface of lateral incisor shows similar responses to that of hair follicle regions in Figure 3.4(a) and (b), fluorescing intense signals from 600 nm to 660 nm. The reconstructed multispectral data cube verified the different spectral performance of bacteria-produced porphyrins and background tissue, indicating that this multispectral information can be utilized to distinguish them by conducting spectra-based analyses and processing.

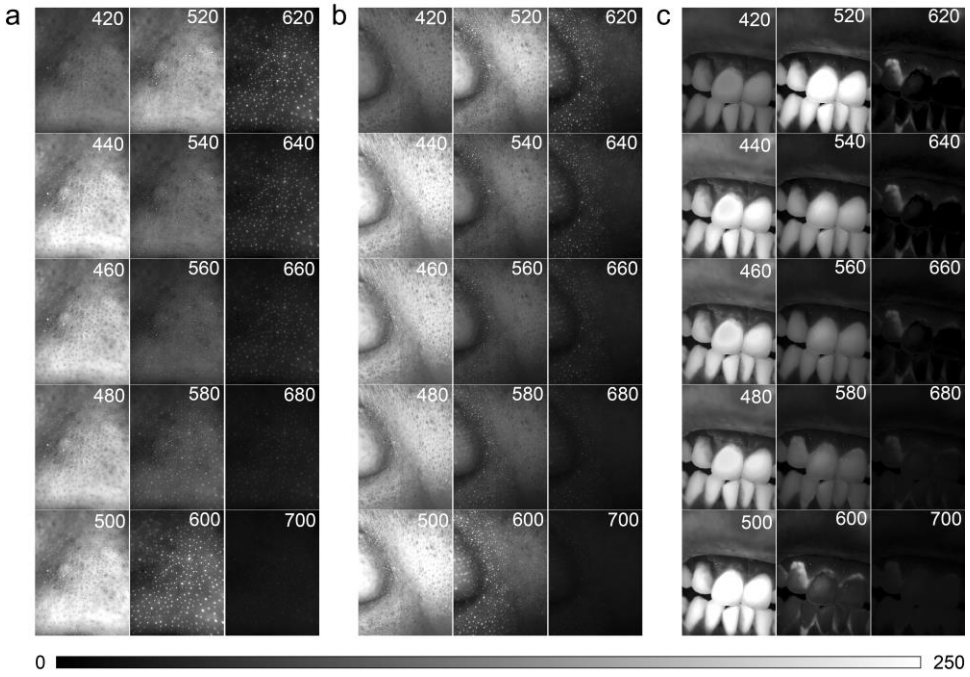

Figure 3. 4. Reconstructed multispectral autofluorescence data cube at the wavelength bands as shown from the RGB-mode photographs.
(a) Multispectral data cube of right side of nose bridge. (b) Multispectral data cube of lest side of nose alar. (c) Multispectral data cube of teeth. The reconstructed spectra range from 420 nm to 700 nm, the labeled number on each image indicates the corresponding waveband. The color bar indicates the signal strength at a full scale of 8-bits.

3.3.4 SPECTRAL ANALYSIS AND BACTERIA-TARGETED FEATURE MAPPING

To compare the fluorescence spectral performance between bacteria-contaminated tissue and background skin on the side of nose bridge, we selected 10 data points with red fluorescence signals and other 10 background data points in the fluorescence photograph (Figure 3.5), where the fluorescence spectra were extracted from the reconstructed multispectral data cubes using the proposed method. The positions of these data points are labeled with red and blue arrows, respectively, as shown in Figure 3.5(a). Figure 3.5(b) shows that the two groups of data points behave similarly in fluorescence spectra from 420 nm to 540 nm. However, from 560 nm to 700 nm, the fluorescence signal strength in the

bacteria group is obviously higher than the background skin group. The intensity difference reaches a maximum around 600 nm and 620 nm. According to the weighted subtraction method as introduced above, we selected 600 nm (Figure 3.5(c1)) and 560 nm (Figure 3.5(c2)) as two wavebands to conduct dual-waveband processing to realize the feature mapping of bacteria-produced porphyrins. From the spectral analysis result, the subtraction ratio was calculated to be 1.22, which was applied in the subtraction strategy. The result is shown in Figure 3.5(c3), which is porphyrin-feature mapping, showing minimal background signal contamination. Figure 3.5(d) to (f) show the similar spectral analyses and feature mapping of the porphyrin content within the skin located at the left side of nose alar.

Figure 3.5(g) is the photograph of the fluorescence image captured from teeth, where the background greenish fluorescence produced by tooth tissue components (e.g. enamel, dentin etc.) is seen to dominate. To separate the fluorescence due to porphyrin-containing plaque from the strong background fluorescence, we again selected 10 data points on the clean surface of lateral incisor to be the background group and 10 points from the plaque locations. For this case, the weighted subtraction ratio was calculated to be 0.58. After the subtraction strategy was applied, the fluorescence signals of teeth were removed, resulting in the dental plaque area clearly outlined (Figure 3.5(i)). To make a clearer illustration for the porphyrin-mapping performance, we conducted a quantitative analysis to the bacteria-produced porphyrins and background signals. In doing so, we first selected twenty corresponding positions from each image of the RGB photograph, reconstructed multispectral data at 560 nm and 600 nm and porphyrin-feature mapping. The signal strengths due to either bacteria-produced porphyrins or background tissue at these locations

were evaluated and averaged. The results are presented in a bar plot format (Figure 3.5(j)), where the strong background signals exist in both RGB and multispectral images. However, the background signals are significantly suppressed in feature-mapping result (i.e. porphyrin feature mapping shown in the images marked by '3' at the right column of Figure 3.5). To quantify the contrast enhancements, the ratios between porphyrins and background signals in all groups of data were calculated and shown in Figure 3.5(j), where the signals due to the background skin and teeth were seen greatly reduced when using the proposed subtraction strategy, with a contrast enhancement between 5 and 15 times compared with either raw fluorescence image or multiple spectral images. Therefore, the use of the signals after applying the subtraction strategy would be more accurate in the quantitative measurement of porphyrin contents to indicate the severity of bacterial infections. It should be noted that the background of dental plaque imaging came from teeth, different from facial skin. Thus, the weighted subtraction was conducted between porphyrins and teeth fluorescence, resulting in Figure 3.5(i3) where the background teeth signals are basically removed with some background signal residues in gingiva and lips areas. While it is beyond the scope of this study, the elimination of multiple background signals with different emission spectrum, like teeth and gingiva, can be realized by expanding our dual-waveband weighted subtraction to a multi-waveband model.

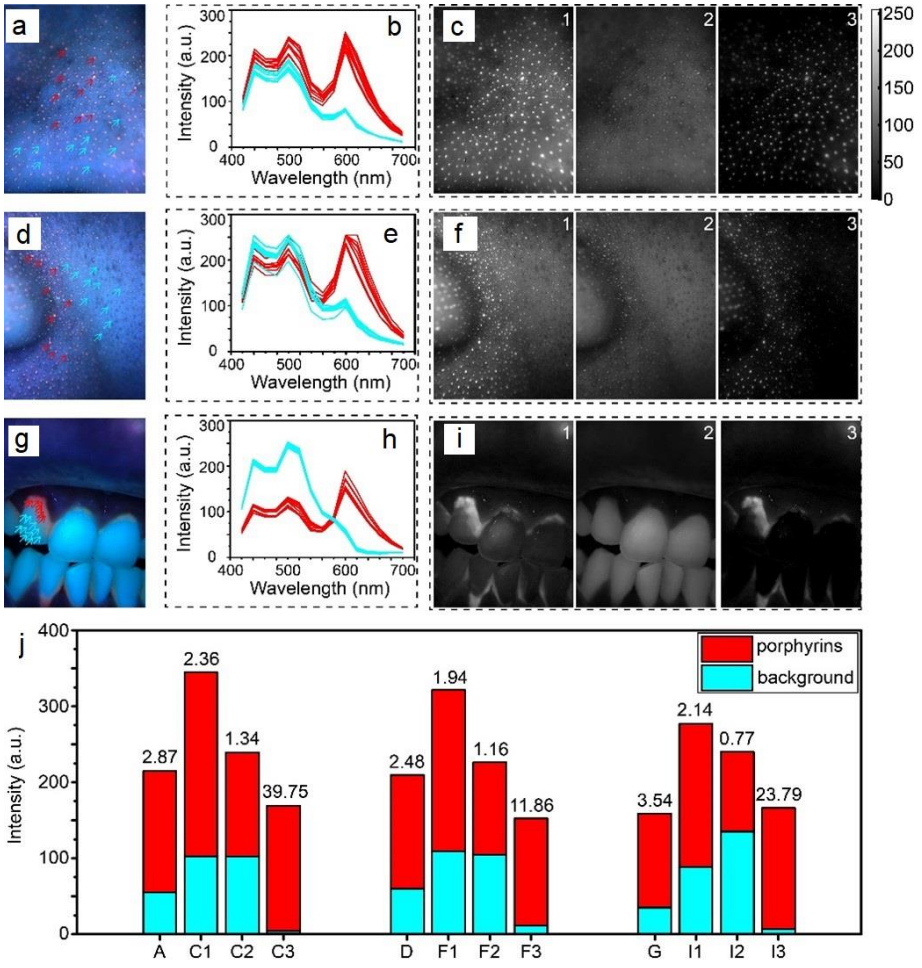

Figure 3. 5. Mapping and Quantification of porphyrins fluorescence.
(a, d, g) Positions of the selected 10 data points of porphyrin and background tissue groups illustrated respectively on the fluorescence photographs. Red arrow: bacteria-related points; blue arrow: background. (b, e, h) Corresponding spectral analysis of two groups of points selected from (a), (d) and (g). Red line: bacteria-related points; blue line: background. (c, f, i) Weighted subtraction processing for bacteria-targeted feature mapping, where 1): image from 600 nm waveband; 2): image from 560 nm waveband; and 3): bacteria-targeted feature mapping with background signal contamination removed. (j) Quantitative analysis of bacteria-produced porphyrins and background autofluorescence. The intensity from each group is averaged from 20 selected data points. Labeled numbers on bars are the intensity ratios between porphyrins and background signals. The letters and numbers on the horizontal axis refer to the quantification from specific figures (e.g. C1 points to Figure 3.5(c1)).

3.3.5 BACTERIA ASSESSMENTS OF COMBINATION AND OILY SKINS

In common senses, compared with the combination type of skins, oily skin is of more active sebum secretion in order to subsidize higher bacteria accumulation in sebaceous glands. It is acknowledged that for the combination skin type, cheek areas usually show lower bacterial infection than the nose areas do, whereas for the oily skin, the bacterial infection is believed to be equally active in both the areas. With our smartphone-enabled system and processing methods, we imaged the nose and cheek areas of the two volunteers and conducted bacteria assessments of the two distinct skin types. Figure 3.6(a) and (d) show the direct facial RGB photographs of combination and oily skins, respectively. From the facial skin, we selected the nose and cheek areas as the imaging targets of interest, showing by the red dot boxes. The autofluorescence photographs of corresponding areas are shown in Figure 3.6(b) and (e), from where red fluorescence spots in both the nose and cheek areas of oily skin appear denser and brighter than those of the combination skin type. As somewhat expected, only a very small amount of red fluorescence spots can be found in the cheek area of the combination skin (Figure 3.6(b2)), whereas these specific features are densely distributed in the cheek area of oily skin (Figure 3.6(e2)). After multispectral reconstruction and feature extraction, we obtained bacteria-targeted feature mapping from autofluorescence photographs, showing in Figure 3.6(c) and (f). As discussed above, the extracted signal strengths can be used as a direct indication of the extent of porphyrin accumulations, thus could be used for evaluating the bacterial infection conditions of the skin. The mapping results here have confirmed the usefulness of our proposed method, for that the signal strengths support our common sense about the oily skin being infected more severe by bacteria, especially in the cheek area. Based on the mapping results, we

conducted further quantitative assessments to statistically compare the differences. Figure 3.6(g) shows the amount of features (bright spots) counted from each sampling area. Figure 3.6(h) shows the average signal strengths of porphyrins fluorescence in these areas. From the quantitative results, it is concluded that sebaceous glands in the nose area are widely infected by bacteria in both the skin types, with the bacterial metabolism more active in the oily skin. Further, sebaceous glands in cheek area of the combination skin are almost free from obvious bacterial infection, while those in the oily skin are pervasively and heavily infected. These comparison and quantification demonstrate the ability of the proposed system and method to evaluate the bacterial infections of different skin samples.

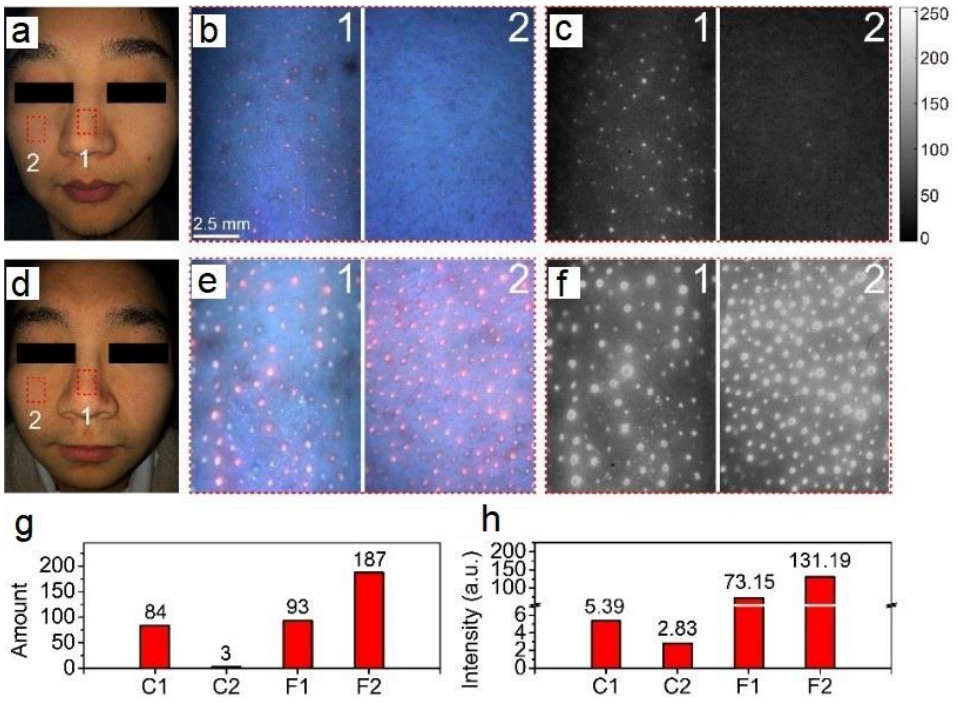

Figure 3. 6. Bacterial assessments of combination and oily skin types.
(a, d) Straight facial RGB photograph of a volunteer with combined and oily skin type, respectively. Red dot box areas marked with "1" and "2" indicate the targeted fluorescence imaging areas at the nose and cheek regions, respectively. (b, e) Smartphone-enabled autofluorescence photographs of the targeted areas in (a) and (d), respectively. (c, f) Bacteria-targeted feature mapping calculated from (b) and (e). (g) Amounts of bacteria-produced porphyrins features in targeted nose and cheek areas of the combined and

oily skin types. (h) Average fluorescence intensities of the targeted nose and cheek areas of combined and oily skin types. The letters and numbers on horizontal axis of (g) and (h) point to the specific figures (e.g. C1 points to nose area in Figure 3.6(c1)).

3.4 DISCUSSION AND CONCLUSION

Skin and oral care have experienced a booming development in the past decade. The global market size for the skin and oral care products was valued at around 180 billion U.S. dollars in 2019 and is expected to reach 240 billion U.S. dollars in the next five years. Following this broad market figures, the development of skin and oral assessment tools that are capable of identifying and creating personalized products, are surging in demand at the same time. Bacterial infection is one of the most important factors to cause conditions in the skin and oral cavity. Recently, camera-based imaging has shown its attractiveness and potential in providing real-time and visualized assessment of the bacterial infection. In this study, we initiated a smartphone-enabled imaging system to realize mobile multispectral autofluorescence photography. With this cost-effective, compact and flexible imaging device, camera-based bacterial assessments can be made available in people's daily lives rather than in research labs and clinical wards, which presents potential in both spreading this technique and improving public health care.

There are a number of multispectral imaging systems that have been developed for smartphone use. However, most of them rely on the additional hardware, e.g., optical filters or monochromatic light sources to realize the multispectral imaging. For example, Hwang et. al used an auxiliary miniaturized filter-wheel-based multispectral system on the smartphone to select spectral illumination from housed white LED [35]. Liang et. al assembled LEDs of various wavelengths from 400 nm to 1000 nm on a PCB board to achieve polarized multispectral imaging [36]. In these systems, the selection of required

illumination wavelengths requires time to complete, introducing motion artifacts in multispectral data cubes. In comparison, our method requires no extra attachments for realizing multispectral imaging. In addition, there is no motion artifact contamination in our system and method since the multiple spectral imaging is realized from a single snapshot photograph, which improves the accuracy of final results and also supports the compactness of system.

In this study, we have conducted the analyses of porphyrins fluorescence as a proof of concept to introduce our system and method, in which the porphyrin content was contrasted with the dual-waveband subtraction method after multispectral reconstructions. Moreover, our method can also be developed to meet the purpose of contrasting fluorophores from background with higher crosstalk. Weighted subtraction method can be expanded to a multiple waveband model if signals from multiple fluorophores are close to each other. Therefore, our system and method can be used in the applications involving more complicated skin components, such as in clinical wound care. An example of such can be the differentiation of bioburden in the wound bed that fluoresce highly mixed signals. Except for metabolic porphyrins, pyoverdines also exists as bacterial byproducts in bioburden and fluoresce cyan under black light illumination which can easily be overwhelmed by endogenous green fluorescence. With our method, these fluorophores can be potentially separated and mapped from the wound bed, thus providing visual guidance for wound healing prediction and debridement. Besides, although we are applying our system and method to analyze bacterial infections of human tissue in this study, the proposed strategy can be generalized in other applications which require fluorescence differentiation and quantification. For example, as we mentioned above, the endogenous

fluorescence of skin is contributed by multiple fluorophores including collagen proteins. By adjusting reconstructed wavelengths, our smartphone-enabled device and method can also be applied in investigations of the collagen, useful to evaluate aging performance of skin.

There are some limitations in our current study to use smartphone-enabled system in bacteria-targeted imaging and assessments. At the current stage, we are imaging facial skin and dental plaque from only two volunteers as a proof of concept. More subjects are clearly needed in order to further improve and validate the performance of our system and method with a sufficient statistical power, paving the way towards practical and sophisticated applications (including clinical). Besides, currently, smartphone cameras with different sensors need to be calibrated independently because of their unique performance in the RGB space. Except for the efficiency reduction caused by the tedious calibration step, the lack of standard fluorescent color checker would also lead to uncertainties in reconstruction performance. These factors may limit the generalization of proposed system and method. In the future, we will develop universal and simplified calibration methods, including building a standard fluorescence color checker and RGB-mode transformation algorithms, to support our strategy to be applicable on different smartphone operating platforms. Furthermore, at present, the multispectral reconstruction, spectral analysis, feature mapping and quantitative analysis are still achieved by off-line processing, thus the usability and efficiency of this smartphone-enabled system have not been fully exploited. By utilizing the strong communicating and computing power of current commercial smartphones, we will further build mobile applications and apply cloud computing to

realize real-time and online processing of data, which would be extremely helpful to develop mobile health and could-based data managements on our imaging platform.

We have proposed a smartphone-enabled autofluorescence imaging system for bacteria assessment within human tissue. Based on this system, we developed corresponding multispectral reconstruction and weighted subtraction methods to realize spectral analysis and feature mapping of bacteria-targeted features in skin and oral cavity. With the Wiener estimation strategy, the acquired RGB-mode autofluorescence images were converted into multispectral data cubes across the visible range, from which the specific spectral emissions of bacteria-produced porphyrins can be isolated. We further described a weighted subtraction strategy to suppress the background signals in order to enhance the contrasts of targeted bacteria features against the background tissue beds. As a proof of concept demonstration, we presented the RGB photographs, reconstructed multispectral images, spectral responses and bacteria-targeted mapping results of facial skin and teeth. Based on the feature mapping results, we also conducted quantitative assessments to investigate different bacterial infection conditions of the combination and oily skin types. Compared with conventional multispectral imaging systems, our smartphone-enabled system and method perform similar spectral analysis ability but work in a snapshot mode, immune to any motion artifacts. Being easily accessible and very cost effective, it is expected that the proposed mobile multispectral smartphone system can be utilized by consumers in their daily live, which would be especially beneficial for people living in the rural and low-resource setting environment.

Chapter 4. DEVELOPMENT OF SMARTPHONE-ENABLED REMOTE MULTISPECTRAL PHOTOPLETHYSMOGRAPHY METHOD FOR SPATIOTEMPORAL MONITORING OF BLOOD OXYGENATION AND PULSATION ON HUMAN SKIN

4.1 BACKGROUND AND MOTIVATION

The primary function of the microcirculation is to supply oxygen and nutrients to the local tissue[76][76][91][91]. Microcirculation status, hence capillary hemodynamics, plays an important role in regulating blood flow and tissue oxygenation, thus being well recognized in the vital sign monitoring, as well as in the study of vascular function, peripheral artery diseases [77-81][77-81][92-96] and cardiovascular disorders[82, 83][82, 83][97, 98]. Therefore, non-invasive and contactless techniques to assess microcirculatory behaviors and hemodynamic contents are indispensable for clinical practices and daily assessment of medical conditions [84, 85][84, 85][99, 100].

Skin, being the largest and capillary-rich organ, provides an easily accessible window for developing such techniques to access the hemodynamic information inside the human body [86-89][86-89][101-104]. Thanks to the translucent property of skin at visible and near infrared (NIR) wavelengths, numerous optical methods have been developed to derive signals that are indicative of blood hemodynamics, for example blood perfusion, oxygen saturation, pulsation etc. [44, 90-93][44, 90-93][44, 105-108]. Among these optical methods, photoplethysmography (PPG) is becoming one of the most popular techniques and being widely used for in-hospital monitoring and even in wearable devices nowadays [94-96][94-96][109-111][109-111]. Due to the strong absorption of blood to the light, PPG

works by recording time-elapsed optical reflectance modulated by the effective blood volume within light interrogated tissue volume to indicate the dynamic pulsatile behavior of the blood flow (volume) caused by cardiac heartbeat. With this dynamic and pulsatile blood flow behavior directly obtained from the human skin tissue, PPG can be used to monitor the heart rate [97][97][112], cardiac cycle [98][98][113] and respiration [99][99][114]. However, PPG is often implemented through a contact approach between sensors and skin, prone to motion artifacts. To solve this problem, remote PPG (rPPG) has been proposed and developed [42, 100][42, 100][42, 115]. rPPG is typically implemented by a camera-based system that is used to acquire the video of skin surface, from which to derive the pulse waveforms [101][101][116]. Using dedicated signal processing algorithms, subtle momentary changes in the skin reflection in the video can be extracted. The remote attribute of rPPG is its most attractive advantage compared to the conventional PPG [100][100][115]. However, since global parameters are addressed in the above applications, there is still a demand to develop techniques that can be used to perform the spatiotemporal analysis of rPPG and explore its potential applications.

As exciting as the rPPG delivers, however, previous developments were not able to decouple the hemoglobin compositions from the acquired signals, e.g., oxygenated (HbO2) and deoxygenated (Hb) blood. This additional information is critical for our improved understanding of the microcirculatory function and hemodynamic regulations [102][102][117]. In most cases, changes in pulsation and oxygenation detected at the peripheral site would manifest changes in supplying arteries or systemic blood flow [86, 103, 104][86, 103, 104][101, 118, 119]. Although previous rPPG studies have explored the changes in pulse waveforms (e.g., shape, intensity) upon conditioning the blood flow, they

have not been able to decouple the modulation of deoxyhemoglobinO2 and deoxyhemoglobin from the tissue volume, making the techniques less effective and accurate in assessing blood flow obstruction and microvascular disorders. In addition, achieving all these detections with the use of a widely available and cost-effective device is an additional challenge that, to our best knowledge, has not been addressed. In our previous study, we have developed smartphone-enabled transdermal optical imaging techniques to investigate the spatial blood perfusion on the human skin [105][105][72]. This work has shown that snapshot RGB-mode photographs of the skin can be reconstructed into multispectral images to map the contents of bio-chromophores [106][106][120], which proves it possible to integrate the smartphone-enabled transdermal optical imaging technique with rPPG to measure and monitor the cutaneous hemodynamics in both time and spatial scales.

Herein, we propose a smartphone-enabled remote multispectral photoplethysmography (SP-rmPPG) system and method to provide a spatiotemporal monitoring of the perfusion changes and pulsations of oxyhemoglobin and deoxyhemoglobin in the human skin. The method first converts the RGB video into the multispectral data cube, upon which to derive and decouple spatiotemporal oxyhemoglobin and deoxyhemoglobin information within the effective blood volume utilizing a modified Beer-Lambert law and dual-waveband processing method. We then describe a method to obtain the spatiotemporal pulsation amplitudes of both two types of oxygenated and deoxygenated bloods by applying a window-based lock-in amplification approach. To demonstrate the feasibility and performance of our proposed method, two experiments are performed by imaging two peripheral skin sites in health volunteers while conditioning the upstream blood supply and

drainage, with an aim to delineate the changes in oxyhemoglobin and deoxyhemoglobin modulation and pulsation strength upon the challenging.

4.2 MATERIAL AND METHODS

4.2.1 SET UP OF SYSTEM AND DATA RECORDING

Schematic of the experimental setup to demonstrate the proposed SP-rmPPG method is illustrated in Figure 4.1(a), where an unmodified smartphone was used to acquire video images of dynamic light reflectance emerging at the skin surface upon which to derive blood oxygenation and hemodynamics. In this study, an iPhone 8 (Apple, USA) was used for the demonstration purpose, but any types of smartphones can be used. The videos were collected by the smartphone rear camera under illumination from the built-in flashlight. The spectral power distribution of the flashlight is shown in Figure 4.1(b). The relative spectral sensitivities of the R, G and B channels in the smartphone camera are given in Figure 4.1(c). We placed a polarizer film in front of the flashlight and an analyzer film in front of the camera lens. The film pairs were arranged orthogonally to minimize specular reflections from the skin surface. The illumination uniformity in the field of view (FOV) was tested with a standard 95% reflection board. U1 (Minimum/Average lux) and U2 (Minimum /Maximum lux) were assessed to be 0.99 and 0.92, respectively, indicating that the illumination is relatively uniform across the sample target.

The room temperature was kept at around 23℃ and the humidity was around 50% during the experiments of video recording. Before recording the video, the volunteer was allowed to calmly sit in a chair for 5 minutes to get acquainted to the room environment and stabilize the heartbeat. The smartphone was placed 30 cm away from the skin surface. In the smartphone, we installed “ProMovie” from the App Store and used it to acquire videos, representing the light reflectance emerging at the skin surface. The image resolution was set at 2160x3840 pixels. The shutter speed, ISO and white balance were set to be 1/60 seconds (i.e. frame rate of 60 fps), 100 and 4000K, respectively. Before data processing described below, a proprietary sub-pixel registration algorithm was used to pre-process the videos to minimize subtle motion artifacts in the results.

Normal healthy volunteers were enrolled in this study to demonstrate the feasibility of proposed methods. This study adhered to the tenets of the Declaration of Helsinki and was performed in accordance with the Health Insurance Portability and Accountability Act. Informed consent was obtained from the subjects prior to the start of each study session. Ethical approval was obtained from the Institutional Review Board of the University of Washington.

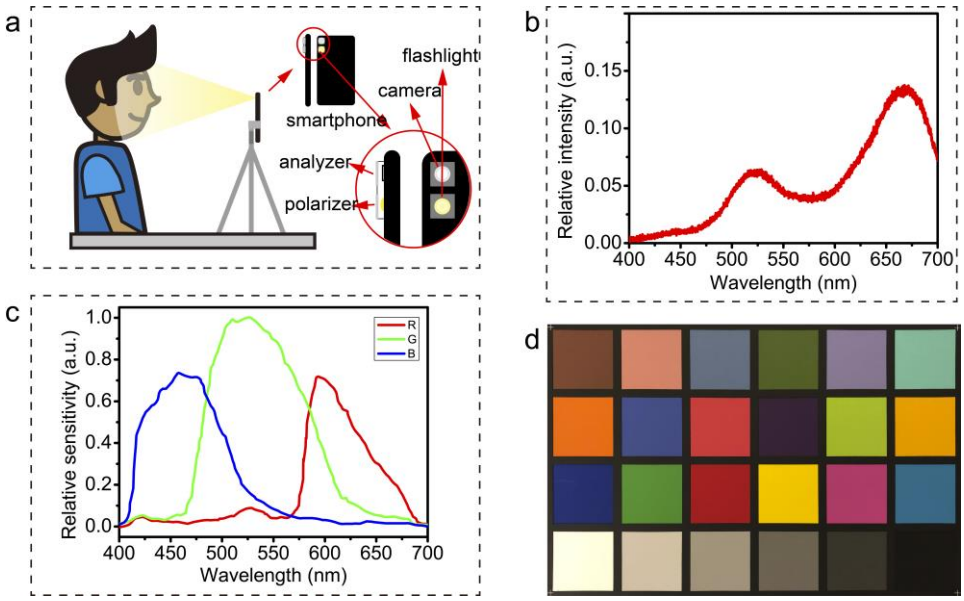

Figure 4. 1. Schematic of the smartphone multispectral remote photoplethysmography.
(a) Schematic of the smartphone remote PPG (SP-rmPPG) system setup for video recording of the subject. (b) Spectral power distribution of the built-in flashlight in the smartphone (iPhone 8, Apple Inc, USA). (c) Spectral sensitivity of R, G and B channels of the smartphone camera used to record videos. (d) Photograph of the standard color checker used to calibrate the smartphone for multispectral imaging.

4.2.2 SMARTPHONE CAMERA CALIBRATION TO PERFORM MULTI-SPECTRAL IMAGING

We applied Wiener estimation method to calibrate the built-in RGB-mode camera in the smartphone to perform multi-spectral imaging. The details of this method can be found in our previous study [105, 107][105, 107][72, 121]. Briefly, a standard color checker (X-Rite ColorChecker Classic, Figure 4.1(a)) was used in this study to calibrate the smartphone

camera, where the images (or video) captured from the standard color checker were used as the training data set to determine a transformation matrix that is needed to convert the RGB color images into the multi-spectral images. The standard reflectance data of the color checker was provided by the manufacturer. Here, we selected 450, 500, 550, 600, 650 and 700 nm as the wavelengths of interest in the calibration, though other wavelengths can be selected if needed. VV^t is the autocorrelation matrix of the RGB sensor responses in the camera.

To verify the accuracy, the derived transformation matrix was firstly applied on the RGB-mode image of the color checker that was used for calibration to calculate its reconstructed reflectance data at multiple wavelengths of interest. We evaluated the goodness of fit coefficients (GFC) between the standard and reconstructed reflectance data [108, 109][108, 109][122, 123]. The minimum, average and maximum GFC values were measured to be 0.9533, 0.9898 and 0.9999, indicating excellent performance of the derived transformation matrix. We then tested the matrix on a set of 14 unique skin tone colors in ColorChecker Digital SG (X-Rite) that were not used for the calibration. The comparison of standard and reconstructed reflectance data is shown in Figure 4.2, with corresponding GFC values shown. The minimum, average and maximum GFC values were measured to be 0.9928, 0.9971 and 0.9999, demonstrating that the derived transformation matrix is accurate enough to estimate the real reflectance of the targets from their RGB-mode images.

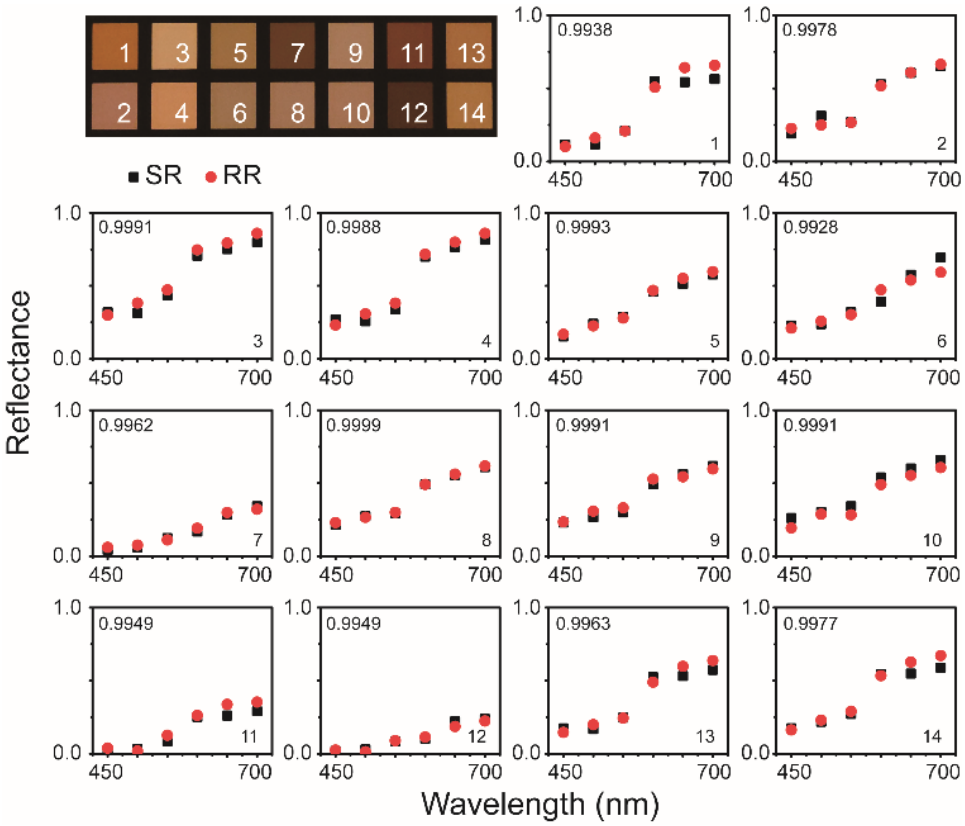

Figure 4. 2. The comparison between the standard reflectance and the reconstructed reflectance from the transformation matrix for each block of 14 unique skin tone colors in ColorChecker Digital SG.
(SR: standard reflectance; RR: reconstructed reflectance). Numeric values shown in each block are the goodness of fit coefficients between SR and RR.

4.2.3 ANALYSIS OF CHANGES IN OXYHEMOGLOBIN AND DEOXYHEMOGLOBIN WITHIN BLOOD PERFUSION

With the transformation matrix *W* obtained in the last Section 2.2, the RGB-mode videos of the skin can then be converted into multispectral data cubes. The multispectral cube thus obtained represents the spectral information at the six wavelengths of 450, 500, 550, 600, 650 and 700 nm, which can be written as:

$$\begin{bmatrix} M_1(x,y,t) \\ M_2(x,y,t) \\ \dots \\ M_6(x,y,t) \end{bmatrix} = W \times \begin{bmatrix} R(x,y,t) \\ G(x,y,t) \\ B(x,y,t) \end{bmatrix} \tag{4.1}$$

where $M_i(x,y,t)$ is the reconstructed spectral value at pixel (x,y) and time t. i is the channel number ($i = 1,2,\dots,6$, representing 450, 500, 550, 600, 650 and 700 nm, respectively). $R(x,y,t)$, $G(x,y,t)$ and $B(x,y,t)$ are the values at the pixel (x,y) and time t of the video from the red, green, and blue channels, respectively.

Since here we are interested in extracting oxyhemoglobin and deoxyhemoglobin information in the dynamic blood perfusion, the wavelength selection could follow the requirements of pulse oximetry [110][110][124]. That is, the absorption coefficients of oxyhemoglobin and deoxyhemoglobin should be approximately equal at one wavelength and differ considerably at another wavelength. Therefore, we selected the channel 2 (500 nm, approximately at the isosbestic point) and channel 5 (650 nm, having considerable difference in absorption between oxyhemoglobin and deoxyhemoglobin) as the target wavelengths in further processing steps to derive oxygenation information. For the reconstructed signals at each channel, we estimated the changes in light absorption with reference to the time zero by using the modified Beer-Lambert law [111][111][125], i.e.,

$$\Delta A = A_t - A_0 = -\log\left({}^{I_t}/_{I_s}\right) - \left(-\log\left({}^{I_0}/_{I_s}\right)\right) = -\log\left({}^{I_t}/_{I_0}\right) \tag{4.2}$$

where ΔA is the change in light absorption from the time t_0 to t. A_t and A_0 are the light absorbance at the time t and t_0. I_t and I_0 are the signal intensities in selected channels at the time t and t_0. I_s is the intensity of incident light. Assume that the light absorption in the skin is caused by melanin, oxyhemoglobin and deoxyhemoglobin chromophores. In the

current study, we can safely assume the melanin concentration and skin tissue scattering are relatively constant over time [40]. Thus, the change in light absorption (Eq. 3) would be dominated by the changes in oxyhemoglobin and deoxyhemoglobin concentrations within the blood volume. Consequently, Eq.5.2 could be rewritten as,

$$\Delta A = \Delta c^{HbO2} \varepsilon^{HbO2} l + \Delta c^{Hb} \varepsilon^{Hb} l \tag{4.3}$$

where Δc is the change in either oxyhemoglobin or deoxyhemoglobin concentrations. ε is the absorption extinction coefficient of either oxyhemoglobin or deoxyhemoglobin. l is the light interaction path length. We assume that the light interaction path lengths at different wavelengths to be the same. In order to decouple the changes in oxyhemoglobin and deoxyhemoglobin in Eq.5.3, we constructed a weighting formula below,

$$\Delta = \Delta A_2 - k\Delta A_5 = \Delta c^{HbO2} l\left(\varepsilon_2^{HbO2} - k\varepsilon_5^{HbO2}\right) + \Delta c^{Hb} l\left(\varepsilon_2^{Hb} - k\varepsilon_5^{Hb}\right) \tag{4.4}$$

where Δ is the result after weighted subtraction. ΔA_2 and ΔA_5 are the changes in the light absorbance at 500 nm and 650 nm, respectively. k is the subtraction weighting factor to be determined. ε_2^{HbO2}, ε_5^{HbO2}, ε_2^{Hb} and ε_5^{Hb} are the absorption extinction coefficients of oxyhemoglobin and deoxyhemoglobin at 500 nm and 650 nm, respectively. It is clear that if the factor k is set to be $\varepsilon_2^{Hb} / \varepsilon_5^{Hb}$, then the effect of the deoxyhemoglobin changes on Eq.5.4 would be eliminated. Thus, the change in oxyhemoglobin concentration can be derived as,

$$\Delta c^{HbO2} = \frac{\Delta A_2 - k\Delta A_5}{l\left(\varepsilon_2^{HbO2} - k\varepsilon_5^{HbO2}\right)} \quad (\text{where } k = \varepsilon_2^{Hb} / \varepsilon_5^{Hb}) \tag{4.5}$$

Likewise, if the factor k is set to $\varepsilon_2^{HbO2} / \varepsilon_5^{HbO2}$, then the effect of the oxyhemoglobin changes on Eq.5.4 is eliminated. Thus,

$$\Delta c^{Hb} = \frac{\Delta A_2 - k\Delta A_5}{l\left(\varepsilon_2^{Hb} - k\varepsilon_5^{Hb}\right)} \quad (\text{where } k = \varepsilon_2^{HbO2} / \varepsilon_5^{HbO2}) \tag{4.6}$$

Thus far, we have decoupled the effects of the changes in oxyhemoglobin and deoxyhemoglobin concentrations on the Eq.5.2 that can be estimated from the color images captured over time by the smartphone after multispectral conversion (Eq.5.1). In doing so at each pixel in the video image, the spatiotemporal changes of decoupled oxyhemoglobin and deoxyhemoglobin concentrations (i.e., Δc^{HbO2} and Δc^{Hb}) within the dynamic blood perfusion within the light interrogated tissue volume can be obtained, but scaled by the light interaction path length. For simplicity, we assume that the light interaction path length for oxyhemoglobin and deoxyhemoglobin is constant and takes a value of 1 mm in the current study. A further discussion about this assumption is provided in Discussion Section.

4.2.4 ANALYSIS OF BLOOD PULSATIONS

It is known that heart pumping leads to pulsatile blood volume propagating throughout the body tissue. This pulsatile modulation of the blood volume results in the absorption modulation of the light propagating within the skin, which in turn leads to the intensity modulation of light reflected from the skin tissue. Assuming that the oxygenated and deoxygenated bloods are responsible for this absorption, the derived spatiotemporal changes in oxyhemoglobin and deoxyhemoglobin concentrations in the last Section would also behave pulsatile, which can be used to analyze and indicate the blood volume pulsations within the light interrogated skin tissue volume in this study.

To recover spatiotemporal pulsation of the dynamic blood perfusion, we applied a window-based lock-in amplification algorithm [112][112][126] on the time varying oxyhemoglobin and deoxyhemoglobin signals obtained by Eq.5.5 and Eq.5.6. First, we selected a 5-second time window starting from the first frame. In the window, we built a standard function with its temporal heart rate frequency. The heart rate was extracted by conducting fast Fourier transformation of the global perfusion data in the window. The standard function can be expressed as:

$$R(t) = \cos(\omega_h t) - i\sin(\omega_h t) = e^{-i\omega_h t} \tag{4.7}$$

where $R(t)$ is the standard reference function constructed by the known heart beating frequency ω_h. The dynamic blood perfusion signal at each pixel (x, y) obtained from the last Section can be expressed through Fourier series expansion:

$$\begin{aligned} \Delta c(x,y,t) &= \sum_m \sum_n AM_{mn}(x,y)\cos[\omega_m t + \theta_n(x,y)] \\ &= \sum_m \sum_n \frac{AM_{mn}(x,y)}{2}\left\{e^{i[\omega_m t+\theta_n(x,y)]} + e^{-i[\omega_m t+\theta_n(x,y)]}\right\} \end{aligned} \tag{4.8}$$

where $\Delta c(x, y, t)$ is the input signal representing the changes in hemoglobin concentration contained in the dynamic blood volume at time t. $AM_{mn}(x, y)$, ω_m and $\theta_n(x, y)$ are the amplitude, frequency and phase of the input signal at the pixel (x, y).Therefore, the signals solely due to the heartbeat at the frequency ω_h embedded within $\Delta c(x, y, t)$ can be recovered by applying lock-in detection [113][113][127]:

$$Z(x,y) = \sum_t R(t)\Delta c(x,y,t)$$

$$= \sum_t \sum_m \sum_n \frac{AM_{mn}(x,y)}{2} \{ e^{i[(\omega_m - \omega_h)t + \theta_n(x,y)]} + e^{-i[(\omega_m + \omega_h)t + \theta_n(x,y)]} \} \quad (4.9)$$

where $Z(x,y)$ is the time integral of the product of the standard reference function *R(t)* and the input signal of $\Delta c(x,y,t)$. Per lock-in detection mechanism, when the components of input signals have the frequencies that differ from the standard reference frequency (i.e., ω_h), the product would oscillate in time and approach to zero. However, when the signal is of the same frequency as ω_h, the product would be retained and amplified. Assuming the phase of the heart cycle at pixel (x,y) is constant over time, the output of the lock-in detection can be simplified as,

$$Z(x,y) = \frac{AM_h(x,y)}{2} e^{i\theta_h(x,y)} \quad (4.10)$$

where $AM_h(x,y)$ and $\theta_h(x,y)$ are the amplitude and phase of the extracted cardiac pulsation signal, respectively. Consequently, the pulsation amplitude at pixel (x,y) can be calculated as below:

$$AM_h(x,y) = 2abs[Z(x,y)] = 2abs[\sum_t R(t)\Delta c(x,y,t)] \quad (4.11)$$

By moving the evaluating time window along the time axis across the entire video frames, the spatial and time-resolved pulsation of blood perfusion within the light

interrogated skin tissue volume can be obtained. Since the dynamic blood contains oxygenated and deoxygenated blood, the pulsation amplitudes separately evaluated from the oxyhemoglobin and deoxyhemoglobin signals (i.e. Eq.5.5 or Eq.5.6) must be equal and the same as the pulsation amplitude of the whole blood volume.

A flow chart for the signal processing procedures described above is given in Figure 4.3. After the videos are captured by the smartphone, the time trace of signals in the RGB channels are first converted into the multispectral data cube through the transformation matrix obtained by calibration (Eq.5.1). In this study to achieve our purpose, we converted the RGB colors into the six spectral wavelengths at 450, 500, 550, 600, 650 and 700 nm, respectively. Then, the changes in light absorbance at 500 and 650 nm were calculated (Eq.5.3) with reference to the frame at the time zero (i.e., the start of video frame of interest). Afterwards, the spatiotemporal changes in oxyhemoglobin and deoxyhemoglobin concentrations within the dynamic blood volume are decoupled by weighted subtraction method (Eq.5.5 and Eq.5.6). Finally, the spatiotemporal pulsation is mapped by the window-based lock-in detection mechanism (Eq.5.9 and Eq.5.11).

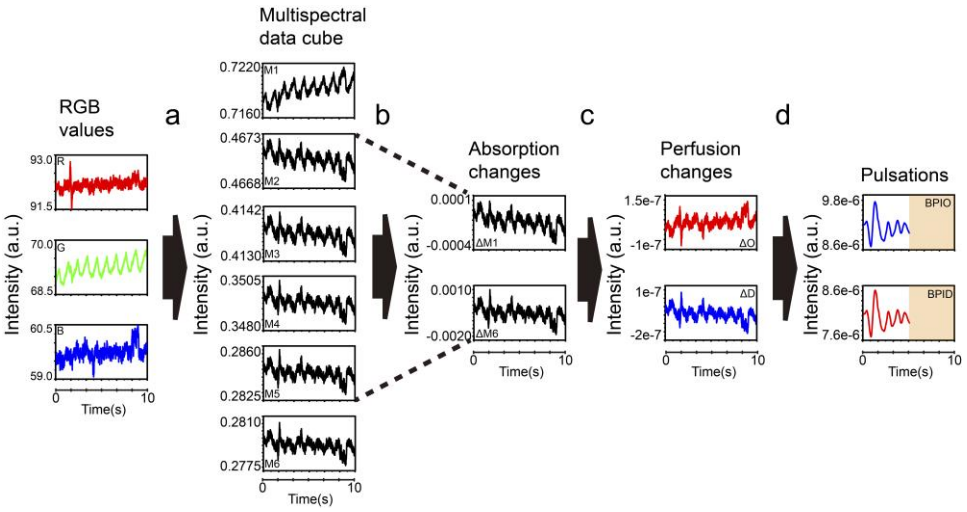

Figure 4. 3. The schematic of signal processing steps to derive the spatiotemporal changes in oxyhemoglobin and deoxyhemoglobin and their pulsation amplitudes from the video images captured by the smartphone. (a) The RGB color video is first converted to multispectral video cube, where multispectral cube contains 6 wavelengths of 450, 500, 550, 600, 650 and 700 nm in this study. (b) The time-varying spectral signals of selected wavelengths at 500nm and 650nm are used to calculate (c) the spatiotemporal changes in the oxyhemoglobin and deoxyhemoglobin concentrations in the blood volume within the light interrogated tissue volume. (d) Finally, the spatial pulsation amplitude is evaluated from either dynamic oxyhemoglobin or deoxyhemoglobin signals resulted in the step (c).

4.2.5. EXPERIMENTAL DEMONSTRATION CONSIDERATIONS

Having described the methods and formulations of SP-rmPPG to monitor the changes in oxyhemoglobin and deoxyhemoglobin concentrations and pulsatile blood volume in the light interrogated skin tissue from smartphone recorded videos, we conducted two experiments to demonstrate its feasibility to reveal oxygenation and pulsation changes during flow-challenged conditions. The first experiment was designed around the popular blood cuff maneuver at the upper arm to gradually occlude the blood draining venules. The second experiment was designed to simulate the occlusive external carotid artery (or more precisely the facial artery) that supplies the facial skin tissue beds.

In the 1st experiment (Experiment I), we applied a standard medical grade manual blood cuff to condition the blood supply and drainage in the left upper arm, and then used our proposed SP-rmPPG system to monitor the development and evolution of blood hemodynamics in the dorsal skin of the left hand. With the hand placed on the desk steadily to avoid relatively large motion, videos were taken by the smartphone while the cuff pressure was being applied. In parallel, a medical grade contact-mode sensor-based pulse oximeter (PC-66H Handheld Pulse Oximeter, CMI Health, USA) was used to monitor the peripheral oxygen saturation (SaO2) at the left little finger. Five trials of the experiments were conducted by applying 0 (control), 50, 70, 90 and 110 mmHg cuff pressures on the upper arm until the SaO2 as measured by the pulse oximeter reached a level of 97% (control), 96%, 95%, 94% and 93%, respectively. For each experimental trial, we started the video recording at the time when the cuff pressure was applied. After the target SaO2 level was reached as monitored by the pulse meter and stabilized for 20 seconds, we released the cuff pressure and continued the video recording for next 10 seconds. We labeled these 5 trials as: c1– 0 mmHg/97% (control), c2 – 50 mmHg/96%, c3 – 70 mmHg/95%, c4 – 90 mmHg/94%, c5 – 110 mmHg/93%. For example, for the trial c5 (110 mmHg/93%), the cuff pressure applied was 110 mmHg. The onset of the continuous video recording was at the time when the cuff pressure started at the upper arm. The cuff pressure was continuously being applied until the SaO2 value measured by the pulse oximeter reached at the level of 93%, at which time the pressure was released. And the video recording continued for another 10 seconds.

The 2nd experiment (Experiment II) was designed to demonstrate whether the smartphone system is able to observe the changes in blood oxygenation and associated

blood pulse strength at the facial skin when the external carotid artery that supplies maxillofacial region is challenged. There are two branches of the facial arteries symmetrically located at the lower jaw region near neck, supplying the nutritive blood to the facial skin tissue beds. We simulated partial occlusive (or ischemic) condition within the skin tissue beds by gently pressing on the facial artery while continuously recording the videos of the light reflectance emerging at the facial skin surface using the smartphone. To avoid motion, the head was placed on the chin rest in a slit lamp setup. Below are the brief procedures of the experiment. First, the volunteer used finger-touching method to locate the artery position by feeling pulse below the jawbone. Then, the smartphone started to continuously record the skin videos, initially without applying finger pressure on the artery. Approximately 15 seconds after the onset of the video recording, the volunteer applied a gentle pressure to press the artery to produce partial occlusion on the artery to limit the blood supply to the corresponding facial skin tissue beds. The applied pressure lasted for 20 seconds and then removed. The video recording was finally ended at the time when a period of 60 seconds was reached. We conducted two separate experiments using this procedure on the facial artery located at both sides of lower jaws: first on the left, and then on the right. Another set of experiment was also conducted without applying the pressure on the artery, which was treated as the control.

4.3 RESULTS

4.3.1 CHANGES IN OXYHEMOGLOBIN AND HEMOGLOBIN CONCENTRATIONS DUE TO BLOOD CUFF MANEUVER ON THE ARM.

The maneuver of blood cuff pressure on the upper arm progressively occludes relatively superficial venules that drain the blood from the forearm. This action would expect a

gradual increase of the deoxygenated blood pooling at the downstream of skin beds and a gradual decrease of oxygenated blood. Figure 4.4(a) show the representative maps indicating the changes in oxyhemoglobin and deoxyhemoglobin concentrations at the dorsal skin tissue beds of the challenged left hand, extracted from the spatiotemporal images at four observation time points of each experimental trial: 1) the onset of the application of pressure cuff on the upper arm, 2) the time instant at the halfway of the video recording, 3) the time instant when the pressure cuff was released, and 4) the finishing time of the video recording. For all the experimental trials except for the zero-cuff pressure (i.e., the control), the decrease in oxyhemoglobin concentration within the skin tissue beds were observed with the application of pressure cuff, whereas the opposite trends were true for HEMOGLOBIN concentration. After releasing the cuff pressure on the upper arm, a rapid recovery of the oxyhemoglobin and deoxyhemoglobin was seen. Comparing among different trials, the degree of changes in oxyhemoglobin and deoxyhemoglobin concentration from onset to release agrees positively with the level of pressure applied.

To demonstrate the temporal profile of the measured signal, we selected a region of interest (ROI) on the dorsal hand skin and calculated the averaged values of the changes at each frame in the time course of spatiotemporal dynamic images. The averaging operation for a selected region was for the purpose of improving the signal quality and reducing the noises because the smartphone camera that we used was only of 8-bit depth. The time traces of the measured SaO2 values are shown in Figure 4.4(b). In Figure 4.4(c), we show the time traces of decoupled oxyhemoglobin and deoxyhemoglobin. As expected, the changes in oxyhemoglobin concentration show a continuous decrease with the cuff on and a rapid recovery right after the cuff was released. The opposite trends are observed for the changes

in deoxyhemoglobin concentration. These results match well with the values of oxygen saturations given by the pulse oximeter (Figure 4.4(b)). Decreased oxygenation values indicate decreased concentration of the oxygenated blood within the skin tissue beds. We also calculated the changes in total hemoglobin concentration for each experimental trial by summing corresponding changes in oxyhemoglobin and deoxyhemoglobin together (Figure 4.4(d). Except for the control, the changes in total hemoglobin concentration increase in all trials. Since venules are located more superficially than arteries in the upper arm, the application of cuff pressure causes severer occlusion in venules than arteries, leading to gradual blood pooling in the downstream of the forearm, indicating the validity of the results observed in the experiments. It is worthy to mention that all the values of concentration changes (Δc) were calculated when the light interaction path length (l) was assumed to be 1 mm. The real values of Δc can be affected by this assumption and can be improved by a more realistic l under specific illumination and imaging conditions.

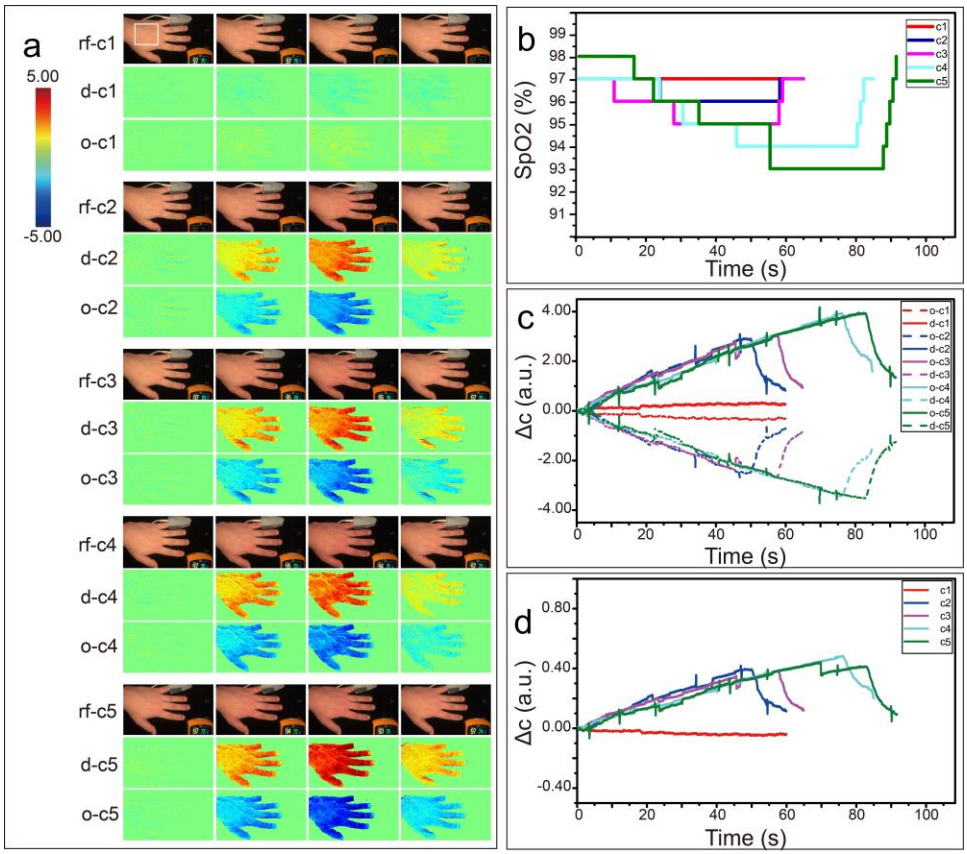

Figure 4. 4. The SP-rmPPG can provide information about spatiotemporal changes in oxygenated and deoxygenated blood within the light interrogated dorsal skin tissue in the hand during a routine blood cuff procedure applied on the upper arm.

The changes in oxyhemoglobin and deoxyhemoglobin concentrations were estimated from the smartphone recorded videos of a volunteer's hand when the upper arm was applied with a pressure by the cuff, using the proposed SP-rmPPG algorithms. The results shown were obtained from 5 experimental trials: c1– 0 mmHg/97% (control), c2 – 50 mmHg/96%, c3 – 70 mmHg/95%, c4 – 90 mmHg/94%, c5 – 110 mmHg/93%. (a) Representative reflectance (rf), deoxyhemoglobin (d) and oxyhemoglobin (o) images extracted from the spatiotemporal images at four-time instants: 1) the onset of the application of pressure cuff on the upper arm, 2) the time instant at the halfway of the video recording, 3) the time instant when the pressure cuff was released, and 4) the finishing time of the video recording. (b) The time trace of measured oxygen saturation values from the pulse oximeter. (c) The time traces of averaged values of decoupled oxyhemoglobin and deoxyhemoglobin changes within the selected region of interest (ROI) shown in the top left figure in (a). (d) Time traces of averaged values of the total hemoglobin changes within the selected ROI. rf – reflectance image, o – oxygenated blood, d – deoxygenated blood.

4.3.2 PULSATIONS OF OXYGENATED AND DEOXYGENATED BLOOD IN CUFF PRESSURE EXPERIMENTS

With the obtained spatiotemporal changes of oxygenated and deoxygenated blood due to the blood cuff maneuver at the upper arm, we applied a window-based lock-in amplification algorithm described in Section 2.4 to map the spatial pulsation amplitudes at the skin tissue beds as imaged by the smartphone. Since the experiment was conducted with the subject in sitting position that made the forearm about 20 cm below the heat level, the blood pulsation in the hand skin beds would be relatively weaker when compared to the positions that are above the heart level, due to the gravity effect. Therefore, we applied a longer time window of 10 seconds to maximally extract the heart frequency signal. It was successful to map the blood pulsation strengths for all the experimental trials conducted. As an example, Figure 4A show the spatial pulsation maps resulted from the respective spatiotemporal changes of oxyhemoglobin and Hemoglobin concentrations, when 110 mmHg cuff pressure was applied at the upper arm of the subject (i.e., the trial c5). Figure 4.5(b) illustrates the corresponding time traces of the pulsation strength averaged within the selected ROI (square region marked in the upper left figure in Figure 4.4). It can be observed that the blood pulsations remain relatively weak when the cuff pressure was applied, while being approximately the same strength for both the oxygenated and deoxygenated blood volumes. These are expected because mathematically and physically, the pulsation derived from the dynamic concentrations of either oxyhemoglobin or Hemoglobin should be the same as the total effective blood volume. Upon after releasing the cuff pressure, the blood pulsation shows a significant re-bound, indicating that both oxygenated and deoxygenated blood are experiencing a recovery associated with a strong

pulsation, which is more clearly illustrated in the time trace curves of the average pulsation intensity in the selected ROI (Figure 4.5(b)).

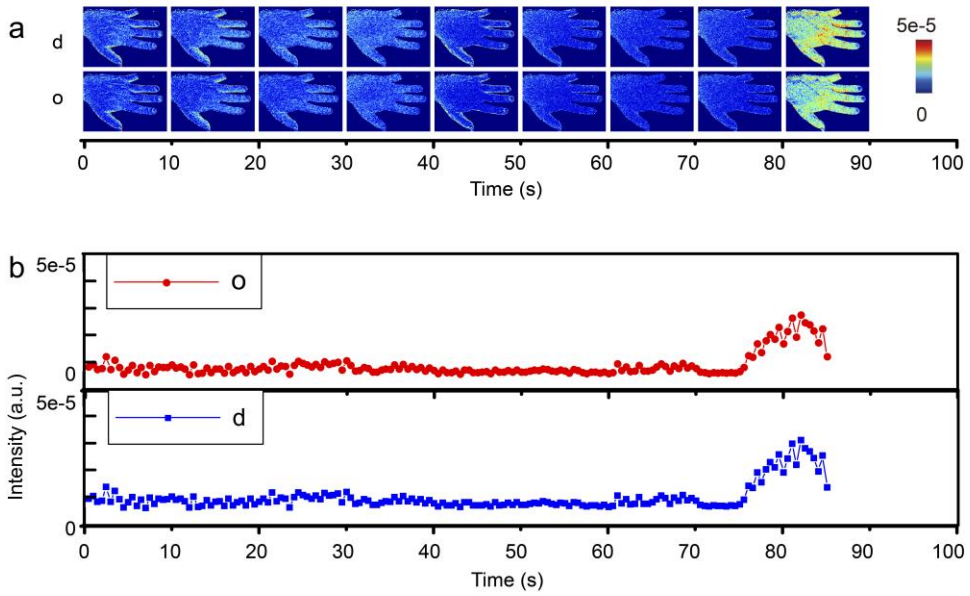

Figure 4. 5. Dynamic blood pulsation maps can be obtained from the spatiotemporal changes in oxyhemoglobin and Hemoglobin concentrations as evaluated from the smartphone recorded videos.
(a) Representative pulsation maps at the time instants as shown derived from the respective Deoxyhemoglobin (top row) and oxyhemoglobin signals (bottom row) when a 110-mmHg cuff pressure was applied at the upper arm until the oxygen saturation at the little finger reached 93% as monitored by the pulse oximeter, i.e., the experimental trial c5: 110 mmHg/93%. (b) Corresponding time traces of the pulsation strengths averaged from the selected ROI, derived from both the oxyhemoglobin (Top) and Deoxyhemoglobin signals (bottom), respectively, evaluated from a time window of 10s sliding through the entire recording time with a step time length of 0.5s. Cuff releasing time was at ~80s. Oxygenated blood is indicated by the label of "o", and deoxygenated blood by "d" in the figure.

4.3.3 CHANGES IN OXYHEMOGLOBIN AND DEOXYHEMOGLOBIN CONCENTRATIONS IN FACIAL SKIN

After conducted feasibility study using the popular blood cuff maneuver on the subject's upper arm, we next performed the experiments to demonstrate whether the proposed SP-rmPPG can monitor the changes of oxyhemoglobin and deoxyhemoglobin within the facial

skin tissue beds (See the procedure in Section 2.5). With the finger pressed on the facial arteries located at the lower jaw region to partially occlude the blood supply to the facial skin tissue beds for ~20s duration at ~15s after the onset of the video recording, Figure 4.6(a) shows the representative dynamic facial skin maps of the changes in oxyhemoglobin and deoxyhemoglobin at the time instants of 1s, 30s and 60s, respectively, when the left facial artery branch was pressurized. The corresponding time traces of oxyhemoglobin and deoxyhemoglobin changes on left and right cheeks are shown in Figure 4.6(b) that were assessed by averaging the values within the regions of interest (the region marked by white boxes in the top left figure) at each frame for the entire time-period of video recording. During the first 15s, both the oxyhemoglobin and deoxyhemoglobin signals are fluctuating around the zero level. At the time when the left facial artery was challenged by applying pressure on it, the oxyhemoglobin started to rapidly decrease and deoxyhemoglobin to increase at the left cheek, while the changes at the right cheek region were minimal. With the pressure sustained at the position for a period of 20s, the decrease in oxyhemoglobin and increase in deoxyhemoglobin sustained in the left cheek, but at a much slower rate. Afterwards, the changes rapidly re-bounded when the pressure was released and then slowly approaching the initial normal level. Such behaviors of changes in oxyhemoglobin and deoxyhemoglobin are expected from normal physiology for a tissue region that experiences a temporary shortage of blood supply (i.e., a transient ischemic attack) [43]. However, a slight opposite trend of changes in oxyhemoglobin and deoxyhemoglobin was observed at the contralateral right creek, where the blood supply was not limited, but the oxyhemoglobin was seen slightly increase and deoxyhemoglobin decrease during the partial occlusive maneuver on the left facial artery, and then the trend reversed after the

pressure was lifted. This may be explained by the symmetrical relationship of arterial supply and venular drainage between the left and right cheeks where an ischemic impairment at one side would likely evoke a response at its dependent contralateral side, trying to balance circulation system likely due to microvascular or sympathetic nerve autoregulation [114][114][128].

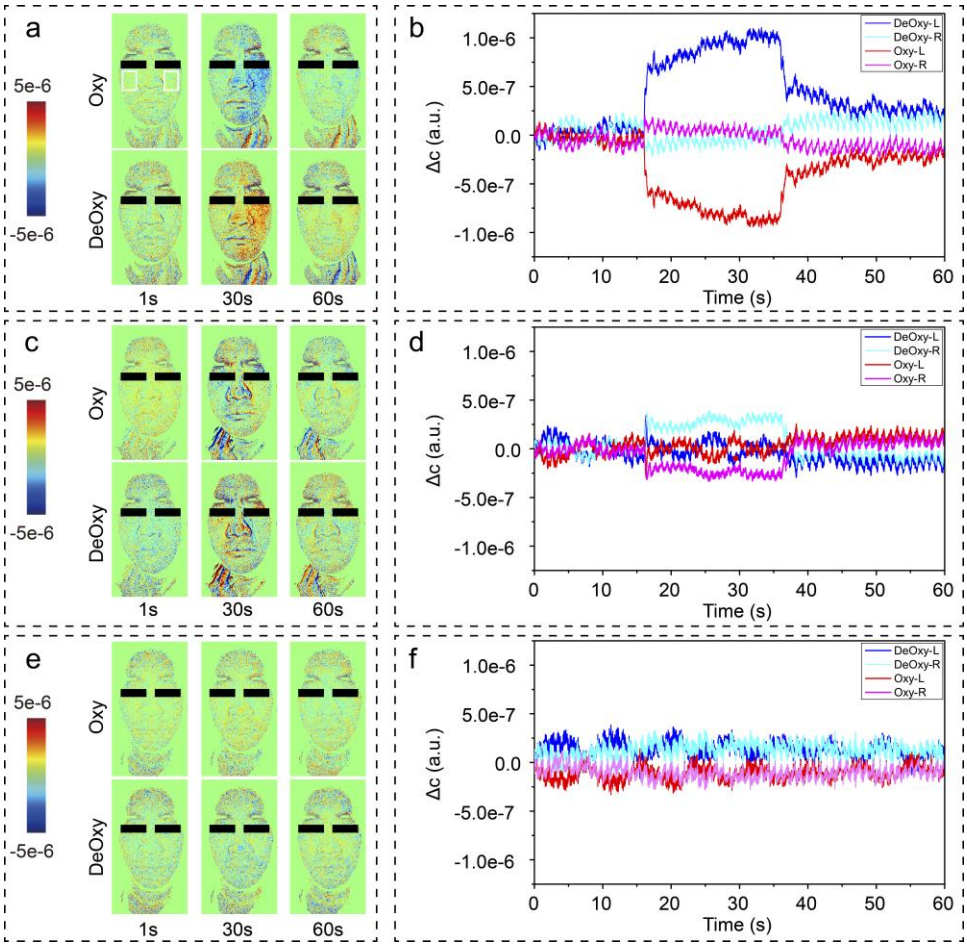

Figure 4. 6. The proposed SP-rmPPG can provide dynamic information of oxyhemoglobin and deoxyhemoglobin within the facial skin tissue beds when blood supply is limited by pressing the facial arteries in the lower jaw region.

(a) The representative maps of oxyhemoglobin (top row) and deoxyhemoglobin (bottom row) changes of the facial skin at three time points (1, 30 and 60s) when the left facial artery was pressed at the time of ~15 s after the onset of the video recording. White box area in the top left figure indicates the selected ROIs for evaluating the temporal time trace

signals. (b) Time traces of averaged values of oxyhemoglobin and deoxyhemoglobin changes within the selected ROIs (R: right cheek, L: left cheek) shown in (a). (c) and (d) the same as in (a) and (b), respectively, but the right facial artery was limited. (e) and (f), the same as in (a) and (b), but the control experiment, i.e. no pressing on the facial artery was applied.

Figure 4.6(c) and (d) show the spatiotemporal changes in the oxyhemoglobin and deoxyhemoglobin of the skin tissue beds at both the right and left cheeks, albeit with the right facial artery challenged to limit the blood supply to right facial regions. The changes are observed the same as that of left-pressing experiment but with the trend reversed. However, the changes are in much smaller magnitude in this case, likely due to insufficient pressure on the right facial artery applied by the finger pressing. In Figure 4.6(e) and (f), we also show the spatiotemporal results of the control group. As expected, the perfusion changes are moderate and stable over the time period of smartphone video recording. These results sufficiently demonstrate that the proposed SP-rmPPG method is feasible to detect the dynamic oxygenation status within the facial skin tissue beds, simply by the use of a widely available and cost-effective smartphone.

4.3.4 PULSATIONS OF OXYGENATED AND DEOXYGENATED BLOOD IN FACIAL SKIN

The spatiotemporal pulsation maps of the facial skin derived from the spatiotemporal changes in oxyhemoglobin and Deoxyhemoglobin are shown in Figure 4.7 for the facial artery challenging experiments. The representative pulsation maps at the time instant of 20s extracted from the spatiotemporal images are shown in Figure 4.7(a), for the experimental trials of 1) left facial artery being challenged, 2) right facial artery being challenged, and 3) control. For the case of occluding left artery, lower pulsation amplitudes for both the oxyhemoglobin and deoxyhemoglobin are seen at the left side of the cheek

compared to its contralateral right cheek, indicating that limiting the blood supply to the skin tissue beds in the left cheek reduces its blood pulsation. The opposite change is true for the case of right artery challenging. However, there is no observed difference between the left and right cheeks for the control group, i.e., they remain symmetrical. Since the signal to noise ratio is relatively low due to the use of smartphone that has limited bit-depths (8-bits), we calculated the averaged pulsation amplitudes within the selected regions of interest (ROI) at each frame in order to improve the signal to noise ratio. The ROIs were selected symmetrically at the right and left cheeks, marked as white boxes in left figure of Figure 4.7(a). We then calculated the ratio of pulsation amplitudes between right and left cheeks in each time window to further contrast the imbalance of blood pulsation within the skin tissue beds at the right and left cheeks. In doing so, the time traces of the ratios of either deoxyhemoglobin (Figure 4.7(b)) or oxyhemoglobin (Figure 4.7(c)) pulsation amplitude in three trials can be obtained. It is observed that for the control group, the ratio sways between 0.8 and 1.0. However, for the left artery challenging case, the ratio reaches more than 1.3, while it becomes ~0.5 for the right artery challenge case. The ratios resulted from deoxyhemoglobin (Figure 4.7(b)) and oxyhemoglobin (Figure 4.7(c)) are almost identical, which is expected because the pulsations so evaluated should be the same and equal to the pulsation of total blood volume within the skin tissue beds. These results support the conclusion that the changes in blood pulsation due to the induced ischemia at the facial tissue beds can be measured by the smartphone, which may be useful in the applications of assessing cardiovascular diseases, for example strokes at risk where the obstruction of internal carotid artery is often the cause of stroke.

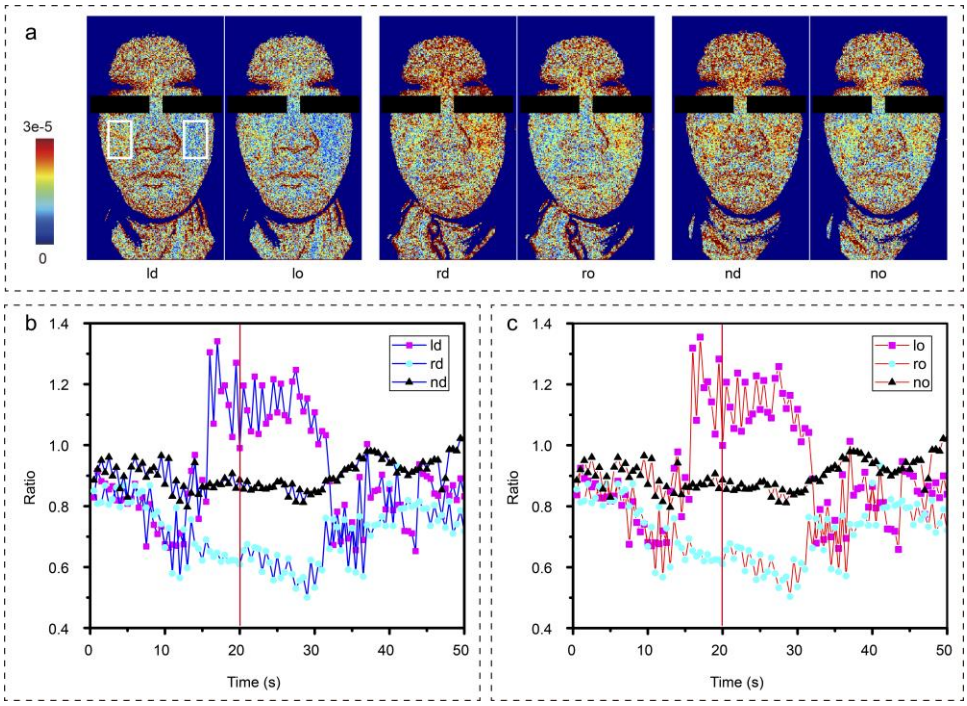

Figure 4. 7. The proposed SP-rmPPG is able to image dynamic changes of blood pulsation within the facial skin tissue beds upon the challenging of the blood supplying facial arteries.
(a) Representative pulsation maps extracted from dynamic images at the time of 20-second, derived from the spatiotemporal oxyhemoglobin (o) and deoxyhemoglobin (d) signals obtained from the facial skin for three experimental trials (l: challenging on left supplying artery; r: challenging on right supplying artery; n: control group without challenging). (b) The time traces of temporal ratios of averaged pulsation intensity values derived from dynamic deoxyhemoglobin signals between right and left cheeks at the selected ROIs (right/left). (c) The time traces of temporal ratios of averaged pulsation intensity values derived from dynamic oxyhemoglobin signals between right and left cheeks at the selected ROIs (right/left).

4.4 DISCUSSION AND CONCLUSION

We proposed a SP-rmPPG method and system to monitor the spatiotemporal changes in oxygenated and deoxygenated hemoglobin concentrations in the effective blood volume within the light interrogated skin tissue beds, and further to map the blood pulsation amplitudes. The results of cuff pressure experiments on the upper arm provided the feasibility of the proposed method to reflect the impact of the occlusion at the upstream

blood vessels on the downstream blood perfusion at the extremity of skin tissue beds. The results obtained by the proposed method agreed well with the parallel peripheral oxygenation measurements by the pulse oximeter. The spatiotemporal oxyhemoglobin and deoxyhemoglobin changes and the blood pulsations of the skin tissue beds at the challenged hand with and without cuff pressure at the upper arm also agreed with the expected changes in the cutaneous blood oxygenation in this well-known and popular blood cuff maneuver. We also demonstrated that the proposed method is capable of measuring the spatiotemporal changes in the oxygenated and deoxygenated blood within the facial skin when it was challenged by a transient ischemic event induced by artificially limiting the blood supply to the tissue region at the external carotid artery. The observed imbalance of the oxygen supply and the blood pulsations within the facial skin tissue beds between the left and right cheeks indicates that the proposed method may be useful in detecting or monitoring certain cardiovascular diseases like carotid stenosis, and in doing so by only taking selfie videos with a cost-effective smartphone.

The values of spatiotemporal oxyhemoglobin and deoxyhemoglobin changes that we obtained were scaled by the light interaction path length in the skin tissue (Eq.5.5 and Eq.5.6). We assumed this path length to be 1 mm in this study. From the measurements, we estimated that the averaged concentration changes of deoxyhemoglobin and oxyhemoglobin was ~16.5 μM for every 1% decrease of the SaO2 value from Figure 4.4(c). For a normal male subject, the concentration of total hemoglobin in the whole blood is approximately ~2500 μM [115][115][129]. In this case, every 1% decrease of SaO2 would be theoretically caused by the concentration changes of deoxyhemoglobin and oxyhemoglobin at ~25 μM. Consequently, the measured changes by the smartphone were

approximately in line with the theoretical predictions (which on the other hand, indicates the validity of the proposed SP-rmPPG method). Given the limited penetration depth of visible lights [116][116][130], thickness of epidermis and dermis in the dorsal skin of hand [117][117][131] and relatively weak illumination of the smartphone flashlight, the actual light interaction path length in our study is likely to be smaller than 1 mm. If this is the case, then the measured values would be closer to the theoretical value. Therefore, we believe that there is still a room to improve the accuracy of the measured changes in oxyhemoglobin and deoxyhemoglobin by carefully determining the practical and more realistic values of the light interaction path length in biological tissue through, for example, Monte Carlo simulations of the light (with the wavelengths of interest) propagating within the skin tissue [118, 119][118, 119][132, 133] taking into account the consideration of its proper optical properties [120][120][134] possibly combined with the measurements of optical coherence tomography of depth-resolved skin morphology and microcirculation information [84, 121][84, 121][99, 135]. Some specified study about the optical path length in PPG can also provide realistic values of l to improve the accuracy of measurements [52,53].

Compared with the conventional single-wavelength PPG (swPPG), the multiple-wavelength PPG (mwPPG) has been demonstrated to have superior performance in detecting the blood pulsation in terms of its signal quality and robustness, thus increasingly gaining attentions from both academic researchers and industrial entrepreneurs [122][122][136]. Most mwPPG sensors rely on the use of multiple light sources each with different wavelength or a more complicated spectrometer-like photodetector array, leading to a bulky system setup and associated complicated control to implement, let alone the cost

issues [123][123][137]. Nevertheless, such strategy has been adopted by many remote PPG (rm-PPG) systems [124, 125][124, 125][138, 139]. Due to the demand of the wide-field illumination and imaging, the system setup of a rm-PPG becomes even more complicated than mw-PPG does. In this study, we provided a simple solution to realize rm-PPG by employing unmodified and intact commercial smartphones through an algorithm that can convert the color images (video) captured by the built-in cameras into the multispectral video cubes. Due to the minimal constraints in hardware requirements, the proposed method provided an advantage of flexibility to select the wavelengths of interest and multi-channel processing. Though it is a "pseudo" multispectral imaging that we achieved, the method can still be used to decouple the dominant bio-chromophores from the videos of the dynamic light reflectance emerging at the skin tissue surface to realize a refined monitoring of skin hemodynamics. Besides, rather than simply detecting the heart rate and pulse waves, our method offers another perspective for the analysis and monitoring of spatiotemporal hemodynamic activities. For example, from the imbalanced hemodynamic responses between the left and right sides of the cheek, we may speculate the existence of vascular disorder in corresponding carotid arteries.

The experiments we conducted and analyzed in this study may be directly relevant to some clinical applications. The cuff pressure experiments on the upper limp could be a useful method in the assessment and monitoring of peripheral vascular diseases that cause the blood vessels outside of the heart and brain to narrow, block, or spasm, for example in the cases of arteriosclerosis, or even diabetes. The facial tissue imaging experiments may be useful in the assessment or prediction of possible obstruction of major blood supplying arteries to the downstream tissue beds, which might cause transient ischemic attacks and

even stroke. The proposed method can also be used to derive and spatially localize the lesion area from the field of view. In addition to the potential usage in clinical scenarios, there would also be a potential space for the SP-rmPPG system to be applied in general health care because of the current ever-growing accessibility and affordability of the smartphone to the general public. It may be envisioned that the future smartphone can have an ability to perform daily monitoring of the skin hemodynamics to support the early screening and interventions of the potential cardiovascular diseases.

Though as promising as it has been demonstrated, the limitations in the use of smartphone to realize rmPPG cannot be ignored. Since current commercial smartphones are not designed to fulfill the requirements for biomedical imaging, there are inherent limitations in their hardware design, including the camera sensor and the flashlight with limited wavelength range. Most smartphones employ 8~10-bit camera sensors and produce compressed 8-bit videos, presenting challenges to acquire blood pulse waveforms with high fidelity. Even with the compensation of illumination uniformity, the flashlight still provides limited irradiance to the target samples for imaging purposes and its available wavelengths are confined within the visible range limited by a near infrared filter within the housing. Due to these constraints, the measured spatiotemporal changes in oxyhemoglobin and deoxyhemoglobin by the proposed SP-rmPPG were inevitably noisy. We had to perform a good averaging within a selected region of interest to improve the signal to noise ratio of temporal change signals to derive oxyhemoglobin, deoxyhemoglobin and blood pulsation information. These limitations may be partly reduced if one has the ability to access its raw videos and to remove its near infrared filter by working together with the smartphone manufacturers. Alternatively, if resources permit,

these limitations can be removed by configuring a dedicated high-performance system that employs high bit-depth camera sensors and high irradiance light sources with appropriate working wavelengths of interest that extend from visible to near infrared region.

Currently, the experiments we conducted were used to simulate vascular diseases for a proof-of-concept study. It can be imagined that the real situation would be much more complicated and individualized. In future, we plan to apply the proposed system and method in clinical medical imaging for further refinements and optimizations, and to conduct proper clinical trials to determine its clinical utility. Meanwhile, due to the large data used in our method, the storage consumption and tedious signal processing also limit the usability. An alternate solution to mitigate this problem would be to adopt cloud computing and deep learning technologies to store and process the acquired data.

We have proposed and described a smartphone-based remote PPG (SP-rmPPG) system and method to spatiotemporally monitor the perfusion changes and pulsations of the circulating blood volume within the light interrogated skin tissue beds. In the method, the skin color videos captured by an unmodified smartphone camera was first converted into the multispectral data cubes, upon which to derive the spatiotemporal changes in oxygenation status within the skin beds through a novel algorithm that can decouple the chromophore determinants of oxygenated and deoxygenated hemoglobin. The corresponding spatiotemporal blood pulsation were then mapped by a window-based lock-in amplification method. We have demonstrated the feasibility of the proposed SP-rmPPG method using the popular blood cuff pressure maneuver on the upper arm to occlude the blood supply to the downstream tissue beds, where the measured dynamic information of oxygenated and deoxygenated blood in the downstream agreed well with the parallel

measurements of oxygenation saturation provided by the standard pulse oximeter. We have also showed the ability of the SP-rmPPG method to monitor the hemodynamic information within the facial skin tissue beds that were challenged by a transient ischemic event. Due to the ever-growing accessibility and affordability of the smartphone to the general public, the proposed system and method are expected to be useful in the vital sign monitoring, in the early screening of peripheral artery diseases and cardiovascular disorders, as well as in the investigations of vascular functions. In particular, due to its attributes of low-cost, compactness and usability, it is expected to serve the health care systems well in the rural areas where the medical resources are severely limited.

Chapter 5. DEVELOPMENT OF A MULTIFUNCTIONAL PLATFORM (SpeCamX) FOR AUGMENTED SMARTPHONE IMAGING AND ITS CLINICAL VALIDATION IN PREDICTING BLOOD BILIRUBIN LEVEL

5.1 BACKGROUND AND MOTIVATION

As a biomarker of liver functions, bilirubin has distinct absorption solely in the wavelength bands between 350 and 500 nm, thus can be detected using optical sensors[126, 127]. Aiming for a low cost and easy access, many researchers have committed themselves to explore the possibility to realize the BBL detection with smartphone cameras. Previous studies reported some strategies to detect BBL by extracting raw signals in RGB channels of photographs[128]. The Results show some potentials, but the prediction quality remains to be improved. Some other studies adopted additional color calibration, image segmentation and feature extraction steps to preprocess the data to retrieve more spectral information of subjects[129]. Though the prediction accuracy was improved, the added operations often require professional interventions which need to be accomplished off-line. In this case, smartphones were simply used as data collection units for experts rather than ready-to-use consumer devices, which unavoidably challenged their utilities to serve the public.

Multispectral imaging is capable of maximally recording the spectral information of subjects, thus being widely used in conducting life science research and providing public healthcare service[130, 131]. Realizing this technique on smartphones would create another space for exploitation to benefit our community, given the large user quantity, high

usage frequency and low cost. Here, we described a custom-developed mobile app termed SpeCamX for transforming smartphones into multispectral imagers without any additional hardware attachments or internal modifications. With this app, we can acquire a 27-channel multispectral data cube ranging from 420 to 680 nm by a single snapshot. From the acquired data cube, we assembled multiple functions in the app to estimate corresponding chromophores levels, including hemoglobin, pigmentation, bilirubin and et al. To investigate the estimation quality of this system and method, we installed SpeCamX on an unmodified smartphone and used it as a bilirubinometer to quantify the sclera pigmentation to predict BBL (Figure 5.1). In the clinical imaging of 320 LD patients, we realized CC over 0.9 between the SpeCamX-enabled predictions and TSB results. To validate the claimed augmentation, we compared the prediction based on SAL and RGBL in four typical machine learning algorithms including artificial neural network (ANN), support vector machine (SVM), k-nearest neighbors (KNN) and random forest (RF). Experimental results demonstrated that the SpeCamX-enabled SAL performs higher prediction quality, efficiency and stability than RGBL, especially when the date feeding was limited. Without additional customized hardware, our strategy has the potential to be widely duplicated in a cost-efficient and easy-to-use mode. Providing tests of BBL and other bio-chromophores in this manner should help the users who are facing low resource settings in their daily lives.

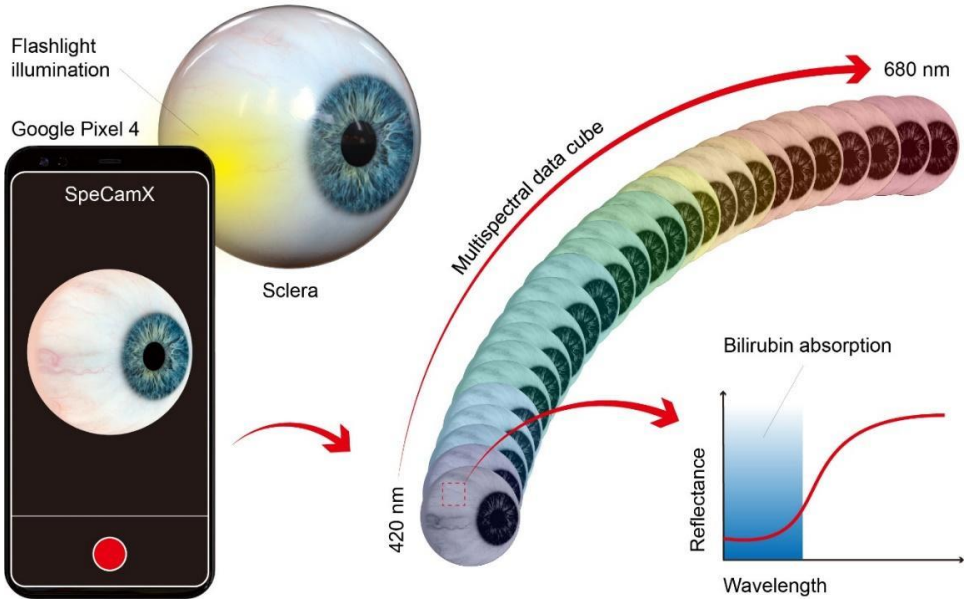

Figure 5. 1. Schematic of SpeCamX-augmented smartphone bilirubinometer.
The housed flashlight in a smartphone illuminated the sclera of patients. The installed SpeCamX acquired multispectral data cubes ranging from 420 to 680nm. The reflectance spectrum was averaged from the data cubes to predict BBL in further processing.

5.2 MATERIAL AND METHODS

5.2.1 CALCULATION OF TRANSFORMATION MATRIX

We calculated and embedded several TMs as default options for different phone models. For this purpose, we acquired RGB photographs of X-rite ColorChecker Classic with corresponding smartphones under the illumination provided by their flashlights. The color chart should be placed at a suitable distance with a smartphone to prevent overexposure (Maximum RGB value > 255) and under exposure (Maximum RGB value < 100). From the photographs, we sampled and calculated averaged RGB values of 24 color blocks. Then, the matrix can be calculated from the averaged signals of 24 color blocks. Using this method, we provided matrices for several most common-used smartphone models. We will

keep updating the supported phone models in the option. For functions that are not included in the current APP, we left an entrance for users to conduct their self-calibration of smartphones and illuminations, the calculation follows above steps as well.

5.2.2 DEVELOPMENT OF MOBILE APPLICATION

SpeCamX was developed using an open-source integrated development environment (IDE) Android Studio (Google, CA). The Weiner estimation algorithm and default TMs developed on Matlab R2021b were incorporated into the app. The "Imager" fragment can invoke the built-in camera and use it under default settings (Resolution: 2268X4032; f/1.7; shutter speed: 1/60; white balance: 5500K).

"Imager" fragments

The subject is labeled from the left top of the interface, which is autosaved together with date information in the filename of acquired data cubes for further references. According to different illumination conditions, we provided several options to set up the camera (Figure 5.2(b)). The default condition is to use built-in flashlight to illuminate subject. In this case, users can select their smartphone models in the "PHONE MODEL" option under the drop-down menu of settings. In this option, we pre-stored transformation matrices (TMs) to support a variety of smartphone models. Therefore, users can invoke corresponding matrices by simply selecting the smartphone model they use. As long as it is in dark environment, you are ready to go. In our clinical imaging test, the data were acquired using this setup.

In addition to the default setting, there are a number of other options for users to select if the requirement for default setting is not met, for example the smartphone that is in use

is not supported or the environment is not in dark condition. In these cases, the user can generate a customized TM on site through a self-recalibration step. In doing so, the user needs to first tap the “COLOR CHART” icon, in which there are provided with two options, i.e. either to use “24 blocks” or “96 blocks” to build the TM matrix (Figure 5.2(b)). Here, we used X-rite ColorChecker as the default color standard example for recalibration. The “24 blocks” option is provided for color charts with 24 classic color series. The available products include X-rite ColorChecker Classic/Passport/Mini/Nano (Figure 5.3). The “96 blocks” option works for X-rite ColorChecker Digital SG which includes expanded 96 color blocks with standard reflectance spectrums[132] (Figure 5.4). After selecting the color chart option, the user can tap into a calibration page and sample the on-site color chart by tapping the camera icon. In this page, a box array would be generated to guide the sampling of color blocks. For example, in the page of “24 blocks”, a 6 by 4 green box array would appear on the interface (Figure 5.2(c)). By pressing the photo button, the averaged RGB values in these boxes would be collected to compute a new TM with their reflectance spectra. During the calibration, the RGB values can be previewed on the top of corresponding boxes to prevent overexposure. The procedures for “96 blocks” option are the same but the box array is set to be 12 by 8. Furthermore, even under an illumination that cannot be controlled or stabilized, there is provided another option to perform real-time recalibration in the “COLOR CHART” tap, which is termed “co-illumination” strategy. In the “co-illumination”, the color charts and subjects will have to be placed with the same field of view for imaging, which will guarantee a shared illumination condition between the calibration and testing data cubes (Figure 5.5). For this purpose, we can manually adjust the relative positions and sizes of the sampling box array to avoid the

overlap between the color chart and the subject in the field of view. This strategy is suitable for trials if it is not possible to control the illumination environment, for example in the outdoor environment. Except for on-site imaging, users can also load previous or external data by tapping the “Add data” icon on the top of the interface. The acquired and uploaded data can be labeled with “C” and “T”, representing data for color charts and subjects, respectively. In this case, every smartphone installed with SpeCamX can act as a processing platform for an external data set.

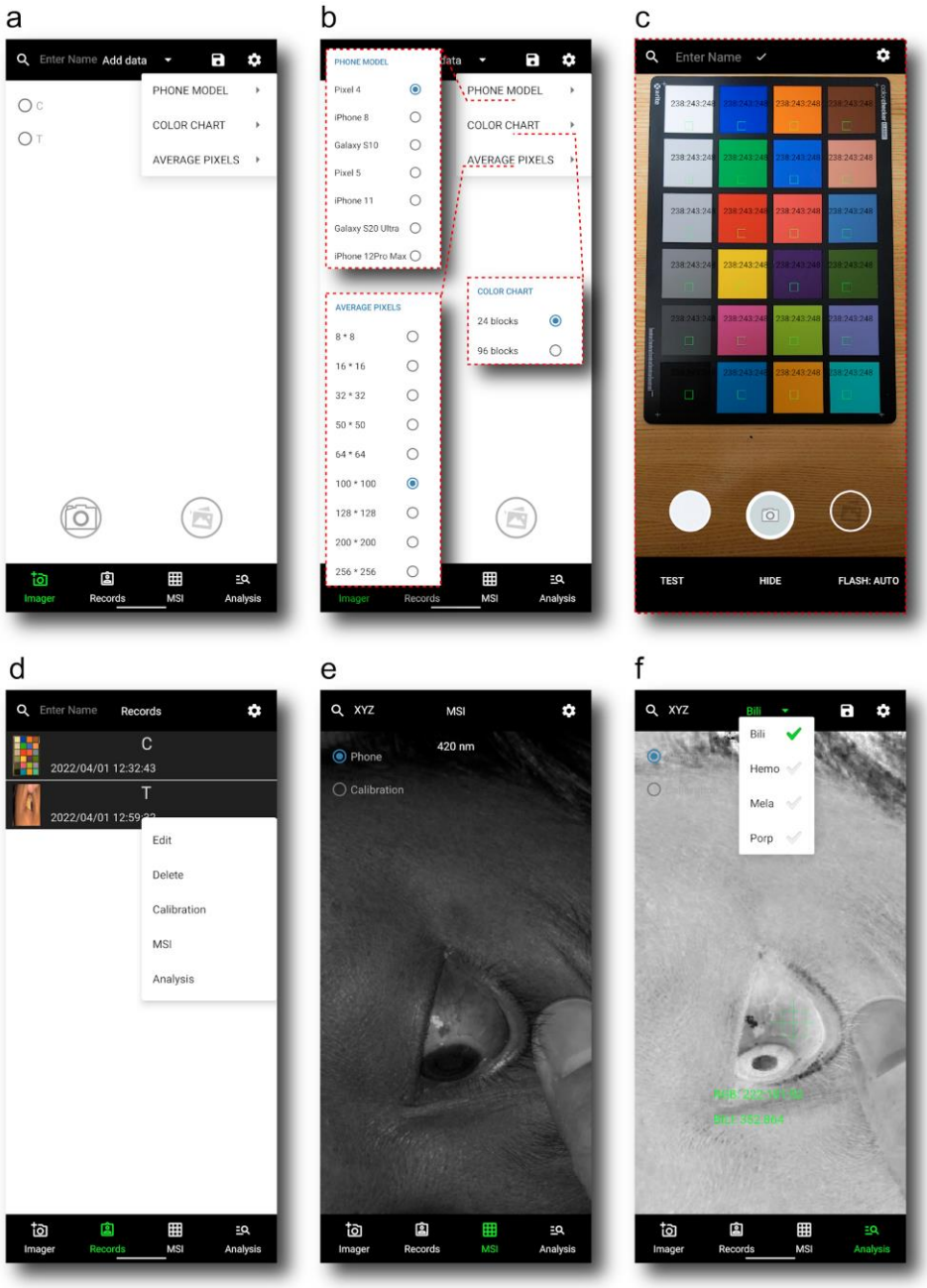

Figure 5. 2. Interfaces and functions of four fragments in SpeCamX.
(a) "Imager" fragment to set up the camera in the smartphone. (b) Supported functions in the setup options. (c) Recalibration page to generate a customized TM with a standard color chart. (d) Interface of the "Records" fragment, where users can check the list of acquired data. (e) "MSI" fragment for the presentation of the acquired spectral images of subjects. (f) "Analysis" fragment to present the information of the extracted feature.

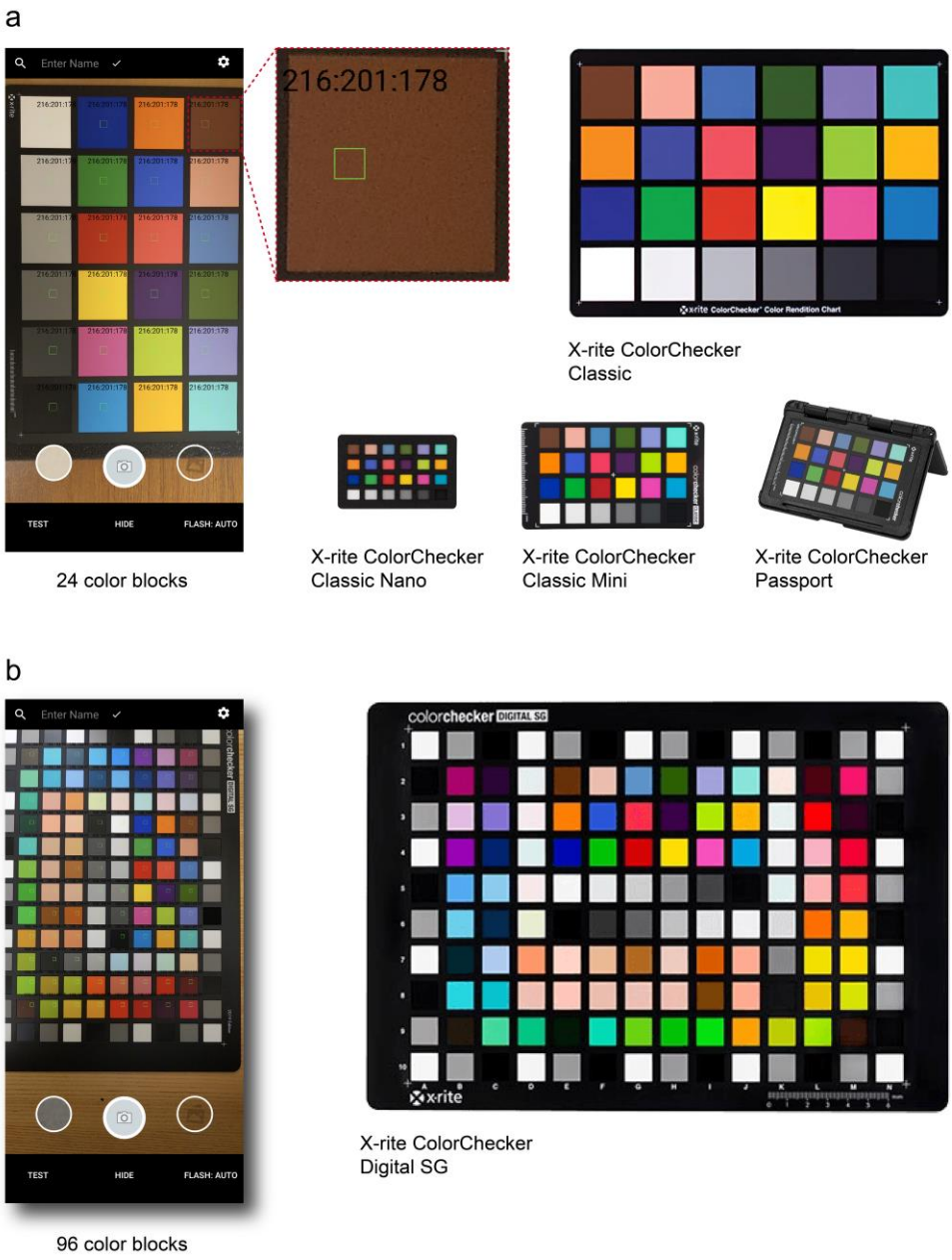

Figure 5. 3. Interfaces of the "24 blocks" and "96 blocks" calibration pages and compatible color charts for these options.
(a) "24 blocks" option for 24 classic colors. A 6 by 4 box array was previewed to guide the sampling of RGB values. The RGB values were previewed on the top of the sampling box. Standard color charts with 24 classic colors, like *X-rite ColorChecker Classic/ Passport/ Classic Mini/ Classic Nano*, can be used in this option. (b) "96 blocks" option for expanded colors. A 12 by 8 box array was previewed to guide the sampling of RGB values. *X-rite ColorChecker Digital SG* can be used in this option.

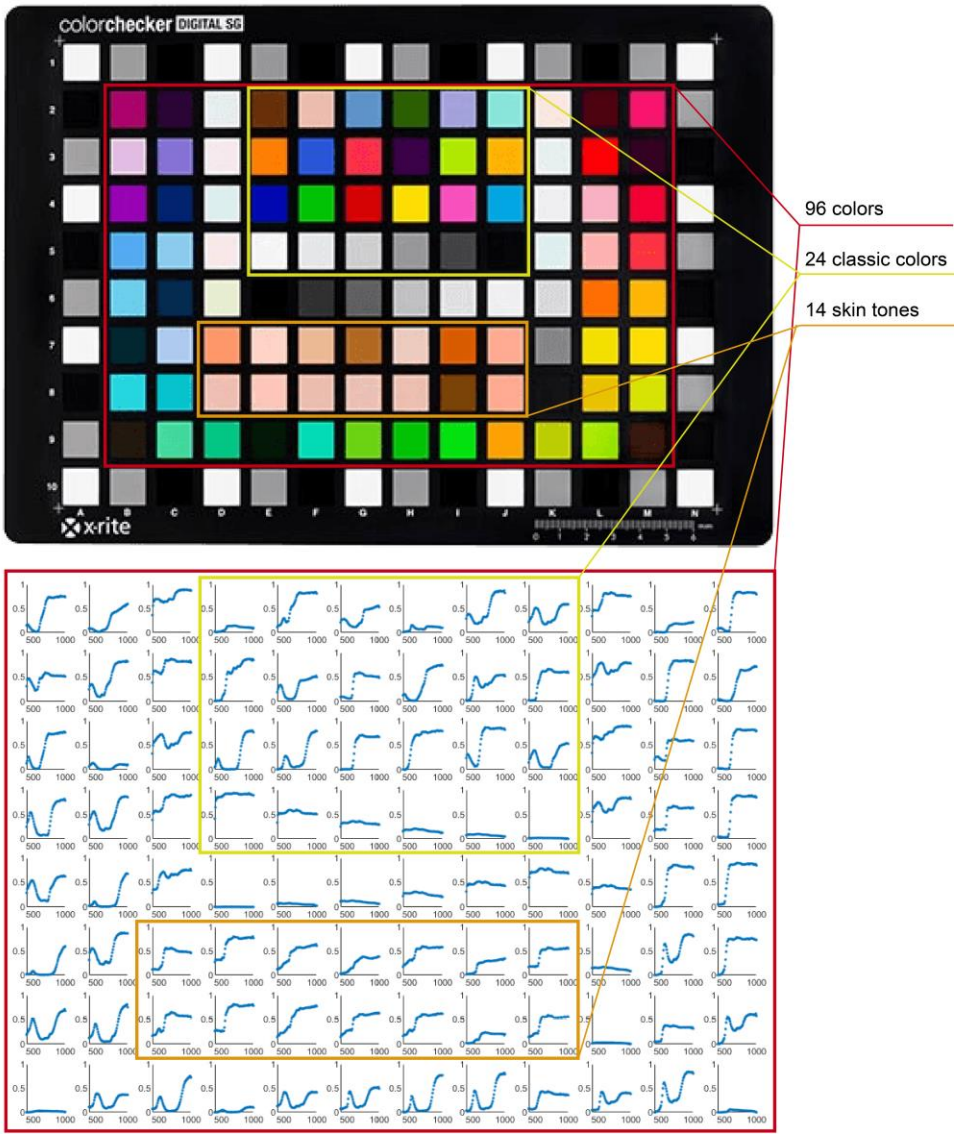

Figure 5. 4. Reflectance spectrums of 96 color blocks in X-rite ColorChecker Digital SG.

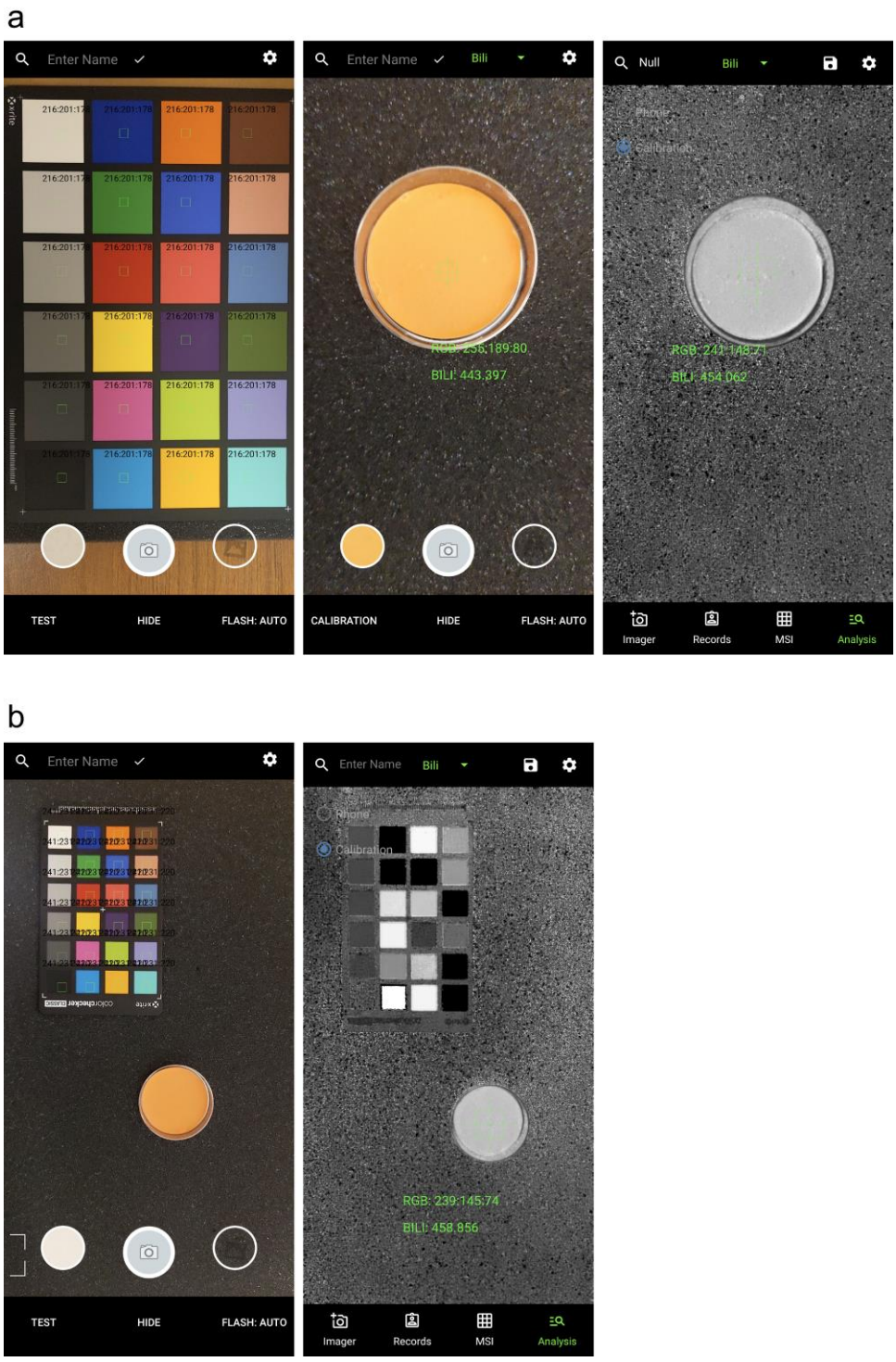

Figure 5. 5. Recalibration under uncontrolled and instable illumination. While the external illumination source cannot be controlled and stabilized, users can adopt a "co-illumination" step to realize real-time calibration.

> Instead of separately conducting “Calibration” and “Test” (a), the subject would be imaged with the color chart together in “Calibration”. To do this, the box array would be rescaled to make space for the subject (b).

“Records” fragments

The data specific to a subject can be recalled by selecting that subject or sliding the drop-down menu up and down to check the thumbnails. To edit the data, several operations, including “Delete”, “Calibration”, “MSI” and “Analysis” are offered by long clicking. “Calibration” is provided for color chart data labeled with “C” to calculate a new TM. Tapping “MSI” and “Analysis” can switch to the corresponding fragments to show the related information of the selected case.

“MSI” fragments

The grayscale images at wavelengths from 420 to 680 nm are presented in a scrolling display started with the corresponding RGB photograph (Figure 5.6). The wavelength is labeled on the top of each spectral image accordingly.

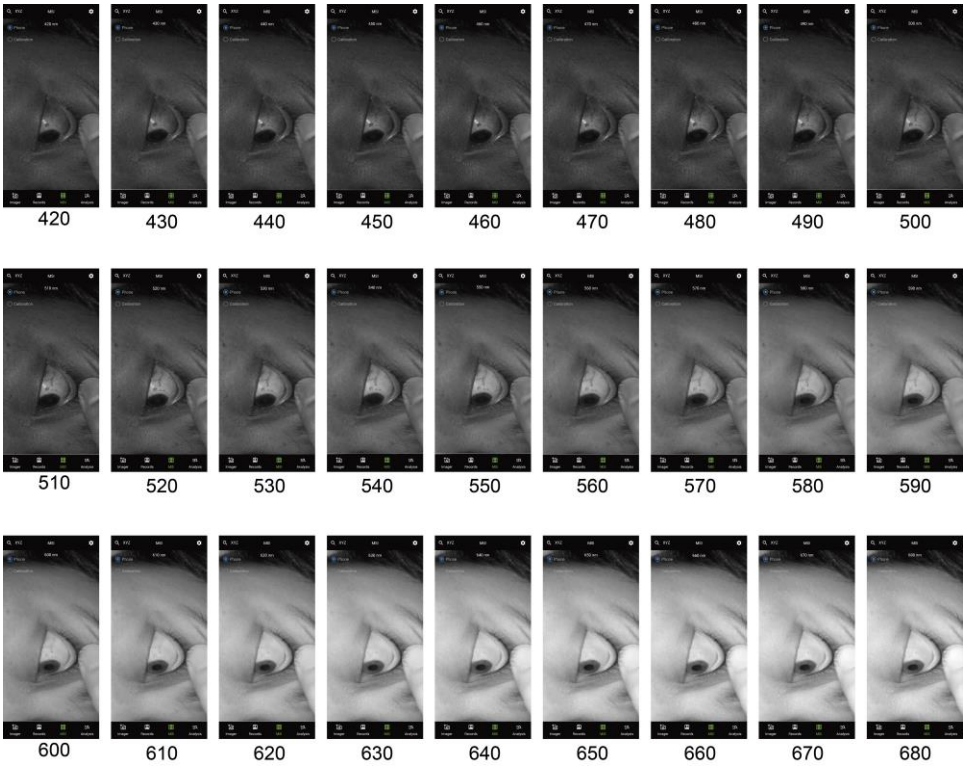

Figure 5. 6. The grayscale spectral images at wavelengths from 420 to 680 nm would be presented in the "MSI" fragment.
The images can be checked by scrolling the screen, the wavelength would be accordingly labeled on the image.

"Analysis" fragments

The BBL estimation results would be mapped in the "Bili" page, where a green box would guide the users to select a ROI. The averaged reflectance spectrum from the ROI would read out that provides the prediction of BBL. Considering the complexity of clinical imaging, we provided enough flexibility for the sampling procedure. The size of the ROI can be set in the "AVERAGE PIXELS" option (Figure 5.7) and its position can be manually shifted to the desired regions of interest. (Figure 5.8). Averaged RGB values in the ROI is shown in display so that the user can check to make sure the region is not overexposed. The shown "BILI" value represents the prediction made by the reflectance

spectrum averaged from the ROI. The prediction algorithm will be discussed later in this paper. The spectrum and predicted BBL are saved by tapping the photo icon for later use.

Except for the prediction of BBL (Bili) used in this study, SpeCamX also integrated algorithms to map other features like blood perfusion (Hemo), melanin pigmentation (Mela) and et al. Users can launch these functions by switching analysis algorithms from the drop-down menu on the top of the interface.

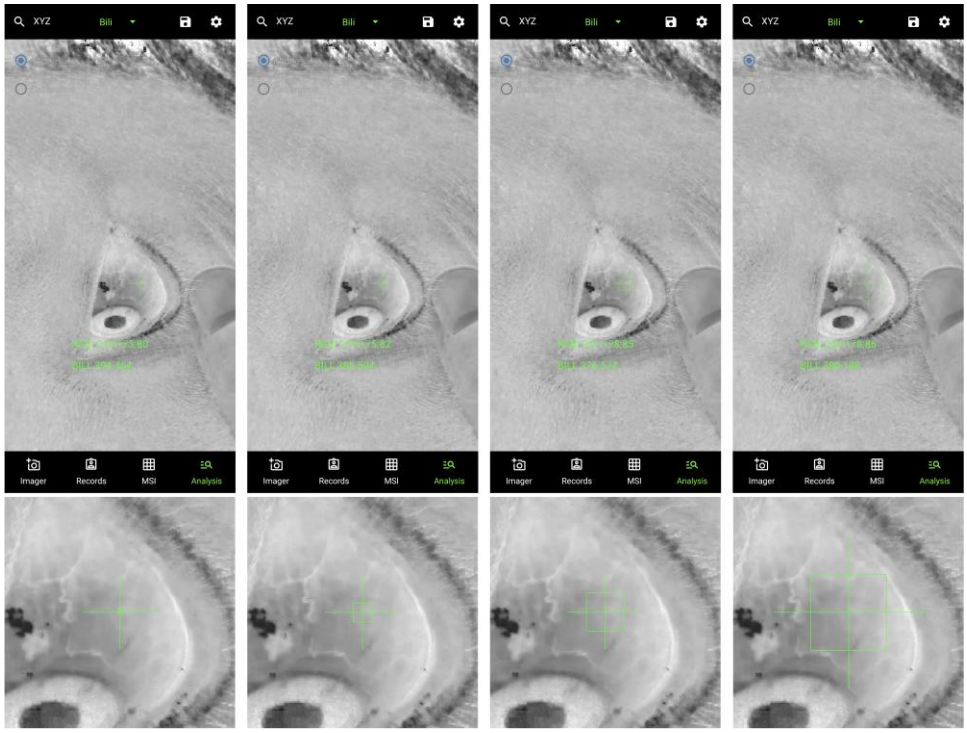

Figure 5. 7. The size of ROI can be set up in the “AVERAGE PIXELS”. Interfaces from the left to the right were under the setting of “8*8”, “32*32”, “128*128” and “256*256”, respectively.

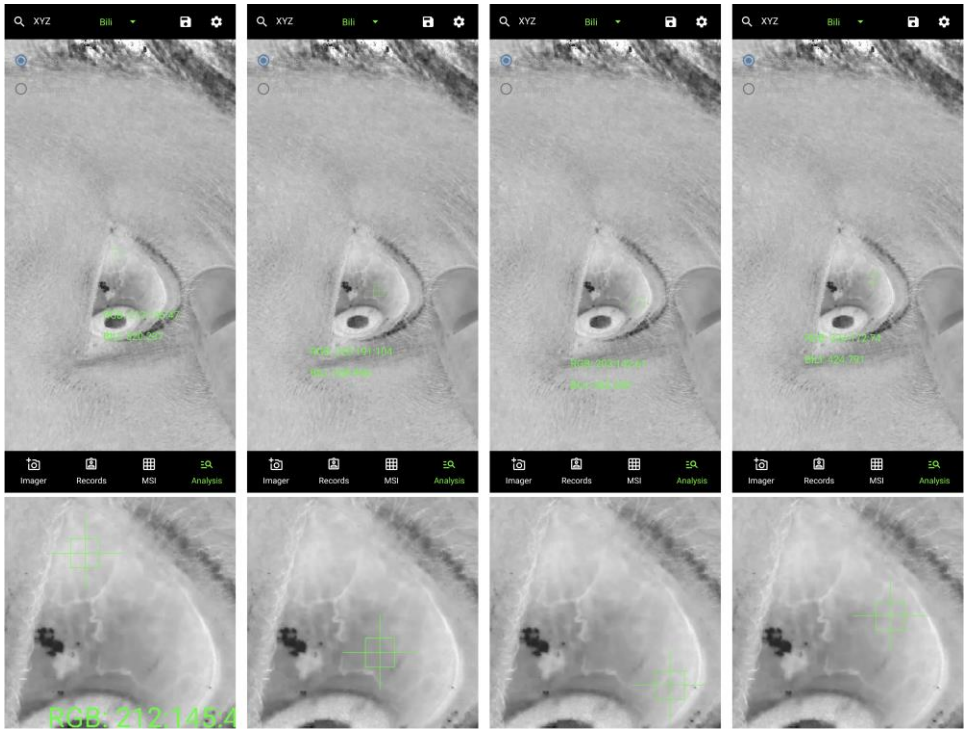

Figure 5. 8. Manual adjustments of the ROI position to sample different tissue regions by dragging the green marker.

5.2.3 CLINICAL IMAGING WITH MOBILE APPLICATION

This study adhered to tenets of the Declaration of Helsinki and was performed in accordance with the Health Insurance Portability and Accountability Act. Ethical approval was obtained from the Institutional Review Board of the University of Washington. Informed consent was obtained from the subject prior to the start of each study session. Anonymized and de-identified sclera images were collected from the First Hospital of Jilin University (Jilin, China). 320 patients with LD were enrolled in this study for SpeCamX to image/photograph their sclera at the anterior segment of the eye. Their diagnosis information was shown in Table 1. The photographing was conducted in a dark ward and the subject was illuminated by the smartphone flashlight, so no further color calibration is needed. Occasionally, some trials were conducted with some residue ambient light or room light. In this case, the smartphone was recalibrated on-site with a standard color chart.

Before imaging, the patient was asked to lie in the bed and keep their eyes open. The clinician held the smartphone and targeted sclera tissue. Then, the patient was asked to brink before taking each photo of the targeted region on the sclera. Ten 10 snapshots were taken for each participant. Each photo was then reconstructed into a multispectral cube as described before. For each data cube, a 100*100-pixel2 region was selected to calculate the averaged reflectance spectrum. Finally, the spectrum averaged from 10 snapshots would be used to predict BBL. Within 6 hours after imaging, the participants were subjected to standard clinical blood sampling to obtain their BBL.

5.2.4 MACHINE LEARNING REGRESSION ALGORITHMS TO PREDICT BBL

We compare SAL and RGBL in four different machine learning regression algorithms, including ANN, SVM, KNN and RF. We applied these regressions algorithms by invoking functions in the Statistics and Machine Learning Toolbox in Matlab R2021b. In ANN algorithm, we used *fitrnet* to train a 10-layer, feedforward, fully connected neural network to predict BBL. Function *fitrsvm* fits a support vector regression model. Function fitrsvm fits a support vector regression model. Function *kNNeighborsRegressor* estimates the values of a continuous variable (target) based on one or more independent variables (predictors) based on KNN algorithm. In the RF algorithm, we used *TreeBagger* to combine results of many decision trees to provide predictions. In the “Analysis” fragment of SpeCamX, the previewed value of “BILI” was averaged from SAL models using these algorithms.

All the statistical analysis, including regression CCs, Bland-Altman and ROC, were conducted using Matlab R2021b. 95% prediction bands were computed for the correlation plots. The bias error (MD) and 95% limits of agreement (LOA) were computed for the

Bland-Altman plots. LOA was computed as 1.96 times the standard deviation of the error. To create ROC curves, 320 cases were classified into positive and negative groups using 17.1 μmol/L as the threshold. All the plots and curves were generated using Origin 2021b.

The data that support the findings of this study are available from the corresponding author, but restrictions apply to the availability of these data, which were used under license for the current study, and so are not publicly available. Data is however available from the corresponding author upon reasonable request. The code that supports this work is copyright of the Regents of the University of Washington and can be made available through license.

5.3 RESULTS

5.3.1 DEVELOPMENT OF MOBILE APPLICATION

A number of proof-of-concept studies were attempted where the strategy was to develop additional hardware attachments to the smartphone[133]. In these attachments, diverse wavelength selection units can be assembled, like light sources at various wavelengths or tunable filters. However, the asynchronous data acquisition at different wavelengths would inevitably cause co-registration error in the data cube and consequently contaminate the analysis outcomes. More importantly, the required investments on these attachments may also pose obstacles on their realistic applications.

In our previous study, we described a strategy to reconstruct multispectral information from skin photographs in RGB format[105]. Before imaging, the RGB camera was calibrated to calculate a transformation matrix (TM) using Wiener estimation algorithm. Then, using the TM, acquired RGB photographs can be reconstructed into multispectral images. Following this strategy, we herein optimized the workflow and developed an app

to implement a multispectral imager on an unmodified smartphone. The app was termed SpeCamX and developed on Android 11 platform (Google, CA). Currently, we installed it on Google Pixel 4 (Google, CA), but any type of smartphone can be used.

SpeCamX is capable of transforming the housed RGB camera into a spectral imager by embedding the multispectral reconstruction algorithm within the app. The whole application consists of four functional fragments, with their interfaces shown in Figure 5.2. The “Imager” fragment (Figure 5.2(a)) is responsible for the setup before imaging. Users can setup the default mode by selecting the model of their smartphones or enter into the customized mode to select the type of color chart for recalibration. Figure 5.2(b) shows the drop-down lists of options in the “Imager” fragment. Figure 5.2c shows the recalibration page. After settings, users can launch the imager by tapping the camera icon in Figure 5.2a. All the recorded datasets can be searched in the “Records” fragment (Figure 5.2(d)). The “MSI” fragment (Figure 5.2(e)) shows the reconstructed spectral images of the subject. Embedded algorithms in SpeCamX processes the spectral data cubes to extract features and present the results in the “Analysis” fragment (Figure 5.2(f)). For example, the “BILI” value represents the prediction made from the ROI in the “Bili” page. Users can acquire these predictions whether in the real-time preview mode or after imaging. Except for BBL, other functions like blood perfusion and pigmentation, can also be accessed in the drop-down menu on the top of the interface. The workflow details of these fragments can be found in the method part of this paper. Overall, five key characteristics guaranteed the compatibility and practicability of SpeCamX in mobile health application: 1) No external attachments or internal modifications to the smartphone are required, thus SpeCamX can be duplicated and used like other normal apps; 2) No further calibration is required when

used in the default mode, but we still opened an entrance for the recalibration to setup a customized mode; 3) The customized recalibration can be simply realized by imaging commercialized standard color charts; 4) No offline operation is required, the imaging, processing and analysis functions are all integrated in this app; 5) Except for the BBL detection, more other functions, like mapping of blood perfusion and pigmentation, are provided as well.

5.3.2 SPECTRAL IMAGING OF COLORCHART, PHANTOM AND SCLERAL TISSUE

The retrieval of spectral information from RGB cameras relies on the TMs we calculated and stored in SpeCamX beforehand. In this part, we conducted an investigation to evaluate the quality of the spectral reconstruction realized by these matrices. In our method, the default TM for Pixel 4 was calculated from 24 Macbeth classic color blocks. First, we applied the stored TM on the *X-rite ColorChecker Digital SG* to reconstruct spectra for both classic colors and skin tones. The comparisons of the standard and reconstructed spectra were shown in Figure 5.9a. The reconstructed spectra highlighted in red match well with the references in both classic and skin tone colors. The RMSE of each color block was measured to quantify the reconstruction accuracy, shown in Supplementary Table 1. The average RMSE of all color blocks is less than 0.04, indicating an accurate reconstruction of reflectance spectra.

RGB values can be affected by different illumination conditions and channel sensitivities, which may lead to inconsistent responses under different camera settings. To address this issue, SpeCamX provided both default TMs and recalibration options to stabilize the quality of spectral imaging. Here, we simulated some extreme conditions by

adjusting the color temperature and ISO of the camera to challenge this stability. *X-rite ColorChecker Digital SG* was again used in this evaluation and imaged under different camera settings. The color temperature was increased from 2500K to 9000K with a step width of 500k.The ISO was set to be 880, 840, 800, 720, 640, 570, 500, 450, 400, 360, 320, 285, 250 and 200, respectively. The RGB values and reflectance spectra of all color blocks in these procedures were recorded by SpeCamX. As an example, the results of color block #7D were shown in Figure 5.9(b, c). The horizontal axis includes both RGB and multispectral imaging (MSI) channels, while the vertical axis represents the change of camera settings. The RGB signals were normalized into the same scale with MSI channels and mapped in the same figure. With the color temperature increased from 2500K to 9000K, we observed the signals in G and B channels remained relatively stable, but that in R channel increased proportionally. In contrast, the SpeCamX provided relatively stable signals in all reconstructed reflectance spectral channels despite the change of the color temperature. A similar result can be observed in Figure 5.9(c), where RGB values are increased with the increase of ISO but the SpeCamX provided consistent spectral reconstruction in all the channels. To quantify the consistency, we calculated the standard deviations of signals in each channel of all color blocks, showing in Figure 5.9(d, e). Compared with RGB values, signals in MSI channels perform much lower standard deviations under different color temperatures and ISOs. These experiments demonstrate that SpeCamX is capable of accurately reconstructing spectral information of subjects with a high consistency under different device conditions and settings.

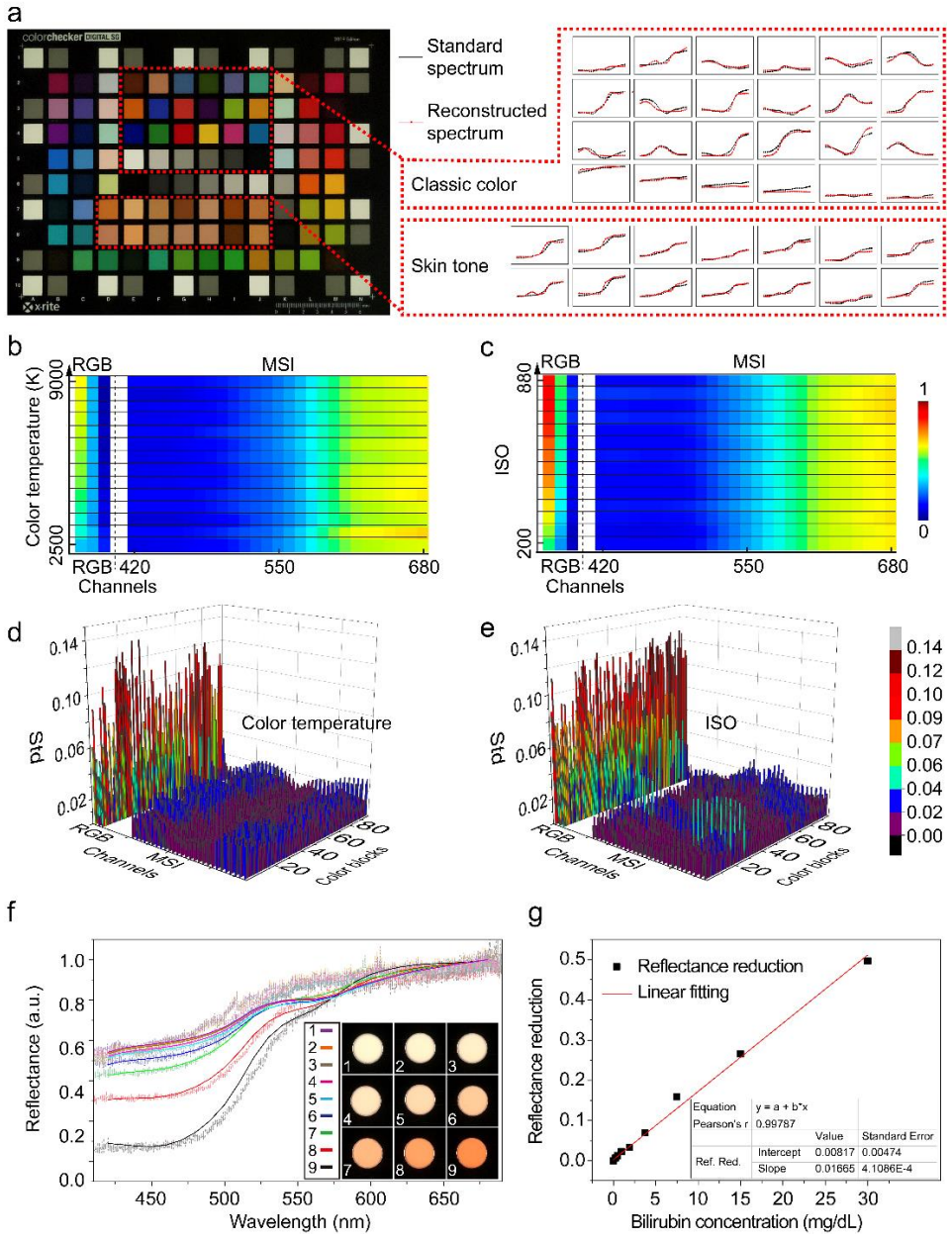

Figure 5. 9. Performance of spectral imaging using SpeCamX.
(a) Spectral reconstruction test on a standard color checker (X-rite ColorChecker Digital SG). The stored TM was applied on the 24 classic colors and also the 14 skin tone colors to estimate the reflectance. The reconstructed spectrums were compared with the standard spectrums in the right. (b, c) Spectral reconstruction of color block #7D under different ISO and color temperature settings. The color temperature is increased from 2500K to 9000K with a step width of 500k. The ISO is set to be 880, 840, 800, 720, 640, 570, 500, 450, 400, 360, 320, 285, 250 and 200. (d, e) Standard deviations of signals in each channel of 96 color blocks with the alternation of color temperature and ISO settings. RGB values of color

block #7D shows much higher standard deviations than the reconstructed spectra in this procedure. (f) Spectral reconstruction test on bilirubin phantoms. The concentrations of bilirubin are 0.00, 0.23, 0.47, 0.94, 1.88, 3.75, 7.50, 15.00, 30.00 mg/dL in phantom 1-9, respectively. The inserted figure shows the RGB photographs of phantoms which show darker and darker yellowish pigmentation from phantom 1 to 9. The curves present the reconstructed reflectance spectra accordingly. The dotted line curves present the reflectance spectra measured by a spectrometer. The reflectance at wavelengths around 460 nm shows gradual decrease from phantom 1 to 9 because of the increased absorption of bilirubin. (g) The linear relationship between the reflectance reduction measured by SpeCamX and the bilirubin concentrations of phantoms. The inserted table shows the fitted equation and fitting errors.

Next, we prepared a set of phantoms to further test the performance of SpeCamX to recover the spectral information of bilirubin. The bilirubin levels are 0.00, 0.23, 0.47, 0.94, 1.88, 3.75, 7.50, 15.00, 30.00 mg/dL in phantoms 1 to 9. The acquired RGB photographs of these phantoms are shown in the inset of Figure 5.9(f), which shows deeper yellowish pigments with the increase of the concentration of bilirubin. Their reflectance spectra were obtained by SpeCamX and presented as the curves in Figure 5.9(f). These spectra were normalized by the reflectance at 680 nm because of the absorbance of bilirubin at this wavelength band is almost negligible. Compared with phantom 1 without bilirubin, other phantoms give lower reflectance around 460 nm and the rate of reduction shows similar to that of their concentrations. We calculated the values of rate reduction at 460 nm and mapped the points with their bilirubin concentrations, accordingly, showing in Figure 5.9(g). There is a linear relationship between these two variables, verifying that SpeCamX can be used to detect and quantify the optical absorption of bilirubin.

Figure 5.10 shows results of SpeCamX-enabled imaging on the sclera of two representative clinical cases. Clinically, BBLs for the participants were measured at 23.4 and 368.9 μmol/L, respectively. From RGB photographs in Figure 5.10(a, b), we can

clearly observe darker yellowish in the sclera of patients with higher BBL. By the side of the photographs, we presented every frame of the spectral images obtained by SpeCamX. In wavebands from 420 to 480 nm, two cases show distinct signal strength differences in the sclera due to different levels of bilirubin concentration. With a further increase of the wavelength, the difference gradually decreases because the absorbance of bilirubin becomes ignorable at longer wavelengths. In red bands above 650 nm, no significant absorption can be observed in both cases. Figure 5.10(c, d) illustrate the generation of the reflectance spectra averaged from two imaging trials. In each trial, we acquired ten snapshots at different regions of the sclera. From each snapshot, we calculated an averaged spectrum from the selected ROI. The final reflectance spectra were then averaged from these ten measurements, showing as the black curves. The reflectance spectra also support our above observation that the sclera tissue of the patient with higher BBL shows lower reflectance in wavebands from 420 to 480 nm.

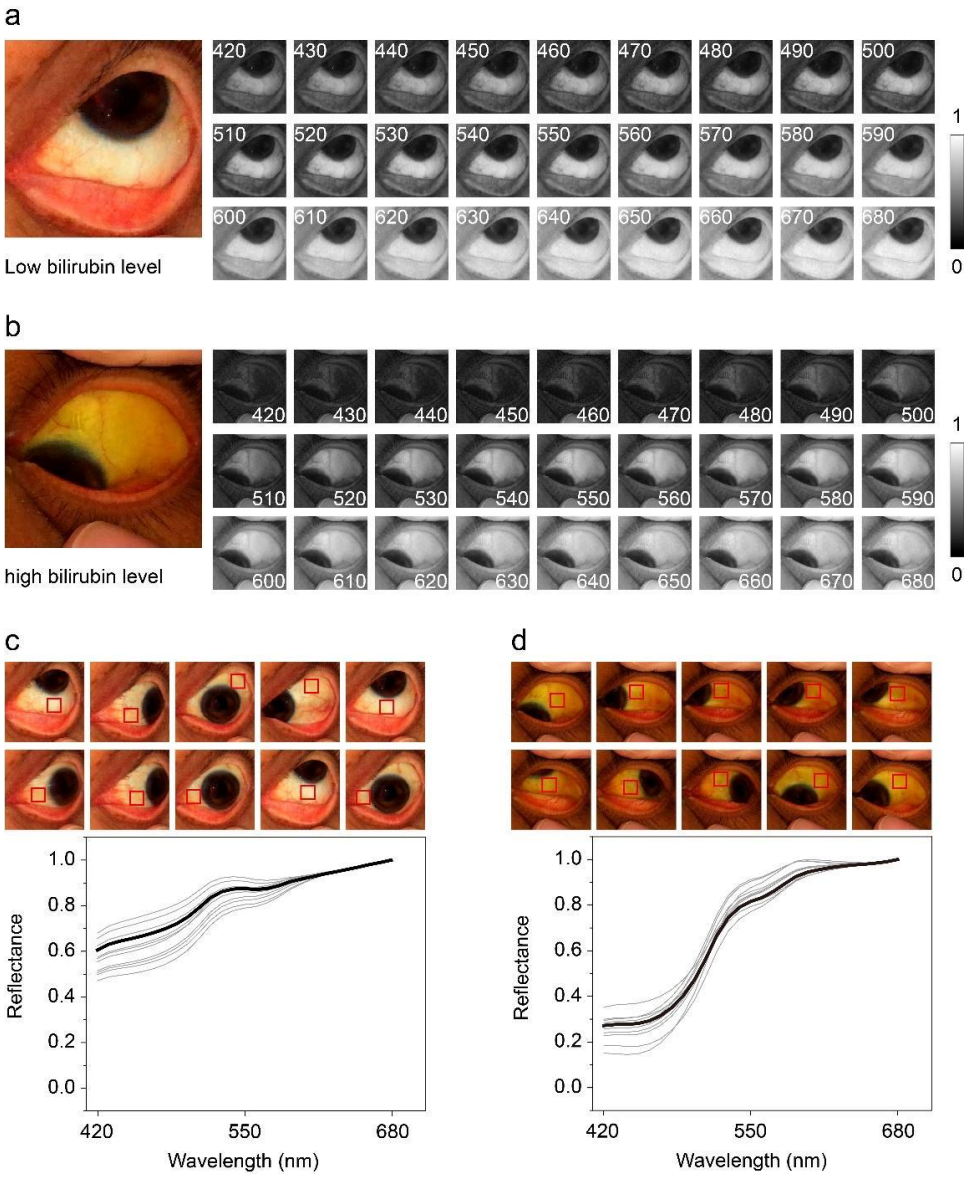

Figure 5. 10. Examples of clinical imaging using SpeCamX.
(a, b) RGB and spectral images of cases with BBLs at 23.4 and 368.9 μmol/L, respectively. (c, d) 10 samplings on different regions of the sclera and the calculation of the reflectance spectrums of cases in (a) and (b), respectively. The case with high BBL shows darker yellowish in the RGB photograph and lower reflectance in wavebands from 420 to 480 nm than the case with low BBLs.

5.3.3 PREDICTION OF BLOOD BILIRUBIN LEVELS WITH MACHINE LEARNING

320 patients with LD were enrolled in our study. The subjects show diversities in the gender, age and diagnosis of disorders (Table 5. 1). RGB photographs and reflectance spectra of

sclera, paired with BBL results obtained from clinical blood testing were included in the data set. As we can observe from Figure 5.10(a, b), except for the yellow pigmentation, the sclera tissue region also shows redness because it is covered by a highly vascularized conjunctiva layer. Considering this multiple-chromophore structure is more complicated than the bilirubin phantom, we chose to use machine learning algorithms to predict BBL instead of using linear regression algorithms. Besides, to validate our assumption that SpeCamX can better predict the BBL, we developed machine learning models respectively trained with spectra and RGB signals to compare their prediction qualities. ANN, SVM, KNN and RF algorithms were used in the training of regression models. To avoid overfitting, the prediction of each group was obtained by 10-fold cross-validation. 320 cases were randomly split into 10 sets. In each round, the model was trained using 9 of 10 sets, and then tested on the remaining one set. In 10 rounds, every data set needed to be tested for once. The final prediction was averaged from predictions of 10 rounds.

Table 5. 1. Diagnosis profile of subjects in clinical assessment

Table 1 Diagnosis profile of subjects in clinical assessment

Gender	Number		Disorder	Number	Disorder	Number
Male	189		Viral Hepatitis	53	Primary biliary cholangitis	6
Female	131		Drug-induced liver injury	30	Alcohol-induce liver injury	6
			Alcoholic cirrhosis	26	Acute liver failure	4
Age	**Number**		Acute-on-chronic liver failure	24	Other diseases	59
20-29	10		Hepatitis B	19	Multiple liver diseases	29
30-39	32		Primary carcinoma of the liver	17		
40-49	92		Acute pancreatitis	15		
50-59	94		Drug-induced liver cirrhosis	11		
60-69	69		Cirrhosis	8		
70-79	19		Subacute liver failure	7		
80-89	4		Primary biliary cirrhosis	6		

Figure 5.11. (a1) shows the predictions obtained by ANN-based regression models. In 320 cases, we realized CC at ~0.90 and ~0.83 with SAL and RGBL models, respectively. Except for higher CC, the SAL prediction band (red band) is also narrower than the RGBL prediction band (black band), indicating smaller prediction errors. From the Bland-Altman

plots (Figure 5.11(b1)), we can also observe smaller prediction errors and bias in SAL prediction. Given more exposed features with higher spectral resolution, the SAL model is also supposed to learn quicker than the RGBL model. To validate this point, we reduced the data feeding to test and compare the prediction performance as well. Figure 5.11(a2-4) show the prediction results while the subjects were reduced by randomly resampling 75%, 50%, 25% of the whole 320 cases, respectively. The prediction bands of both SAL and RGBL widened when the data set size was decreased. However, the SAL prediction band kept its relative stability from the intense expansion that happened in the RGBL prediction band. This observation was quantifiably verified in their corresponding Bland-Altman plots (Figure 5.11(b2-4)). The limits of agreement (LOA) of SAL prediction changed from +122.71/-124.43 μmol/L to +149.66/-157.26 μmol/L while the case number decreases from 320 to 80, but the LOA of RGBL expanded from +161.28/-171.10 μmol/L to +236.29/-234.65 μmol/L. This difference indicates that SpeCamX-enabled SAL can achieve predictions with higher quality than RGBL when the data feeding is limited.

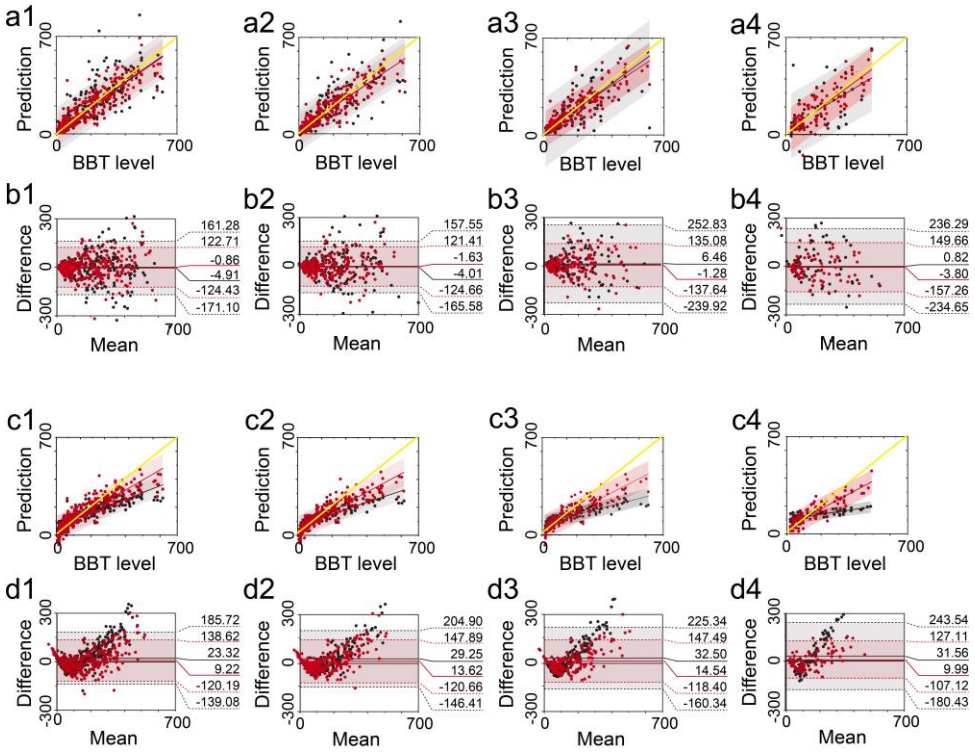

Figure 5. 11. Comparison of prediction performance between SAL and RGBL using ANN and SVM.
(a, c) the relationship between BBL and predictions with SAL/RGBL using ANN and SVM, respectively. Black point: RGBL prediction; red point: SAL prediction; black area: 95% prediction band of RGBL prediction; red area: 95% prediction band of SAL prediction. (b, d) Bland-Altman plots of predictions with SAL and RGBL using ANN and SVM, respectively. Black dotted line: 1.96 limits of agreement of RGBL prediction; red dotted line: 1.96 limits of agreement of SAL prediction; black line: mean difference (MD) of RGBL prediction; red line: MD of SAL prediction. 1-4 represents different resampling percentages: 1:100%; 2:75%; 3:50%; 4: 25%. All the groups with different sample sizes are randomly selected from the data pool of 320 patients. Units for all values are μmol/L.

In the results of SVM-based regression models (Figure 5.11(c1)), the regression coefficient of SAL is significantly closer to 1 than that of RGBL, indicating SAL prediction is less biased. This observation has been validated by the Bland-Altman plots in Figure 5.11(d1), where SAL produces much smaller bias (9.22) than RGBL (23.32). Except for bias, the prediction error is also smaller in SAL. While less data was fed, SAL prediction

shows relative stability in both error and bias. However, these two indexes of RGBL prediction increased by ~35% and ~30%, respectively.

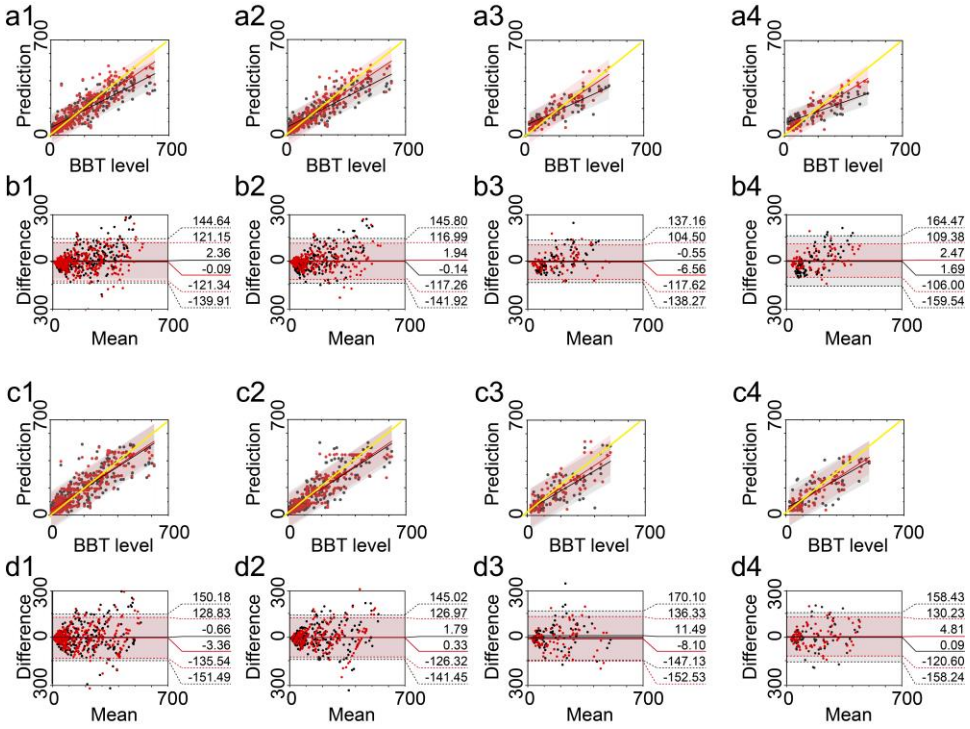

Figure 5. 12. Comparison of prediction performance between SAL and RGBL using KNN and RF.
(a, c) the relationship between BBL and predictions with SAL/RGBL using ANN and SVM, respectively. Black point: RGBL prediction; red point: SAL prediction; black area: 95% prediction band of RGBL prediction; red area: 95% prediction band of SAL prediction. (b, d) Bland-Altman plots of predictions with SAL and RGBL using KNN and RF, respectively. Black dotted line: 1.96 limits of agreement of RGBL prediction; red dotted line: 1.96 limits of agreement of SAL prediction; black line: mean difference (MD) of RGBL prediction; red line: MD of SAL prediction. 1-4 represents different resampling percentages: 1:100%; 2:75%; 3:50%; 4: 25%. All the groups with different sample sizes are randomly selected from the data pool of 320 patients. Units for all values are μmol/L.

Except for ANN and SVM, we also compared the SAL and RGBL predictions using KNN and RF algorithms (Figure 5.12). In summary of these comparisons, SAL improves the prediction quality in varying degrees, especially with less data feeding. To illustrate this point more straightforwardly, we quantified the prediction performance of SAL and

RGBL with data resampling percentage changing from 12.5% to 100% with a step width at 12.5%. The CC, MD and STD were then measured and presented as curves in Figure 5.12. The evolution curves showed that the CC of SAL always remained in high levels at ~0.9, even when only 12.5% of the data was used to train the model. On the contrary, the CC of RGBL can be even lower than 0.6. In all methods except for SVM, the prediction biases of SAL are close to 0, smaller or at least comparable to RGBL predictions. In SVM, the bias of SAL is unneglectable, but also 50% smaller than that of RGBL. The prediction errors of SAL slightly increase with smaller sample size but overall lower than 75 μmol/L, which is almost the best level the RGBL can reach. It is worth noting that our study shows that the prediction error increases along the range of BBL (Figure 5.13). In a similar range, our SpeCamX-enabled SAL provided smaller or at least comparable prediction errors to conventional methods.

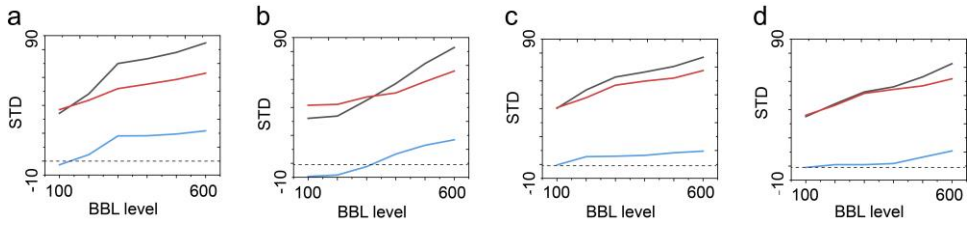

Figure 5. 13. STD of predictions using RGBL and SAL in different BBL ranges.
(a), ANN; (b), SVM; (c), KNN; (d), RF. Black curve: RGBL prediction; red curve: SAL prediction; blue curve: difference between RGBL prediction and SAL prediction. While the BBL range increased, the prediction error showed overall increase in both methods, but slower in SAL. In the range from 0 to 600 μmol/L, the STD of SAL-based prediction can be smaller than 70 μmol/L. In the range from 0 to 350 μmol/L, the STD of SAL-based prediction can be controlled around 50 μmol/L, smaller or comparable to conventional methods.

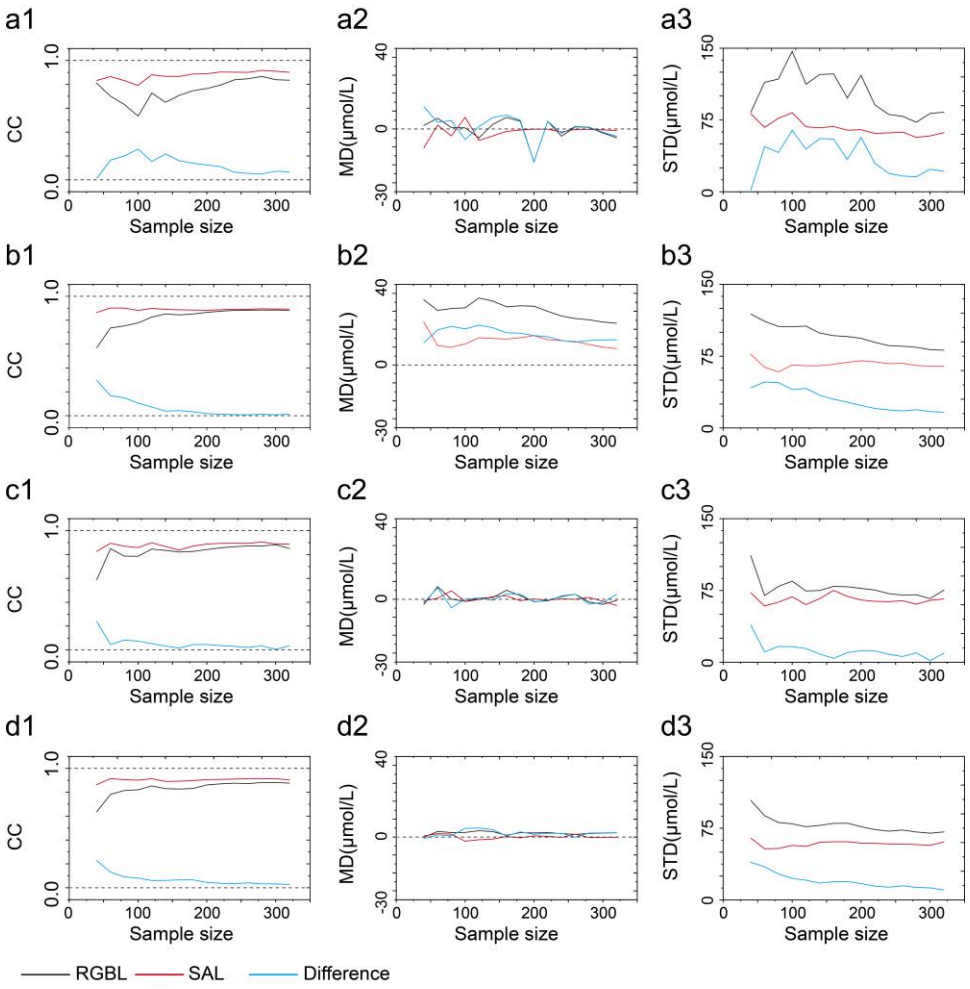

Figure 5. 14. Quantification of improvements of SAL prediction in different sample sizes and learning algorithms compared with RGBL prediction. 1, CC, 2, Mean difference (MD), and 3, STD between BBLs and prediction with SAL/RGBL along different resampling percentages from 12.5% to 100%. a, ANN; b, SVM; c, KNN; d, RF. Black curve: RGBL prediction; red curve: SAL prediction; blue curve: difference between RGBL prediction and SAL prediction.

Besides the enhancements exist in absolute values, the red SAL curves in Figure 5.14 seem to perform higher stability in all groups than RGBL curves. We quantified the standard deviations of these four indexes in all groups with different sample sizes and algorithms (Figure 5.15). The standard deviations of CC, MD, and STD in RGBL prediction are 259%, 102% and 192% higher than those in SAL prediction.

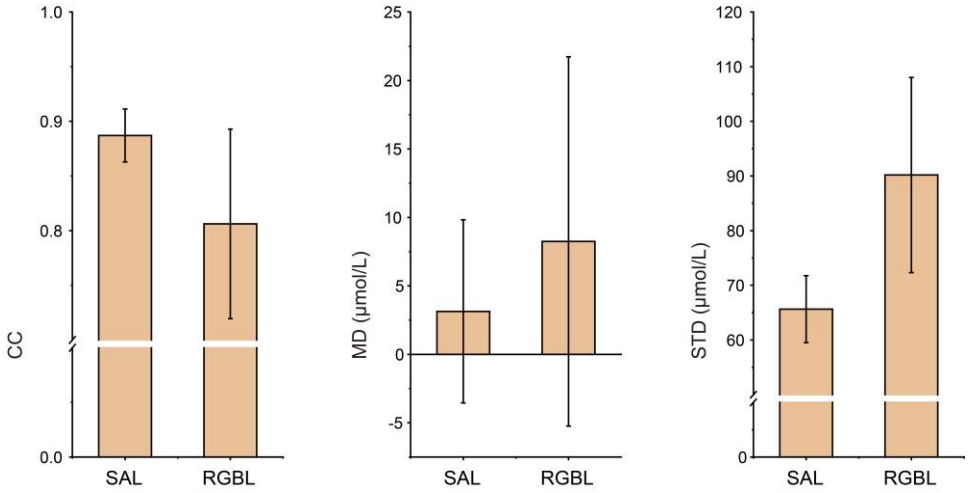

Figure 5. 15. Bar graphs of prediction qualities in all groups with different sample sizes and algorithms using RGBL and SAL.
SAL-based predictions realized smaller STD than RGBL in CC, MD and STD.

These comparison results demonstrated that SpeCamX-enabled SAL learns better than RGBL in accuracy, efficiency and stability. We incorporated four models trained with the whole data set into the "Analysis" fragment of the app, the predictions using these models would be averaged and previewed as the "BILI" value by the side of ROI. In this case, the SpeCamX-augmented smartphone bilirubinometer can be used as an integrated and real-time BBL detector. We showed the predictions of SAL/RGBL using the combined machine learning model in Figure 5.16. Being similar to predictions using the single machine learning model, the predictions of combined model also validated that SAL is better than RGBL in prediction accuracy, stability and learning efficiency. Besides, the combined SAL achieved higher or at least comparable prediction quality than using the single model. In all groups, the STD was controlled to be around 60 μmol/L and the CC/AUROC values were all stabilized above 0.9.

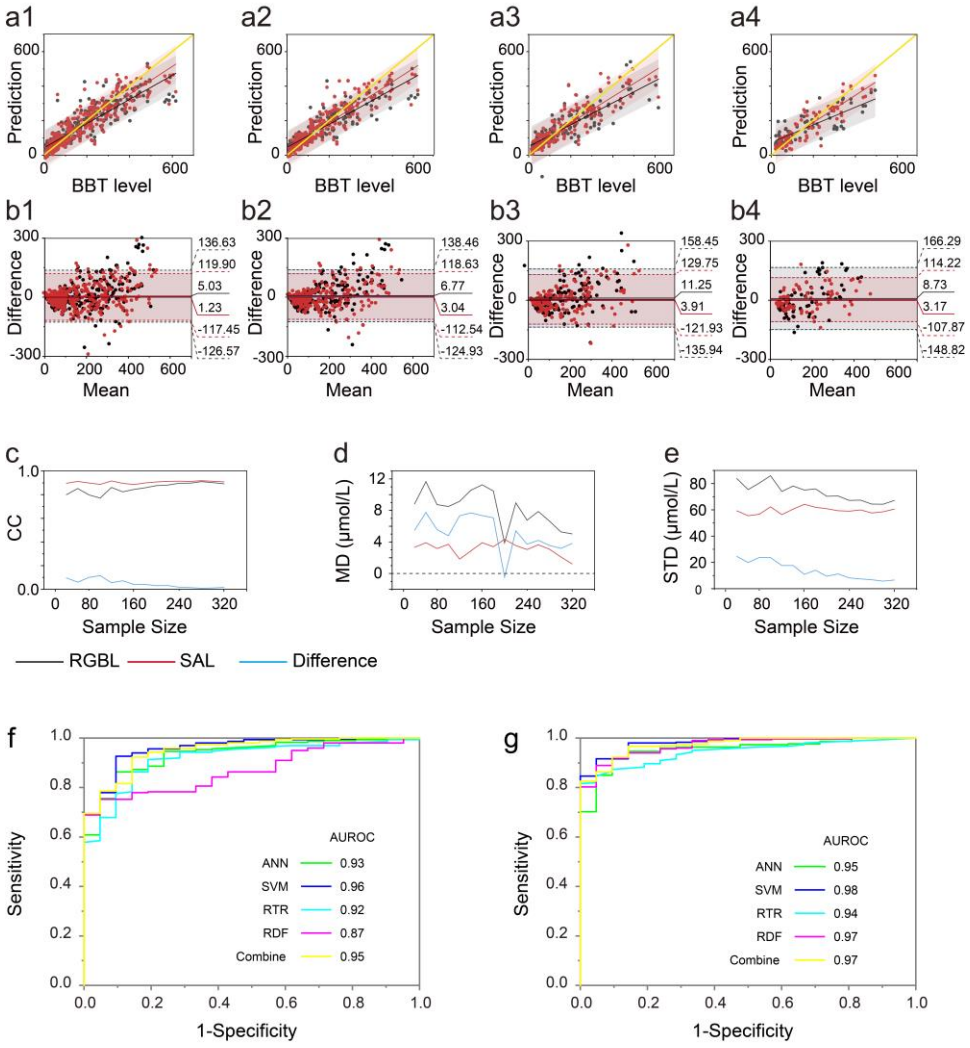

Figure 5. 16. Quantification of improvements of SAL prediction using the combined machine model.

(a) the relationship between BBL and predictions with SAL/RGBL using the combined machine learning model. Black point: RGBL prediction; red point: SAL prediction; black area: 95% prediction band of RGBL prediction; red area: 95% prediction band of SAL prediction. (b) Bland-Altman plots of predictions with SAL and RGBL using the combined machine learning model. Black dotted line: 1.96 limits of agreement of RGBL prediction; red dotted line: 1.96 limits of agreement of SAL prediction; black line: MD of RGBL prediction; red line: MD of SAL prediction. 1-4 represents different resampling percentages: 1:100%; 2:75%; 3:50%; 4: 25%. (c) CC, (d) MD and (e) STD between BBLs and prediction with SAL/RGBL using the combined machine learning model along different resampling percentages from 12.5% to 100%. Black curve: RGBL prediction; red curve: SAL prediction; blue curve: difference between RGBL prediction and SAL prediction. (f, g) the receiver-operating characteristic (ROC) analysis of prediction with RGBL (f) and SAL (g) using the single and combined

machine learning model. Whether in single or combined models, SAL achieves a bigger area under the ROC curve (AUROC) than RGBL, which indicates a better diagnostic. All the groups with different sample sizes are randomly selected from the data pool of 320 patients. Units for all values in a, b, d and e are μmol/L.

5.4 DISCUSSION AND CONCLUSION

The development of mobile health enables daily monitoring of many vital signs and components, some of them have the potential to indicate diseases which can rarely be detected out of clinics[6]. Exploring and developing relative techniques can promote the public healthcare. For example, the global incidence of LD is estimated at 1.5 billion, which leads to about 2 million deaths each year[134]. Close monitoring of at-risk populations is believed to be an effective strategy to control its spread and development[135]. However, frequent clinical testing imposes an inevitable burden to the patients, both psychologically and economically, impacting the compliance to seek for medical services. To improve the clinical compliance and promote their willingness to accept the monitoring of liver health conditions, one solution is to noninvasively detect bilirubin levels in the serum, preferably that can be performed in a non-clinical environment. The balance of BBL in the circulation relies on a normal liver metabolism, which makes it a suitable biomarker of liver functions[136]. At different severity stages of LD, bilirubin dysbolism accumulates and eventually causes different levels of hyperbilirubinemia, which usually appears as the yellowish pigmentation in body tissue[137]. With distinct spectral properties, bilirubin-induced pigmentation is suitable to be noninvasively measured using optical sensors to estimate the BBL and finally predict the live condition. Some of these sensors, like transcutaneous bilirubinometer, equip spectral illumination for the detection of the light absorption to estimate BBL[138].

Actually, there are already some portable versions of these sensors that can save people from the frequent clinical visits[139], however, substantial investment is still required to acquire these specially-made devices, which eventually prevents their wider spread use.

Herein, we provided a strategy by developing a mobile application termed SpeCamX to transform smartphones into spectral imagers and tested this strategy in BBL prediction. SpeCamX is capable of acquiring multispectral data cubes though a single snapshot without external attachments. Besides, SpeCamX provides a set of pre-loaded TMs for some popular smartphones and standard room conditions. This provision would save users from the requirements on the expertise of complicated color calibration and off-line processing. Moreover, after spectral imaging, we inserted the “Analysis” fragment in the app to analyze the chromophore information from acquired multispectral data cubes. Except for the bilirubin prediction discussed in this study, we also provide entrances to map the blood perfusion, melanin pigmentation and other chromophores within human tissue. Given that smartphones are already integrated terminals equipped with detector, processor and display units, the installation of SpeCamX will enable them to conduct medical screening and diagnosis with a high independence and exempted expense.

In this study, as a proof of concept, the output data cube of SpeCamX was set to be in 27 channels and range from 420 to 680 nm with a step width at 10 nm. We assumed that bilirubin and hemoglobin dominated the color of scleral tissue, thus the selected wavelength bands covered both the absorption peaks and troughs of these two chromophores. Moreover, the format of output data, including the spectral resolution and channel number, is tunable according to different sample compositions and processing methods. For instance, we are capable of setting up denser channels around bilirubin’s

absorption peak if the hemoglobin was excluded. While using machine learning algorithms, we prefer to provide data with more channels and higher spectral resolutions so the potential features can be fully learned. Except for that, SpeCamX can also support non-learning algorithms by imaging at typical wavelengths, like 460 and 500 nm used in transcutaneous bilirubinometer. Overall, SpeCamX-enabled medical imaging shows a high technical flexibility and a large optimization space.

Through the clinical imaging to patients with LD, we demonstrated the enhancements on predictions realized by SpeCamX. Encouraged by this study, we believe SpeCamX may also act as an effective tool to monitor other bilirubin-related diseases, like neonatal jaundice. In fact, both infants and the guardians should benefit from the real-time, non-contact and non-invasive evaluation mode of this SpeCamX-augmented smartphone bilirubinometer. Further, if we see the bilirubin prediction described here as an evidence, it should be reasonable to expect similar prediction quality when evaluating other chromophores. For example, SpeCamX should conceivably better describe hemoglobin behaviors than regular camera apps, which would strengthen the monitoring of blood and vascular abnormalities. In a word, SpeCamX has the potential to get involved in conventional smartphone-enabled medical imaging methods and improve their performance.

There are still some limitations in our study. Although we maintained the diversity of patients in gender and ages, only Asian patients were enrolled and imaged. Being dominated by bilirubin and hemoglobin, the color of scleral tissue is supposed to be uncorrelated with the pigments varied in different complexions, but further investigation is needed. Besides this, the property of SpeCamX to estimate targets from more complicated

backgrounds still remains untested. Some human tissues may contain chromophores with more diversity and less predictability. Aiming to spread the usage of SpeCamX, we need to further explore its usability in these scenes.

Looking forward, though our current study was conducted in clinics, a wider application of SpeCamX is expected to be realized by the public in their daily lives. In the future, we will keep working on the optimization, package and approval of this app and method to provide their open access. Through this way, we may conduct studies on the health care of a larger population with more diversity in regions, races, complexions and diagnosis. Meanwhile, we will keep updating the embedded “Analysis” fragment by uploading more functions to empower this platform for the screening and monitoring of more health issues.

Chapter 6. SUMMARY AND FUTURE WORK

In this thesis, the development and applications of typical augmented smartphone-enabled imaging in mobile health are comprehensively presented and discussed. The systems and methods of smartphone-enabled multispectral imaging, fluorescence imaging and remote photoplethysmography are designed and developed. Considering their performance in mapping hemoglobin, melanin, bilirubin, oxygenation and blood pulsations within human tissue, this set of techniques possess a great potential in augmenting imaging from afar in mHealth.

We propose a novel method and system that utilizes popular smartphone to realize multispectral imaging for analyzing skin morphological features and monitoring hemodynamics. The imaging system works based on built-in RGB camera and flashlight in the smartphone. We apply Wiener estimation to transform the acquired RGB-mode images into “pseudo”-multispectral images with 16 wavebands, covering a visible range from 470nm to 620nm. The processing method uses weighted subtractions between wavebands to extract absorption information caused by specific chromophores within skin tissue, mainly including hemoglobin and melanin. Based on the extracted absorption information of hemoglobin, we conduct real-time monitoring experiments in the skin to measure heart rate and to observe skin activities during a vascular occlusion event. Compared with expensive multispectral imaging systems, the smartphone-based system delivers similar results but with very-high imaging resolution. Besides, it is easy to operate, very cost effective and has a wider customer base. The use of an unmodified smartphone to realize multispectral imaging promises a possibility to bring multispectral analysis of

skin out from laboratory and clinical wards to daily life, which may also impact on healthcare in low resource settings and rural areas.

We propose a smartphone-enabled system and method to realize multispectral autofluorescence imaging for analyzing bacterial infection within skin and oral cavity. The system consists of an unmodified and intact commercial smartphone and a home-made cell phone case with built-in black light LEDs. We use Wiener estimation method to calibrate the RGB-mode smartphone camera and transform the acquired autofluorescence photographs into pseudo-multispectral data cubes with 15 wavebands ranging from 420 nm to 700 nm. Then, we extract and compare the spectral performance of emissions from bacteria-produced porphyrins and endogenous background tissue. Based on the extracted autofluorescence spectra, we apply weighted subtraction between wavebands of interest to realize bacteria targeting and feature mapping. We conduct analysis of autofluorescence on facial skin and dental plaques to demonstrate the performance of the proposed system and methods. Further, with this strategy, we realize quantitative analysis of the bacterial infection in the combination and oily types of skin. Compared to traditional bacteria assessment strategies, we provide a method with the features of real-time visualization, label-free molecular identification, and feature mapping. Meanwhile, differing from the most conventional multispectral imaging systems, the proposed smartphone-based system works in a snapshot mode, thus improving its immunity to motion artifacts. Considering the popularity of smartphones in today's world, it is expected a relatively easy acceptance of the proposed cost-effective method by the community, making an impact on skin and oral care in general and in rural areas with low resource settings in particular.

We propose a smartphone-enabled remote multispectral photoplethysmography (SP-rmPPG) system and method to realize spatiotemporal monitoring of perfusion changes and pulsations of the oxyhemoglobin and deoxyhemoglobin information of the effective blood volume within light interrogated skin tissue beds. The system is implemented on an unmodified smartphone utilizing its built-in camera and flashlight to acquire videos of the skin reflectance. The SP-rmPPG method converts the RGB video into multispectral cubes, upon which to decouple the dynamic changes in oxyhemoglobin and deoxyhemoglobin information using a modified Beer-Lambert law and the selective wavelength bands of 500nm and 650nm. Blood pulsation amplitudes are then obtained by applying a window-based lock-in amplification on the derived spatiotemporal changes in oxyhemoglobin or deoxyhemoglobin signals. To demonstrate the feasibility of proposed method, we conduct two experiments on the skin tissue beds that are conditioned by occlusive maneuver of supplying arteries: one using the popular blood cuff pressure maneuver on the upper arm, and another artificially inducing a transient ischemic condition on the facial skin tissue beds by finger pressing on the supplying external carotid artery. The cuff experiment shows that the measured dynamic information of oxyhemoglobin and deoxyhemoglobin in the downstream agrees well with the parallel measurements of oxygenation saturation given by the standard pulse oximeter. We also observe the expected imbalance of spatiotemporal changes in the oxyhemoglobin and deoxyhemoglobin between the right and left cheeks when the transient ischemic condition is induced in the one side of facial skin tissue beds. The results from the two experiments sufficiently demonstrate the feasibility of the proposed method to monitor the spatiotemporal changes in the skin hemodynamics, including blood oxygenation and pulsation amplitudes. Considering the ever-growing

accessibility and affordability of the smartphone to the general public, the proposed strategy promises the early screening of vascular diseases and improving general public health particularly in rural areas with low resource settings.

Lastly, we developed a mobile app termed SpeCamX that can transform smartphones into multispectral imagers. With this app, we implemented an augmented smartphone bilirubinometer to predict BBL in an accurate, low-cost and easy-to-use manner. We described the development of SpeCamX and validated its performance in capturing multispectral information. In clinical study, we imaged the sclera of 320 LD patients with this augmented smartphone bilirubinometer. With the acquired multispectral data cubes paired with total serum bilirubin (TSB) results from blood testing, we trained machine learning models to predict BBL and realized correlation coefficients (CC) above 0.9 between two measurements. Moreover, we compared this SpeCamX-enabled spectrally augmented learning (SAL) with the learning based on RGB photographs (RGBL) in four typical algorithms, including artificial neural network (ANN), support vector machine (SVM), K-nearest neighbors (KNN) and random forest (RF). Experimental results verified the superiority of SAL in prediction bias, errors and stabilities, especially with reduced data feeding. The results support our claim that SpeCamX-enabled smartphone multispectral imager can better capture spectral information to improve the prediction of bio-chromophores, like bilirubin. More importantly, our imaging and prediction can be conducted without additional investments and expertise, implying a high utility to provide healthcare for publics, especially for populations in the shortage of medical resources.

Above development on the smartphone-enabled imaging provides a new strategy by exposing more information than conventional smartphone RGB vision. Besides, no

modification would be required, except for the external light source for fluorescence excitation, for smartphone to derive these vital signs and biometric features. In other words, these functions are added on the original imaging modality without disturbing or replacing it, which is what we claimed “augmented” smartphone-enabled imaging. For the imaging from afar aspect in mHealth, this strategy has the potential to significantly strengthen its capacity in delivering trustable information for diagnosis.

Though the potential has been revealed in this thesis, some further work on the augmented smartphone-enabled imaging is worth exploring. In Chapter 2, the multispectral reconstruction method based on Wiener estimation algorithm has been proposed. However, the reconstruction accuracy has only been tested with the standard color chart. Concerning the difference of spectral property between human tissue and color chart, further investigation on the reconstruction quality and optimization is necessary. Besides, the chromophore extraction model used in Chapter 2 is in a highly simplified form. The scattering property of tissue has been ignored for the convenience of calculation. However, practically, human skin is a high scattering tissue with very complicated structures and components. Further work will be required to address these issue to improve the function of proposed method from “contrasting” to accurate quantification. In Chapter 4 and 5, the oximeter and blood test results had been used as the reference and golden standard to assess the quality of corresponding smartphone imaging. However, this validation step has not been provided in the estimation of cutaneous hemoglobin, pigmentation and porphyrins in Chapter 2 and 3 because of the complexity of golden standard testing to these components. Our future work will also focus on validating these estimations with clinical standard to further support and enhance the augmented smartphone imaging methods. In Chapter 5,

the usefulness and advantages of smartphone-enabled multispectral imaging in clinics have been verified by predicting blood bilirubin levels of patients with liver diseases. However, some details in the imaging procedure are also worth exploring as well. For example, some previous studies have discussed the impact of ambient light on the measurement [140], which is also a key factor that might challenge our calibration step in the multispectral reconstruction. In this case, further exploration on the illumination conditions, including the ambient light, illumination evenness, imaging distance and angles, would provide useful technical supports and backups for the practical application of augmented smartphone imaging methods. Except for the mentioned imaging modalities, the package and development of related mobile applications also needs to be addressed to provide service for the public. Besides, to keep empowering this strategy, it is necessary to explore the implementation of other imaging modalities, such as polarization imaging and 3D imaging, on the smartphone platform. Finally, as a branch of mHealth techniques, the communication and cross-validation between smartphone-enabled imaging from afar and other techniques, like wearable devices, are also worth exploring, especially when the purpose is to monitor hemodynamics.

BIBLIOGRAPHY

1. S. T.-B. Hamida, B. Ahmed, D. Cvetkovic, E. Jovanov, G. Kennedy, and T. Penzel, "A new era in sleep monitoring: the application of mobile technologies in insomnia diagnosis," in *Mobile Health* (Springer, 2015), pp. 101-127.
2. S. Adibi, *mHealth multidisciplinary verticals* (CRC Press, 2014).
3. O. World Health, *The world health report 2006: working together for health* (World Health Organization, 2006).
4. Y. Kinfu, M. R. Dal Poz, H. Mercer, and D. B. Evans, "The health worker shortage in Africa: are enough physicians and nurses being trained?," (SciELO Public Health, 2009).
5. N. Mansor, H. Awang, N. F. A. Rashid, D. Gu, and M. Dupre, "Malaysia ageing and retirement survey," Encyclopedia of gerontology and population aging, 1-5 (2019).
6. S. R. Steinhubl, E. D. Muse, and E. J. Topol, "The emerging field of mobile health," Science translational medicine **7**, 283rv283-283rv283 (2015).
7. S. Sukreep, K. Elgazzar, H. Chu, P. Mongkolnam, and C. Nukoolkit, "iWatch: a fall and activity recognition system using smart devices," Int J Comp Commun Eng **8**, 18-31 (2019).
8. M. Ringeval, G. Wagner, J. Denford, G. Paré, and S. Kitsiou, "Fitbit-based interventions for healthy lifestyle outcomes: systematic review and meta-analysis," Journal of medical Internet research **22**, e23954 (2020).

9. J. Barczik and Y. C. Serpanos, "Accuracy of smartphone self-hearing test applications across frequencies and earphone styles in adults," American journal of audiology **27**, 570-580 (2018).

10. Y.-C. Wu, P.-F. Chen, Z.-H. Hu, C.-H. Chang, G.-C. Lee, and W.-C. Yu, "A mobile health monitoring system using RFID ring-type pulse sensor," in (IEEE, 317-322.

11. E. K. Sackmann, A. L. Fulton, and D. J. Beebe, "The present and future role of microfluidics in biomedical research," Nature **507**, 181-189 (2014).

12. S. A. Boppart and R. Richards-Kortum, "Point-of-care and point-of-procedure optical imaging technologies for primary care and global health," Science translational medicine **6**, 253rv252-253rv252 (2014).

13. L. M. Abbott, R. S. Magnusson, E. Gibbs, and S. D. Smith, "Smartphone use in dermatology for clinical photography and consultation: Current practice and the law," Australasian Journal of Dermatology **59**, 101-107 (2018).

14. K. M. Rappaport, C. C. McCracken, J. Beniflah, W. K. Little, D. A. Fletcher, W. A. Lam, and A. L. Shane, "Assessment of a smartphone otoscope device for the diagnosis and management of otitis media," Clinical pediatrics **55**, 800-810 (2016).

15. M. E. Giardini, I. A. T. Livingstone, S. Jordan, N. M. Bolster, T. Peto, M. Burton, and A. Bastawrous, "A smartphone based ophthalmoscope," in (IEEE, 2177-2180.

16. J. K. Bae, A. Vavilin, J. S. You, H. Kim, S. Y. Ryu, J. H. Jang, and W. Jung, "Smartphone-based endoscope system for advanced point-of-care diagnostics: feasibility study," JMIR mHealth and uHealth **5**, e7232 (2017).

17. C. M. Perera and R. Chakrabarti, "A review of m-health in medical imaging," Telemedicine and e-Health **21**, 132-137 (2015).

18. S. Kroemer, J. Frühauf, T. M. Campbell, C. Massone, G. Schwantzer, H. P. Soyer, and R. Hofmann-Wellenhof, "Mobile teledermatology for skin tumour screening: diagnostic accuracy of clinical and dermoscopic image tele-evaluation using cellular phones," British Journal of Dermatology **164**, 973-979 (2011).

19. H. Engel, J. J. Huang, C. K. Tsao, C. Y. Lin, P. Y. Chou, E. M. Brey, S. L. Henry, and M. H. Cheng, "Remote real-time monitoring of free flaps via smartphone photography and 3G wireless Internet: A prospective study evidencing diagnostic accuracy," Microsurgery **31**, 589-595 (2011).

20. A. Sharma, S. D. Subramaniam, K. I. Ramachandran, C. Lakshmikanthan, S. Krishna, and S. K. Sundaramoorthy, "Smartphone-based fundus camera device (MII Ret Cam) and technique with ability to image peripheral retina," European journal of ophthalmology **26**, 142-144 (2016).

21. G. Bearman and R. Levenson, "Biological imaging spectroscopy," Biomedical photonics handbook, 1-25 (2003).

22. V. G. Bondur, "Modern approaches to processing large hyperspectral and multispectral aerospace data flows," Izvestiya, Atmospheric and Oceanic Physics **50**, 840-852 (2014).

23. P. Curran, "Multispectral remote sensing of vegetation amount," Progress in physical geography **4**, 315-341 (1980).

24. R. M. Levenson and J. R. Mansfield, "Multispectral imaging in biology and medicine: slices of life," Cytometry Part A: the journal of the International Society for Analytical Cytology **69**, 748-758 (2006).

25. I. Diebele, I. Kuzmina, A. Lihachev, J. Kapostinsh, A. Derjabo, L. Valeine, and J. Spigulis, "Clinical evaluation of melanomas and common nevi by spectral imaging," Biomedical optics express **3**, 467-472 (2012).

26. V. Lukinsone, I. Kuzmina, R. Veilande, E. V. Plorina, D. Bliznuks, K. Bolochko, A. Derjabo, I. Lihacova, and J. Spigulis, "Multispectral and autofluorescence RGB imaging for skin cancer diagnostics," in (SPIE, 54-60.

27. R. Shogenji, Y. Kitamura, K. Yamada, S. Miyatake, and J. Tanida, "Bimodal fingerprint capturing system based on compound-eye imaging module," Applied Optics **43**, 1355-1359 (2004).

28. A. A. Wagadarikar, N. P. Pitsianis, X. Sun, and D. J. Brady, "Video rate spectral imaging using a coded aperture snapshot spectral imager," Optics express **17**, 6368-6388 (2009).

29. L. Gao, R. T. Smith, and T. S. Tkaczyk, "Snapshot hyperspectral retinal camera with the Image Mapping Spectrometer (IMS)," Biomedical optics express **3**, 48-54 (2012).

30. D. Evanko, "Focus on fluorescence imaging," Nature Methods **2**, 901-902 (2005).

31. W. Zhong, "Nanomaterials in fluorescence-based biosensing," Analytical and Bioanalytical Chemistry **394**, 47-59 (2009).

32. C. Grienberger and A. Konnerth, "Imaging calcium in neurons," Neuron **73**, 862-885 (2012).

33. L. A. Yannuzzi, K. T. Rohrer, L. J. Tindel, R. S. Sobel, M. A. Costanza, W. Shields, and E. Zang, "Fluorescein angiography complication survey," Ophthalmology **93**, 611-617 (1986).

34. L.-M. W. K. Song, S. Banerjee, D. Desilets, D. L. Diehl, F. A. Farraye, V. Kaul, S. R. Kethu, R. S. Kwon, P. Mamula, and M. C. Pedrosa, "Autofluorescence imaging," Gastrointestinal endoscopy **73**, 647-650 (2011).

35. G. A. Wagnieres, W. M. Star, and B. C. Wilson, "In vivo fluorescence spectroscopy and imaging for oncological applications," Photochemistry and photobiology **68**, 603 (1998).

36. M. Larsson, R. Favilla, and T. Strömberg, "Assessment of advanced glycated end product accumulation in skin using auto fluorescence multispectral imaging," Computers in Biology and Medicine **85**, 106-111 (2017).

37. M. Y. Rennie, D. Dunham, L. Lindvere-Teene, R. Raizman, R. Hill, and R. Linden, "Understanding real-time fluorescence signals from bacteria and wound tissues observed with the MolecuLight i: XTM," Diagnostics **9**, 22 (2019).

38. J. Allen, "Photoplethysmography and its application in clinical physiological measurement," Physiological measurement **28**, R1 (2007).

39. A. A. R. Kamal, J. B. Harness, G. Irving, and A. J. Mearns, "Skin photoplethysmography—a review," Computer methods and programs in biomedicine **28**, 257-269 (1989).

40. R. Sinhal, K. Singh, and M. M. Raghuwanshi, "An overview of remote photoplethysmography methods for vital sign monitoring," Computer Vision and Machine Intelligence in Medical Image Analysis, 21-31 (2020).

41. P.-W. Huang, B.-J. Wu, and B.-F. Wu, "A heart rate monitoring framework for real-world drivers using remote photoplethysmography," IEEE journal of biomedical and health informatics **25**, 1397-1408 (2020).

42. M. Van Gastel, S. Stuijk, and G. de Haan, "Robust respiration detection from remote photoplethysmography," Biomedical optics express **7**, 4941-4957 (2016).

43. Z. Sun, Q. He, Y. Li, W. Wang, and R. K. Wang, "Robust non-contact peripheral oxygenation saturation measurement using smartphone-enabled imaging photoplethysmography," Biomedical Optics Express **12**, 1746-1760 (2021).

44. Z. Marcinkevics, U. Rubins, J. Zaharans, A. Miščuks, E. Urtane, and L. Ozolina-Moll, "Imaging photoplethysmography for clinical assessment of cutaneous microcirculation at two different depths," Journal of Biomedical Optics **21**, 035005 (2016).

45. (!!! INVALID CITATION !!! {}).

46. E. Zherebtsov, V. Dremin, A. Popov, A. Doronin, D. Kurakina, M. Kirillin, I. Meglinski, and A. Bykov, "Hyperspectral imaging of human skin aided by artificial neural networks," Biomedical optics express **10**, 3545-3559 (2019).

47. D. Kapsokalyvas, N. Bruscino, D. Alfieri, V. de Giorgi, G. Cannarozzo, R. Cicchi, D. Massi, N. Pimpinelli, and F. S. Pavone, "Spectral morphological analysis of skin lesions with a polarization multispectral dermoscope," Optics express **21**, 4826-4840 (2013).

48. S. Kim, D. Cho, J. Kim, M. Kim, S. Youn, J. E. Jang, M. Je, D. H. Lee, B. Lee, and D. L. Farkas, "Smartphone-based multispectral imaging: system development and potential for mobile skin diagnosis," Biomedical optics express **7**, 5294-5307 (2016).

49. C. Mo, G. Kim, K. Lee, M. S. Kim, B.-K. Cho, J. Lim, and S. Kang, "Non-destructive quality evaluation of pepper (Capsicum annuum L.) seeds using LED-induced hyperspectral reflectance imaging," Sensors **14**, 7489-7504 (2014).

50. G. Bert, B. Carolina, G. Pilar, T. Nicolaas, and L. Andy, "A tiny VIS-NIR snapshot multispectral camera," in *Proc.SPIE*, 2015), 937414.

51. P.-J. Lapray, J.-B. Thomas, and P. Gouton, "High Dynamic Range Spectral Imaging Pipeline For Multispectral Filter Array Cameras," Sensors **17**(2017).

52. S. Janis, O. Ilze, B. Anna, and B. Alexander, "Smartphone snapshot mapping of skin chromophores under triple-wavelength laser illumination," Journal of Biomedical Optics **22**, 091508 (2017).

53. L. Wang, P. C. Pedersen, D. M. Strong, B. Tulu, E. Agu, and R. Ignotz, "Smartphone-Based Wound Assessment System for Patients With Diabetes," IEEE Transactions on Biomedical Engineering **62**, 477-488 (2015).

54. H.-L. Shen, P.-Q. Cai, S.-J. Shao, and J. H. Xin, "Reflectance reconstruction for multispectral imaging by adaptive Wiener estimation," Optics Express **15**, 15545-15554 (2007).

55. H.-L. Shen and J. H. Xin, "Spectral characterization of a color scanner based on optimized adaptive estimation," J. Opt. Soc. Am. A **23**, 1566-1569 (2006).

56. C. Shuo and L. Quan, "Modified Wiener estimation of diffuse reflectance spectra from RGB values by the synthesis of new colors for tissue measurements," Journal of Biomedical Optics **17**, 030501 (2012).

57. I. Nishidate, T. Maeda, K. Niizeki, and Y. Aizu, "Estimation of Melanin and Hemoglobin Using Spectral Reflectance Images Reconstructed from a Digital RGB Image by the Wiener Estimation Method," Sensors **13**, 7902-7915 (2013).

58. D. K. Spierer, Z. Rosen, L. L. Litman, and K. Fujii, "Validation of photoplethysmography as a method to detect heart rate during rest and exercise," Journal of Medical Engineering & Technology **39**, 264-271 (2015).

59. H. G. M. K. John, N. Martin, M. V. Rudolf, and N. Herke Jan, "Non-contact tissue perfusion and oxygenation imaging using a LED based multispectral and a thermal imaging system, first results of clinical intervention studies," in *Proc.SPIE*, 2013), 857207.

60. K. Peters, B. Colebunders, S. Brondeel, S. D'Arpa, and S. Monstrey, "The foot fillet flap for ischial pressure sore reconstruction: A new indication," Journal of Plastic, Reconstructive & Aesthetic Surgery **71**, 1664-1678 (2018).

61. S. Liu, J. M. Hempe, R. J. McCarter, S. Li, and V. A. Fonseca, "Association between Inflammation and Biological Variation in Hemoglobin A1c in U.S. Nondiabetic Adults," The Journal of Clinical Endocrinology & Metabolism **100**, 2364-2371 (2015).

62. I. Stoffels, S. Morscher, I. Helfrich, U. Hillen, J. Leyh, N. C. Burton, T. C. P. Sardella, J. Claussen, T. D. Poeppel, H. S. Bachmann, A. Roesch, K. Griewank, D. Schadendorf, M. Gunzer, and J. Klode, "Metastatic status of sentinel lymph nodes in melanoma determined noninvasively with multispectral optoacoustic imaging," Science Translational Medicine **7**, 317ra199-317ra199 (2015).

63. F. Linming, H. Wei, L. Anqi, C. Yuanyu, X. Heng, P. Sushmita, L. Yiming, and L. Li, "Comparison of two skin imaging analysis instruments: The VISIA® from Canfield vs the ANTERA 3D®CS from Miravex," Skin Research and Technology **24**, 3-8 (2018).

64. R. Sender, S. Fuchs, and R. Milo, "Are We Really Vastly Outnumbered? Revisiting the Ratio of Bacterial to Host Cells in Humans," Cell **164**, 337-340 (2016).

65. E. A. Grice, H. H. Kong, S. Conlan, C. B. Deming, J. Davis, A. C. Young, n. null, G. G. Bouffard, R. W. Blakesley, P. R. Murray, E. D. Green, M. L. Turner, and J. A. Segre, "Topographical and Temporal Diversity of the Human Skin Microbiome," Science **324**, 1190-1192 (2009).

66. J. Kim, "Review of the Innate Immune Response in Acne vulgaris: Activation of Toll-Like Receptor 2 in Acne Triggers Inflammatory Cytokine Responses," Dermatology **211**, 193-198 (2005).

67. M. J. Verkaik, H. J. Busscher, D. Jager, A. M. Slomp, F. Abbas, and H. C. van der Mei, "Efficacy of natural antimicrobials in toothpaste formulations against oral biofilms in vitro," Journal of Dentistry **39**, 218-224 (2011).

68. B. Lange-Asschenfeldt, D. Marenbach, C. Lang, A. Patzelt, M. Ulrich, A. Maltusch, D. Terhorst, E. Stockfleth, W. Sterry, and J. Lademann, "Distribution of Bacteria in the Epidermal Layers and Hair Follicles of the Human Skin," Skin Pharmacology and Physiology **24**, 305-311 (2011).

69. I.-h. Jung, K. H. Yeon, H. R. Song, and Y. S. Hwang, "Cytotoxicity of dental disclosing solution on gingival epithelial cells in vitro," Clinical and Experimental Dental Research **6**, 669-676 (2020).

70. J. Chen, S. Feng, M. Chen, P. Li, Y. Yang, J. Zhang, X. Xu, Y. Li, and S. Chen, "In Vivo Dynamic Monitoring of Bacterial Infection by NIR-II Fluorescence Imaging," Small **16**, 2002054 (2020).

71. E. Barnard, T. Johnson, T. Ngo, U. Arora, G. Leuterio, A. McDowell, and H. Li, "Porphyrin Production and Regulation in Cutaneous Propionibacteria," mSphere **5**, e00793-00719 (2020).

72. S. V. Patwardhan, C. Richter, A. Vogt, U. Blume-Peytavi, D. Canfield, and J. Kottner, "Measuring acne using Coproporphyrin III, Protoporphyrin IX, and lesion-specific inflammation: an exploratory study," Archives of Dermatological Research **309**, 159-167 (2017).

73. I. Seo, S. H. Tseng, G. O. Cula, P. R. Bargo, and N. Kollias, "Fluorescence spectroscopy for endogenous porphyrins in human facial skin," in *Proc.SPIE*, 2009), 716103.

74. M. H. van der Veen, R. Z. Thomas, M. C. D. N. J. M. Huysmans, and J. J. de Soet, "Red Autofluorescence of Dental Plaque Bacteria," Caries Research **40**, 542-545 (2006).

75. N. Farhan and S. Jeffery, "Utility of MolecuLight i:X for Managing Bacterial Burden in Pediatric Burns," Journal of Burn Care & Research **41**, 328-338 (2020).

76. G. Guven, M. P. Hilty, and C. Ince, "Microcirculation: physiology, pathophysiology, and clinical application," Blood purification **49**, 143-150 (2020).

77. A. J. Bakermans, C. H. Wessel, K. H. Zheng, P. F. C. Groot, E. S. G. Stroes, and A. J. Nederveen, "Dynamic magnetic resonance measurements of calf muscle

oxygenation and energy metabolism in peripheral artery disease," Journal of Magnetic Resonance Imaging **51**, 98-107 (2020).

78. D. Lopez and C. M. Kramer, "Oxygenation and flow in the limbs: Novel methods to characterize peripheral artery disease," Current cardiovascular imaging reports **6**, 150-157 (2013).

79. M. J. Sullivan, J. D. Knight, M. B. Higginbotham, and F. R. Cobb, "Relation between central and peripheral hemodynamics during exercise in patients with chronic heart failure. Muscle blood flow is reduced with maintenance of arterial perfusion pressure," Circulation **80**, 769-781 (1989).

80. A. A. Frazier, T. J. Franks, T.-L. H. Mohammed, I. H. Ozbudak, and J. R. Galvin, "Pulmonary veno-occlusive disease and pulmonary capillary hemangiomatosis," Radiographics **27**, 867-882 (2007).

81. H. M. A. Hofstee, A. V. Noordegraaf, A. E. Voskuyl, B. A. C. Dijkmans, P. E. Postmus, Y. M. Smulders, and E. H. Serné, "Nailfold capillary density is associated with the presence and severity of pulmonary arterial hypertension in systemic sclerosis," Annals of the rheumatic diseases **68**, 191-195 (2009).

82. G. London, A. Covic, D. Goldsmith, A. Wiecek, G. Suleymanlar, A. Ortiz, Z. Massy, B. Lindholm, A. Martinez-Castelao, and D. Fliser, "Arterial aging and arterial disease: interplay between central hemodynamics, cardiac work, and organ flow—implications for CKD and cardiovascular disease," Kidney international supplements **1**, 10-12 (2011).

83. L. Østergaard, S. N. Jespersen, T. Engedahl, E. G. Jiménez, M. Ashkanian, M. B. Hansen, S. Eskildsen, and K. Mouridsen, "Capillary dysfunction: its detection and

causative role in dementias and stroke," Current neurology and neuroscience reports **15**, 37 (2015).

84. P. H. Tomlins and R. K. Wang, "Theory, developments and applications of optical coherence tomography," Journal of Physics D: Applied Physics **38**, 2519-2535 (2005).

85. S. Eriksson, J. Nilsson, and C. Sturesson, "Non-invasive imaging of microcirculation: a technology review," Med Devices (Auckl) **7**, 445-452 (2014).

86. J. Hansell, L. Henareh, S. Agewall, and M. Norman, "Non-invasive assessment of endothelial function–relation between vasodilatory responses in skin microcirculation and brachial artery," Clinical physiology and functional imaging **24**, 317-322 (2004).

87. G. E. Gökçek, D. Kartal, N. Kalay, S. L. Çinar, G. Savaş, and M. Borlu, "The relationship between the severity of coronary artery disease and skin measurement parameters," Skin Research and Technology: Official Journal of International Society for Bioengineering and the Skin (ISBS)[and] International Society for Digital Imaging of Skin (ISDIS)[and] International Society for Skin Imaging (ISSI) (2020).

88. M. Ohmi, M. Kuwabara, and M. Haruna, "Dynamic imaging of a small artery underneath skin surface of a human finger by optical coherence tomography," (2013).

89. Q. He, T. Liu, and R. K. Wang, "Enhanced spatial resolution for snapshot hyperspectral imaging of blood perfusion and melanin information within human tissue," Journal of Biophotonics **13**, e202000019 (2020).

90. V. Y. Toronov, X. Zhang, and A. G. Webb, "A spatial and temporal comparison of hemodynamic signals measured using optical and functional magnetic resonance imaging during activation in the human primary visual cortex," Neuroimage **34**, 1136-1148 (2007).

91. C.-L. Chen and R. K. Wang, "Optical coherence tomography based angiography," Biomed. Opt. Express **8**, 1056-1082 (2017).

92. S. L. Davis, P. J. Fadel, J. Cui, G. D. Thomas, and C. G. Crandall, "Skin blood flow influences near-infrared spectroscopy-derived measurements of tissue oxygenation during heat stress," Journal of applied physiology **100**, 221-224 (2006).

93. M. Paul, A. F. Mota, C. H. Antink, V. Blazek, and S. Leonhardt, "Modeling photoplethysmographic signals in camera-based perfusion measurements: optoelectronic skin phantom," Biomed. Opt. Express **10**, 4353-4368 (2019).

94. T. Tamura, Y. Maeda, M. Sekine, and M. Yoshida, "Wearable photoplethysmographic sensors—past and present," Electronics **3**, 282-302 (2014).

95. D. Castaneda, A. Esparza, M. Ghamari, C. Soltanpur, and H. Nazeran, "A review on wearable photoplethysmography sensors and their potential future applications in health care," International journal of biosensors & bioelectronics **4**, 195 (2018).

96. J. Liu, B. P.-Y. Yan, W.-X. Dai, X.-R. Ding, Y.-T. Zhang, and N. Zhao, "Multi-wavelength photoplethysmography method for skin arterial pulse extraction," Biomed. Opt. Express **7**, 4313-4326 (2016).

97. D. Biswas, N. Simões-Capela, C. Van Hoof, and N. Van Helleputte, "Heart rate estimation from wrist-worn photoplethysmography: A review," IEEE Sensors Journal **19**, 6560-6570 (2019).

98. N. Paradkar and S. R. Chowdhury, "Cardiac arrhythmia detection using photoplethysmography," in (IEEE, 113-116.

99. O. S. Hoilett, A. M. Twibell, R. Srivastava, and J. C. Linnes, "Kick LL: A smartwatch for monitoring respiration and heart rate using photoplethysmography," in (IEEE, 3821-3824.

100. V. V. Zaytsev, S. V. Miridonov, O. V. Mamontov, and A. A. Kamshilin, "Contactless monitoring of the blood-flow changes in upper limbs," Biomed. Opt. Express **9**, 5387-5399 (2018).

101. W. Wang, A. C. den Brinker, and G. De Haan, "Full video pulse extraction," Biomed. Opt. Express **9**, 3898-3914 (2018).

102. W. W. Muir and M. L. Wellman, "Hemoglobin solutions and tissue oxygenation," Journal of veterinary internal medicine **17**, 127-135 (2003).

103. D. A. Low, H. Jones, N. T. Cable, L. M. Alexander, and W. L. Kenney, "Historical reviews of the assessment of human cardiovascular function: interrogation and understanding of the control of skin blood flow," European journal of applied physiology **120**, 1-16 (2020).

104. M. Hellmann, M. Roustit, and J.-L. Cracowski, "Skin microvascular endothelial function as a biomarker in cardiovascular diseases?," Pharmacological Reports **67**, 803-810 (2015).

105. Q. He and R. Wang, "Hyperspectral imaging enabled by an unmodified smartphone for analyzing skin morphological features and monitoring hemodynamics," Biomedical Optics Express **11**, 895-910 (2020).

106. Q. He and R. K. Wang, "Analysis of skin morphological features and real-time monitoring using snapshot hyperspectral imaging," Biomed. Opt. Express **10**, 5625-5638 (2019).

107. Q. He, Z. Sun, Y. Li, W. Wang, and R. K. Wang, "Smartphone-enabled snapshot multispectral autofluorescence imaging and its application for bacteria assessments in skin and oral cavity," Optics and Lasers in Engineering **140**, 106546 (2021).

108. J. Eckhard, T. Eckhard, E. M. Valero, J. L. Nieves, and E. G. Contreras, "Outdoor scene reflectance measurements using a Bragg-grating-based hyperspectral imager," Applied Optics **54**, D15-D24 (2015).

109. J. Hernández-Andrés, J. Romero, and R. L. Lee, "Colorimetric and spectroradiometric characteristics of narrow-field-of-view clear skylight in Granada, Spain," JOSA A **18**, 412-420 (2001).

110. W. Karlen, J. Lim, J. M. Ansermino, G. Dumont, and C. Scheffer, "Design challenges for camera oximetry on a mobile phone," in *2012 Annual International Conference of the IEEE Engineering in Medicine and Biology Society*, 2012), 2448-2451.

111. W. B. Baker, A. B. Parthasarathy, D. R. Busch, R. C. Mesquita, J. H. Greenberg, and A. G. Yodh, "Modified Beer-Lambert law for blood flow," Biomed. Opt. Express **5**, 4053-4075 (2014).

112. R. D. Muir, S. Z. Sullivan, R. A. Oglesbee, and G. J. Simpson, "Synchronous digitization for high dynamic range lock-in amplification in beam-scanning microscopy," Review of Scientific Instruments **85**, 033703 (2014).

113. A. A. Kamshilin, S. Miridonov, V. Teplov, R. Saarenheimo, and E. Nippolainen, "Photoplethysmographic imaging of high spatial resolution," Biomed. Opt. Express **2**, 996-1006 (2011).

114. K. Jackman and C. Iadecola, "Neurovascular regulation in the ischemic brain," Antioxidants & redox signaling **22**, 149-160 (2015).

115. M. Gassmann, H. Mairbäurl, L. Livshits, S. Seide, M. Hackbusch, M. Malczyk, S. Kraut, N. N. Gassmann, N. Weissmann, and M. U. Muckenthaler, "The increase in hemoglobin concentration with altitude varies among human populations," Annals of the New York Academy of Sciences **1450**, 204-220 (2019).

116. P. Avci, A. Gupta, M. Sadasivam, D. Vecchio, Z. Pam, N. Pam, and M. Hamblin, "Low-Level Laser (Light) Therapy (LLLT) in skin: stimulating, healing, restoring," Seminars in cutaneous medicine and surgery **32**, 41-52 (2013).

117. P. Oltulu, B. Ince, N. Kokbudak, S. Findik, and F. Kilinc, "Measurement of epidermis, dermis, and total skin thicknesses from six different body regions with a new ethical histometric technique," Turkish Journal of Plastic Surgery **26**, 56-61 (2018).

118. L. Wang, S. L. Jacques, and L. Zheng, "MCML—Monte Carlo modeling of light transport in multi-layered tissues," Computer methods and programs in biomedicine **47**, 131-146 (1995).

119. R. K. Wang, "Signal degradation by multiple scattering in optical coherence tomography of dense tissue: a Monte Carlo study towards optical clearing of biotissues," Physics in Medicine & Biology **47**, 2281 (2002).

120. S. L. Jacques, "Optical properties of biological tissues: a review," Physics in Medicine & Biology **58**, R37 (2013).

121. L. An, J. Qin, and R. K. Wang, "Ultrahigh sensitive optical microangiography for in vivo imaging of microcirculations within human skin tissue beds," Opt. Express **18**, 8220-8228 (2010).

122. J. Lee, M. Kim, H.-K. Park, and I. Y. Kim, "Motion Artifact Reduction in Wearable Photoplethysmography Based on Multi-Channel Sensors with Multiple Wavelengths," Sensors **20**, 1493 (2020).

123. C.-C. Chang, C.-T. Wu, B. I. Choi, and T.-J. Fang, "MW-PPG sensor: An on-chip spectrometer approach," Sensors **19**, 3698 (2019).

124. F. P. Wieringa, F. Mastik, and A. F. W. van der Steen, "Contactless multiple wavelength photoplethysmographic imaging: A first step toward "SpO 2 camera" technology," Annals of biomedical engineering **33**, 1034-1041 (2005).

125. J. Zheng, S. Hu, V. Azorin-Peris, A. Echiadis, V. Chouliaras, and R. Summers, "Remote simultaneous dual wavelength imaging photoplethysmography: a further step towards 3-D mapping of skin blood microcirculation," in (International Society for Optics and Photonics, 68500S.

126. A. F. McDonagh, G. Agati, F. Fusi, and R. Pratesi, "QUANTUM YIELDS FOR LASER PHOTOCYCLIZATION OF BILIRUBIN IN THE PRESENCE OF HUMAN SERUM ALBUMIN. DEPENDENCE OF QUANTUM YIELD ON EXCITATION WAVELENGTH," Photochemistry and Photobiology **50**, 305-319 (1989).

127. G. Inamori, U. Kamoto, F. Nakamura, Y. Isoda, A. Uozumi, R. Matsuda, M. Shimamura, Y. Okubo, S. Ito, and H. Ota, "Neonatal wearable device for colorimetry-based real-time detection of jaundice with simultaneous sensing of vitals," Science Advances **7**, eabe3793 (2021).

128. J. A. Taylor, J. W. Stout, L. de Greef, M. Goel, S. Patel, E. K. Chung, A. Koduri, S. McMahon, J. Dickerson, E. A. Simpson, and E. C. Larson, "Use of a Smartphone App to Assess Neonatal Jaundice," Pediatrics **140**, e20170312 (2017).

129. Z. Hu, C. Fang, B. Li, Z. Zhang, C. Cao, M. Cai, S. Su, X. Sun, X. Shi, and C. Li, "First-in-human liver-tumour surgery guided by multispectral fluorescence imaging in the visible and near-infrared-I/II windows," Nature biomedical engineering **4**, 259-271 (2020).

130. L. Qiu, R. Chuttani, D. K. Pleskow, V. Turzhitsky, U. Khan, Y. N. Zakharov, L. Zhang, T. M. Berzin, E. U. Yee, and M. S. Sawhney, "Multispectral light scattering endoscopic imaging of esophageal precancer," Light: Science & Applications **7**, 17174-17174 (2018).

131. X. Hadoux, F. Hui, J. K. H. Lim, C. L. Masters, A. Pébay, S. Chevalier, J. Ha, S. Loi, C. J. Fowler, and C. Rowe, "Non-invasive in vivo hyperspectral imaging of the retina for potential biomarker use in Alzheimer's disease," Nature communications **10**, 1-12 (2019).

132. Y. Ji, Y. Kwak, S. M. Park, and Y. L. Kim, "Compressive recovery of smartphone RGB spectral sensitivity functions," Optics Express **29**, 11947-11961 (2021).

133. S. Cheemerla and M. Balakrishnan, "Global epidemiology of chronic liver disease," Clinical Liver Disease **17**, 365 (2021).

134. S. K. Asrani, H. Devarbhavi, J. Eaton, and P. S. Kamath, "Burden of liver diseases in the world," Journal of hepatology **70**, 151-171 (2019).

135. R. Lester, J. D. Ostrow, and R. Schmid, "Enterohepatic circulation of bilirubin," Nature **192**, 372-372 (1961).

136. A. Louvet and P. Mathurin, "Alcoholic liver disease: mechanisms of injury and targeted treatment," Nature reviews Gastroenterology & hepatology **12**, 231-242 (2015).

137. R. Williams, S. W. Schalm, and J. G. O'Grady, "Acute liver failure: redefining the syndromes," The Lancet **342**, 273-275 (1993).

138. S. Yasuda, S. Itoh, K. Isobe, M. Yonetani, H. Nakamura, M. Nakamura, Y. Yamauchi, and A. Yamanishi, "New transcutaneous jaundice device with two optical paths," (2003).

139. F. Hemmati and N. A. K. Rad, "The value of Bilicheck® as a screening tool for neonatal jaundice in the South of Iran," Iranian journal of medical sciences **38**, 122 (2013).

140. F. Outlaw, M. Nixon, O. Odeyemi, L.W. MacDonald, J. Meek and T.S. Leung, "Smartphone screening for neonatal jaundice via ambient-subtracted sclera chromaticity," PloS one **15**, 0216970 (2020).